Magnetization dynamics in magnetic nanostructures: spectroscopy, spin transfer effects and nonlinearities

Grégoire de Loubens

Université Paris-Sud

Mémoire présenté pour obtenir le

Diplôme d'Habilitation à Diriger des Recherches

Spécialité Physique de la Matière Condensée

par

Grégoire de Loubens

Service de Physique de l'État Condensé, CEA Saclay

Magnetization dynamics in magnetic nanostructures: spectroscopy, spin transfer effects and nonlinearities

Soutenance prévue le 14 décembre 2017
devant le jury composé de :

M. André Thiaville	Président
M. Christian Back	Rapporteur
M. Stéphane Mangin	–
Mme Catherine Gourdon	–
M. Nicolas Vukadinovic	Examinateur
Mme Ursula Ebels	–
M. Claude Fermon	–

Remerciements

J'aimerais d'abord remercier tous les membres de mon jury pour m'avoir fait l'honneur d'accepter d'en faire partie.

Ensuite j'aimerais remercier les collègues avec lesquels j'interagis au quotidien dans ma recherche depuis près de dix ans. Malgré son départ à Spintec, Olivier Klein reste mon collaborateur le plus proche : les résultats que je rassemble dans ce mémoire sont pour la plupart le fruit de notre complicité scientifique et de notre amitié. Michel Viret est l'autre pilier présent à mes côtés depuis mes débuts dans la recherche. J'espère partager avec lui bureau et idées en tout genre pour de nombreuses années encore. Je remercie aussi mon chef de groupe, Claude Fermon, pour son écoute attentive, ses conseils avisés, et son soutien bienveillant.

Je souhaite également remercier tous mes autres collègues, chercheurs et techniciens, du Laboratoire Nanomagnétisme et Oxydes, et en particulier Jean-Baptiste Moussy, Jean-Yves Chauleau, Myriam Pannetier-Lecœur, Aurélie Solignac et Gérald Le Goff et Grégory Cannies.

Je tiens tout particulièrement à remercier Vladimir Naletov pour tout ce qu'il apporte par sa présence au laboratoire lors de ses séjours au SPEC.

Je remercie aussi tous les étudiants en thèse et post-doctorants que j'ai été amené à encadrer, et dont la contribution à ce travail est primordiale : Benjamin Pigeau, Christian Hahn, Abbass Hamadeh, Xavier de Milly, et Nathan Beaulieu et Yi Li.

Je tiens également à remercier tous mes collaborateurs. Parmi ceux-ci, il y a bien sûr les collaborateurs historiques, Jamal Ben Youssef, Nicolas Vukadinovic, Hervé Hurdequint, Vincent Cros, Julie Grollier, Andrei Slavin et Vasyl Tiberkevich, que je connais tous depuis ma thèse, et avec qui je travaille toujours avec grand plaisir aujourd'hui.

Merci également à Madjid Anane et Paolo Bortolotti, Sergej Demokritov et Vladislav Demidov, Konstantin Guslienko, José María de Teresa et Soraya Sangiao, avec qui j'espère travailler longtemps encore.

Même si je ne présente pas mon travail de post-doctorat dans ce mémoire, j'aimerais aussi remercier mon ancien boss à NYU, Andy Kent, et Dimitri Garanin, avec qui ce fut un plaisir de collaborer pendant deux années.

Enfin, un grand merci à mon épouse Sophie pour son soutien depuis dix ans et ses encouragements pour la rédaction de ce mémoire.

Contents

Chapter 1

Introduction

In this introduction, I start with summarizing my main research interests. This first section is also a brief introduction to the field of magnetization dynamics. Then, I describe magnetic resonance force microscopy, the main experimental approach that I have used to probe so far magnetization dynamics at the sub-micron scale. I then mention the pedagogical responsibilities which I have got up to now in my career, and give the outline of the rest of this manuscript.

1.1 Research interests

My research interests lie in the fields of microwave nanomagnetism and spintronics. In particular, I study the interplay between the magnetization dynamics [64] and the transport of angular momentum in heterostructures [183]. This allows to control the relaxation of small magnetic objects, and even to destabilize their magnetization, which then becomes free to auto-oscillate. The obtained magnetization oscillations, typically in the GHz range and of large amplitude, are tunable and can be converted into voltage oscillations through magnetoresistive effects. These spin transfer nano-oscillators are thus quite promising for microwave applications. I aim at characterizing and improving their high frequency properties, which requires a detailed knowledge of their excitation spectra and nonlinear properties [163]. In particular, I am investigating the opportunities offered by the vortex state, a topological configuration that magnetization can adopt in nanostructures [67], and by the mutual synchronization of several oscillators [147].

I am also interested in the transmission of pure spin currents at the interface between a ferromagnetic insulator and a normal metal. This possibility recently opened the field of spintronics to insulating magnetic oxides such as Yttrium iron garnet [94], a ferrimagnetic material with unsurpassed dynamical quality. Taking advantage of the spin Hall effect to produce a pure spin current transverse to the charge current flowing into a heavy metal layer [51, 88], it is possible to generate an interfacial spin-orbit torque on an adjacent ultra-thin YIG layer, thereby controlling electrically its magnetic relaxation. This is very promising for magnonics, an emerging research field whose aim is to exploit spin-waves and their quanta magnons to carry and process information [107], since this offers a natural connection to spintronics [29], itself well interfaced with standard electronics. The possibility of integrating ferromagnetic materials directly in micro-electronic circuits is attracting because firstly, the typical time (ps to ns) and length scales (nm to μm)

of spin-waves nicely match those of modern micro-electronics and secondly, it allows to make non-volatile reconfigurable microwave devices.

My general approach on this research line is much more fundamental than applicative. In fact, the new class of microwave devices that the marriage between nanomagnetism and spintronics promises is still at its infant stage, mostly because there are still many fundamental challenges to be understood. Moreover, these two fields evolve quite rapidly, as illustrated for instance by the recent blossoming of spin orbitronics and skyrmion-based proposals [53]. Because microwave oscillations of the magnetization around its equilibrium are the natural dynamical response to external perturbations, a spectroscopic approach is necessary to understand the spatio-temporal evolution of magnetization dynamics in nanostructures, whatever the latter being driven by a microwave field, spin transfer torque, or thermally. This is what we started to develop with Olivier Klein during my thesis, and pushed further later on. Before describing it in some more details, let me first introduce the equation of motion of magnetization.

Equation of motion of magnetization

In the microwave regime, the dynamics of the magnetization in a ferromagnet is well described by the Landau-Lifshitz-Gilbert (LLG) equation [64]

$$\frac{d\boldsymbol{M}(\boldsymbol{r},t)}{dt} = -|\gamma|\mu_0 \boldsymbol{M}(\boldsymbol{r},t) \times \boldsymbol{H_{eff}}(\boldsymbol{r},t) + \alpha \frac{\boldsymbol{M}(\boldsymbol{r},t)}{M_s} \times \frac{d\boldsymbol{M}(\boldsymbol{r},t)}{dt}, \tag{1.1}$$

where $\boldsymbol{M}$ is the magnetization field, γ the gyromagnetic ratio, μ_0 the permeability of free space and α the Gilbert damping parameter. The effective magnetic field $\boldsymbol{H_{eff}} = -\frac{1}{\mu_0}\frac{\partial F}{\partial \boldsymbol{M}}$ derives from the magnetic free energy density F accounting for all the magnetic interactions in the material. This equation of motion, valid at the *local* microscopic scale (the exchange length), conserves the norm of the magnetization vector, $|\boldsymbol{M}(\boldsymbol{r},t)| = M_s$. Moreover, it is obviously *nonlinear*, because the effective field depends on magnetization. The *phenomenological* relaxation term is here in its well-known form of viscous Gilbert damping (a nonlinear model of magnetic dissipation has also been proposed, where the constant Gilbert damping parameter is generalized to a function of the dimensionless scalar proportional to $(d\boldsymbol{M}/dt)^2$ [180]).

Spin-wave modes

A general theory of linear spin-wave excitations [134] can be developed based on Eq.(1.1), and this for any *arbitrary* equilibrium magnetic configuration, including nontrivial textures such as, *e.g.*, a magnetic vortex [74]. The linearization of the local equation of motion is obtained by decomposing the instantaneous magnetization vector $\boldsymbol{M}(\boldsymbol{r},t)$ into a static and dynamic component, $\boldsymbol{M}(\boldsymbol{r},t)/M_s = \hat{\boldsymbol{u}}(\boldsymbol{r}) + \boldsymbol{m}(\boldsymbol{r},t) + \mathcal{O}(\boldsymbol{m}^2)$, where the transverse component $\boldsymbol{m}(\boldsymbol{r},t)$ is the small dimensionless deviation ($|\boldsymbol{m}| \ll 1$) of the magnetization from the equilibrium direction $\hat{\boldsymbol{u}}(\boldsymbol{r})$, and orthogonal to it, due to the conservation of the norm. Substituting this ansatz in the lossless LLG equation, one obtains that the spin-wave frequencies can be estimated from a variationally stable relation with respect to the mode profile $\boldsymbol{m}_\nu$:

$$\omega_\nu = \frac{\langle \overline{\boldsymbol{m}_\nu} \cdot \widehat{\boldsymbol{\Omega}} * \boldsymbol{m}_\nu \rangle}{\mathcal{N}_\nu}, \tag{1.2}$$

where the brackets stand for the spatial average over the volume of the magnetic body, $\mathcal{N}_\nu$ is a normalization constant, and $\widehat{\boldsymbol{\Omega}}$ is a self-adjoint tensor operator, containing all the contributions of the effective field [134], including the exchange and magneto-dipolar interactions, which makes it an integro-differential operator. Injecting some trial vectors inside Eq.(1.2) allows one to get approximate values of ω_ν with high accuracy [7], providing they should form a complete basis in the space of vector functions $\boldsymbol{m}$, be locally orthogonal to $\hat{\boldsymbol{u}}$ and satisfy appropriate boundary conditions at the edges of the magnetic body [69].

Spin transfer torque

Owing to the possibility for spin polarized carriers to transfer angular momentum to local magnetic moments, a spin polarized current can exert a torque on the magnetization $\boldsymbol{M}$ of a ferromagnetic layer. This spin transfer torque, predicted by Slonczewski [165] and Berger [12], writes:

$$\boldsymbol{T}_{\mathrm{STT}} = |\gamma| \frac{J_s}{M_s t_{\mathrm{FM}}} \boldsymbol{M}(\boldsymbol{r},t) \times \left(\hat{\boldsymbol{e}}_{\boldsymbol{\sigma}} \times \frac{\boldsymbol{M}(\boldsymbol{r},t)}{M_s} \right). \tag{1.3}$$

In this expression, t_{FM} is the thickness of the ferrromagnetic layer on which the torque $\boldsymbol{T}_{\mathrm{STT}}$ is acting, J_s the spin current density flowing through it (in units of $\hbar/\mathrm{m}^2/\mathrm{s}$) and $\hat{\boldsymbol{e}}_{\boldsymbol{\sigma}}$ the unit vector along the direction of the spin polarization. In the presence of a spin current J_s, this spin torque should thus be added to the right hand side of the equation of motion of magnetization Eq.(1.1). When the spin polarization is collinear to the equilibrium magnetization, $\boldsymbol{T}_{\mathrm{STT}}$ is either parallel or anti-parallel to the natural damping torque $\alpha \frac{\boldsymbol{M}}{M_s} \times \frac{d\boldsymbol{M}}{dt}$, depending on the sign of the current. Hence, there exists a critical spin current for which the latter can be fully compensated:

$$J_s^* = -\frac{1}{|\gamma|} \left(\frac{\partial \omega}{\partial H_0} \right) \frac{\alpha \omega M_s t_{\mathrm{FM}}}{|\gamma|}. \tag{1.4}$$

Above this *instability threshold* [15, 163], the external flow of angular momentum carried by J_s balances the loss of angular momentum of the magnetization precessing at ω in the field H_0, which is thus free to auto-oscillate on a limit cycle. The spin current density required to destabilize the magnetization is therefore directly proportional to the Gilbert damping rate $\alpha\omega$. It is also proportional to t_{FM}, which reflects the interfacial nature of the spin torque process.

Nonlinearities

As mentioned above, the LLG equation is nonlinear, which results in a variety of interesting phenomena. In certain high symmetry cases, exact analytical results for the nonlinear large motion of the magnetization vector can be derived [14]. The fact that the precession frequency depends on the precession amplitude through the variation of $\boldsymbol{H_{eff}}$ results in the so-called *foldover* of the resonance line, which is a very general consequence of nonlinear effects. The threshold associated to the appearance of bistable dynamics in high power ferromagnetic resonance (FMR) was predicted as early as 1955 [3]. This very same source of nonlinearity is at the heart of the high tunability of spin torque oscillators [163].

But the nonlinearities of the LLG equation have much further implications, as they do couple the different spin-wave modes together. In particular, this leads to the so-called

Suhl instabilities [170], which prevent to achieve large angle of uniform precession in extended films. The nonlinear coupling between the uniform mode and the spin-wave modes allows some energy to be channeled from the former, which is pumped out-of-equilibrium, to the latter. A threshold is reached when the natural losses of the spin-waves are not sufficient anymore to make their population relax towards thermal equilibrium, which suddenly increases their occupation number, and severely limits the uniform precession amplitude in a feedback mechanism [37]. A similar mechanism is at play in parallel pumping, where the nonlinear coupling originates from the ellipticity of uniform precession [166]. A semi-classical treatment of spin-waves allows one to calculate these instability thresholds [64, 166, 170].

Nonlinear effects in magnetization dynamics also enable the formation of dissipative solitons [106], and give rise to many other unique phenomena, as for instance dynamic reversal of the vortex core [73]. As for other physical systems, they can also lead to turbulent regimes and chaos [198]. Finally, they are also key to the formation of Bose-Einstein condensates of magnons [45].

Experimental studies

Studying magnetization dynamics under the aspects of spin-wave excitations, spin transfer effects, and nonlinearities is particularly interesting in nanostructures. For instance, non-uniform magnetic configurations can be stabilized in nanostructures, with specific properties concerning these three aspects. Moreover, spin-wave modes are quantized due to the geometric confinement, which also limits the nonlinear energy flow between spin-waves. In the study of spin transfer effects, nanostructuration is required to reach the threshold current density of about 10^{11} A/m^2 to balance the natural damping. Although the spin transfer torque does not select any particular spin-wave mode, usually only the lowest energy auto-oscillates and reaches large amplitudes above the threshold current due to nonlinear mode competition in the nanostructure [163].

These considerations show that there are some deep relationships between the spectral properties of magnetic nanostructures, their nonlinear characteristics, and the way their dynamics can be excited by external stimuli, including spin transfer effects. One of my main goal is to perform experiments to shed light on and to understand them. For this, a thorough examination of model samples with simple structure and high symmetry is usually key. In these studies, I mainly rely on well-known high frequency transport techniques, which I shall therefore not discuss here, as well as on an original approach to detect magnetization dynamics at the nanoscale, which I shortly introduce in the following section.

Related publications

1. G. de Loubens and M. Bailleul. *Microwave nanomagnetism: spin torque oscillators and magnonics*, in *Nanomagnetism: Applications and Perspectives*, C. Fermon, M. Van de Voorde Eds. (Wiley, 2017)

Grégoire de Loubens

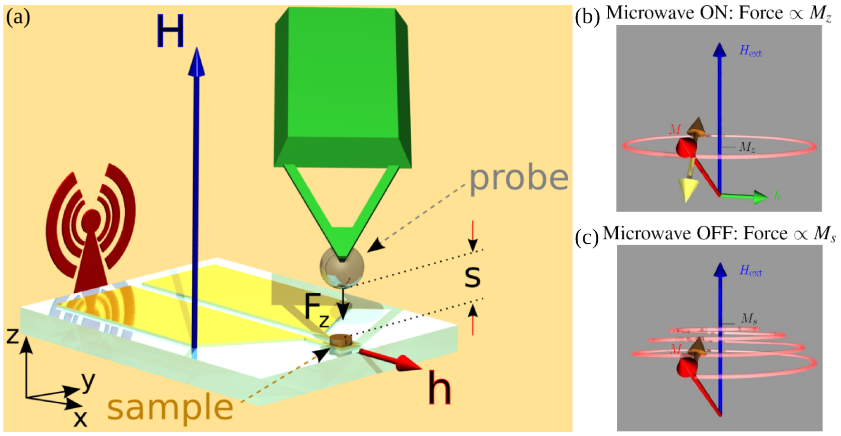

Figure 1.1: ***Principles of MRFM.*** *(a) Schematics of an MRFM setup. The MRFM probe is dipolarly coupled to the magnetization of the sample, which induces a force F_z on the cantilever. (b) When the microwave field h is turned on, the force on the cantilever is proportional to the longitudinal component of the magnetization M_z. (c) When the microwave is switched off, M_z relaxes back to M_s, its equilibrium value.*

1.2 Magnetic resonance force microscopy

Magnetic resonance force microscopy (MRFM) is a near field technique which combines magnetic force microscopy (MFM) with magnetic resonance imaging (MRI) [162]. It was first proposed by John Sidles some 25 years ago [161] as a powerful method to detect nuclear and electron spin resonances of small spin ensembles at the nanometer scale. The rational behind is that traditional inductive methods are sensitive to the time derivative of the magnetic flux, which severely decreases with the sample size, on the contrary to the force detection scheme of MRFM. This technique was experimentally pushed to its best by Dan Rugar's group, who reported on single spin detection with it [153] and on MRI of a biological sample with 4 nm spatial resolution and a noise level below 30 protons [40]. Quite early it was also recognized by Chris Hammel and Phil Wigen as an interesting technique to probe ferromagnetic resonance in microscopic samples [203]. A first MRFM setup to study ferromagnetic samples was built in my lab in CEA/SPEC by Olivier Klein and Vladimir Naletov in the early 2000s, who both educated and trained me on this technique during my PhD.

Principles

A schematics of an MRFM setup is presented in Fig.1.1a. It relies on the dipolar interaction between a magnetic particle attached at the end of a very soft cantilever, which acts as a force sensor, and the magnetization of the sample under study. When the latter undergoes precession, its longitudinal component of magnetization, M_z, is reduced from its equilibrium value M_s (Figs.1.1b and c), which changes the force F_z on the cantilever, thereby inducing a displacement which can be detected optically. In order to gain sensitivity, MRFM experiments are operated in vacuum, which increases the quality factor of the cantilever, and the signal is modulated at the mechanical frequency of the cantilever. The frequency of magnetization precession, in the GHz range, is much larger than the cantilever frequency, which lies in the kHz range. Moreover, magnetic relaxation (Fig.1.1c) typically occurs in a few ns to several hundreds of ns, *i.e.*, on a much shorter time scale

than the mechanical oscillation period of the cantilever, which is typically 100 μs. Therefore, with this amplitude modulation, the MRFM signal is directly proportional to the *static* change of longitudinal component of the magnetization induced by the precession, $\Delta M_z = M_s - M_z$, which is directly proportional to the total number of magnons excited in the sample, $n_t = \Delta M_z/(\gamma\hbar)$ [37].

Sensitivity

The MRFM sensitivity is limited by the thermal noise of the cantilever,

$$F_{\min} = \sqrt{B\frac{4k_BTk}{2\pi f_cQ}} \tag{1.5}$$

where B is the bandwidth of the measurement, k_B the Boltzmann constant, T the temperature, k the spring constant of the cantilever, f_c its mechanical frequency, and Q its quality factor. With the typical parameters of the mechanical oscillator (we use commercial Olympus Biolevers), $k = 6\ 10^{-3}$ N/m, $Q = 2000$ under vacuum, $f_c = 10$ kHz, the force sensitivity is below 1 fN/$\sqrt{\text{Hz}}$ at room temperature. This translates into a spin sensitivity, which depends on the coupling geometry between the sample and the MRFM probe, that sets the dipolar force between them. Typically, in our experiments, the MRFM probe is a sub-micronic sphere of large magnetization material such as Fe or Co, separated by about 1 to 2 μm from a sub-micronic disk ferromagnetic sample (in other words, the sketch of Fig.1.1a is rouhgly at scale concerning the sample and probe), which results in a spin sensitivity between 100 and 1000 Bohr magnetons in a 1 Hz bandwidth at room temperature.

Spatial resolution and spectral distortions

The concept of "resonant slice" [162], which sets the spatial resolution of MRFM on paramagnetic spin systems ($\propto \Delta H_{\text{sample}}/\nabla H_{\text{probe}}$, the ratio of the resonance linewidth to the field gradient produced by the magnetic tip), does not apply to ferromagnetic systems, in which spins are coupled through exchange, and precess collectively. In this case, one can still get spatial information on the precession profile in the sample with resolution down to 100 nm [63], which is primarily determined by the separation between the sample and the tip, as in standard MFM. One complication is that the inhomogeneous strayfield of the MRFM probe sets a trade-off between spatial resolution and spectral distortions. But it is also possible to take advantage of the latter, namely, to use the magnetic tip strayfield to localize the spin-wave modes in the ferromagnetic material right beneath the probe, which provides a novel type of nanoscale imaging [114].

Spectroscopic approach

We chose an opposite approach, as in our experiments, we are rather interested in obtaining an intrinsic spectroscopic information on the ferromagnetic nanostructure under study. As mentioned above, our coupling geometry uses a comparatively rather large MRFM probe to detect the magnetization dynamics in a rather small sample situated quite far away from it (Fig.1.1a). This minimizes the spectral distortions, as the probe strayfield is very homogeneous on the sample (typical average value in the 50 – 500 G

range), while maintaining excellent sensitivity, at the cost of essentially loosing spatial resolution. It is quite clear that in this weak coupling geometry, the MRFM signal will be almost independent of the lateral position of the probe above the sample and of the precession profile in the latter. Even in this case, it is possible to take advantage of the inhomogeneous probe strayfield to perform a spectroscopy of the dipolar coupling between adjacent nanomagnets, as will be shown in section 3.3.1, or to probe the nonlinearity of the confinement potential of a vortex core in a nanodot (section 2.3.1).

In the experimental studies presented in this manuscript, we thus use MRFM on individual nanostructures in a mode where sensitive spectroscopy is favored with respect to spatial resolution. One main other advantage of this mode is that the sample can be buried below rather thick electrodes, as the MRFM detection scheme relies on the long range dipolar coupling between sample and probe (no optical access required). This is particularly interesting to study spin torque nano-oscillators (chapter 3) which need contact electrodes to supply the dc current. Moreover, this allows to incorporate the microwave antenna directly above the sample (rather than beneath it, as sketched in Fig.1.1a), which is convenient to study nanostructures made of epitaxial materials, such as NiMnSb (chapter 2), FeV (chapters 2 and 3), and YIG (chapter 4).

In the following of this manuscript, I will not give any more experimental details on the MRFM technique, except in the particular cases, where the inhomogeneous strayfield of the probe is used advantageously. Moreover, some perspectives on the development of new MRFM probes will be presented in section 5.1.2.

Related publications

1. O. Klein, G. de Loubens, V. V. Naletov, F. Boust, T. Guillet, H. Hurdequint, A. Leksikov, A. N. Slavin, V. S. Tiberkevich, N. Vukadinovic, *Ferromagnetic resonance force spectroscopy of individual submicron-size samples*, Phys. Rev. B **78**, 144410 (2008).

1.3 Pedagogical responsibilities

Since my post-doctoral years, I have contributed to the education of many students. In 2007, I have supervised with Andy Kent at NYU the master thesis of Simon Herr on micro-Hall effect magnetometry of Mn_{12}-based single molecule magnets. In 2009 and 2011, I have supervised with Olivier Klein in CEA/SPEC two master students who eventually did their PhD thesis with us, Benjamin Pigeau and Abbass Hamadeh. In 2014, I have supervised the master thesis of Hugo Meley on spin transfer effects in YIG/Pt hybrid structures.

In total, I have co-supervised three PhD theses with Olivier Klein, and I am currently supervising one student, who is about to defend his thesis:

1. The thesis of Benjamin Pigeau (now a permanent CNRS researcher in Institut Néel, Grenoble) on magnetic vortex dynamics in nanostructures from 2009 to 2012.

2. The thesis of Abbass Hamadeh (now an assistant professor at the Lebanese University in Beyrouth) on synchronization of spin transfer nano-oscillators from 2011 to 2014.

3. The thesis of Christian Hahn (now a permanent staff researcher at PTB, Brunswick) on magnetization dynamics and pure spin currents in YIG / normal metal systems from 2011 to 2014.

4. Since 2014, I am the PhD advisor of Xavier de Milly, on the manipulation of mutual synchronization in a pair of spin torque oscillators.

I have also been the scientific advisor of two young post-doctoral researchers, Dr. Nathan Beaulieu (during one year in 2015-2016, on the FMR and MRFM characterization of YIG and YIG/Pt thin films and nanostructures) and Dr. Yi Li (during two years in 2015-2017, on two different projects: dipolar coupling in spin transfer vortex oscillators and nonlinear dynamics in YIG nanostructures). In the last years, I have also supervised several undergraduate students on small projects focused on the MRFM technique (Hugo Lavenant in 2013, Darius Mofakhami in 2015 and Didier St Médar in 2016).

Besides supervising students and postdocs in the lab, I have also been involved a little bit in teaching. During the three years of my PhD thesis, I have been a teaching assistant in quantum mechanics and statistical physics classes at École Centrale Paris, where I shared responsibility for lectures, exams, homework assignments and grades. Moreover, while my permanent position in CEA is as a full researcher, I really enjoy to be involved occasionally in undergraduate or graduate courses. For instance, I propose bibliographic projects to small groups of students in Éric Vincent's magnetism course at Centrale/Supelec.

1.4 Organization of the manuscript

In the three next chapters, I am presenting an overview of my research activities on magnetic vortex dynamics, spin torque nano-oscillators, and magnetization dynamics in magnetic insulators / normal metal hybrids, respectively. Even though this is a quite natural way to separate my research of the past nine years into three main topics, I also emphasize the links which exist between them. Then, current research projects and future perspectives which I would like to develop are presented in the final chapter of this manuscript.

Each chapter is split into two or three sections, which compile a few published results, sometimes very briefly presented, some other times completed with some unpublished data. For further reading, a list of my related publications is provided at the end of each main section, with the involved students underlined. Moreover, a general summary of the main research results is provided in French at the end of each chapter.

Résumé en français

Mes travaux de recherche portent sur la dynamique de l'aimantation dans les nanostructures magnétiques et l'électronique de spin. Actuellement, je m'intéresse à l'interaction entre la dynamique de l'aimantation et le transport de moment angulaire dans des hétérostructures. Elle permet de contrôler la relaxation de petits objets magnétiques, voire de déstabiliser leur aimantation, alors libre d'auto-osciller. Les oscillations de l'aimantation ainsi obtenues, typiquement dans la gamme GHz et de grande amplitude, peuvent être converties en oscillations de tension par des effets magnétorésistifs. Ces nano-oscillateurs à transfert de spin sont donc prometteurs pour les applications micro-ondes. Je cherche à caractériser et améliorer leurs propriétés hyperfréquences, ce qui nécessite une compréhension détaillée de leurs spectres d'excitations et de leurs propriétés non-linéaires. Les possibilités offertes par l'état vortex et la synchronisation de plusieurs oscillateurs sont notamment étudiées. Je m'intéresse également à la transmission de courants purs de spin à l'interface entre un matériau ferromagnétique isolant et un métal normal. Cette découverte récente permet d'incorporer des matériaux tels que le YIG (un grenat d'Yttrium Fer aux propriétés hyperfréquences inégalées) dans des dispositifs innovants de la spintronique. Le contrôle électronique de la relaxation de couches ultra-minces de YIG nanostructurées grâce au courant de spin généré par effet Hall de spin à l'interface avec un métal à fort couplage spin-orbite (par ex., Pt) ouvre en effet de nombreuses perspectives, dont celle d'utiliser des ondes de spin (ou leurs quanta = magnons) pour transmettre et traiter l'information, idée à la base de la magnonique.

Dans ces études, je m'appuie entre autres sur une technique originale de détection de la dynamique de spin à l'échelle nanométrique développée au laboratoire, la microscopie de force par résonance magnétique (MRFM). Cette technique de champ proche combine microscopie à force atomique et imagerie par résonance magnétique. Elle utilise une sonde magnétique placée à l'extrémité d'un levier mécanique très souple pour détecter la dynamique de l'aimantation (Fig.1.1).

Chapter 2

Magnetic vortex dynamics

The magnetic vortex is a topological singularity which can be stabilized in thin ferromagnetic platelets due to the competition between demagnetizing and exchange energies. This micromagnetic state can be viewed as an in-plane curling magnetization with a central region, the vortex core, where the magnetization points out-of-plane. It corresponds to the ground state for submicrometer- and micrometer-sized soft ferromagnetic disks [127, 33] with a thickness and a disk radius respectively larger and much larger than the exchange length (typically around 5 nm) [67]. The vortex state is characterized by two topological quantities: the vortex core polarization (direction of the vortex core magnetization) [160] and the vortex chirality (rotational direction of the in-plane magnetization).

Before we started to investigate the high frequency dynamics of this topological state in nanodots, it was already well established both theoretically and experimentally that its zero field spin-wave excitation spectrum consisted of a low-frequency (sub-GHz range) vortex translation mode corresponding to the gyrotropic motion of the vortex core as a whole around the disk center [65, 91, 143, 138, 71] and a set of radial and azimuthal modes spreading mainly outside the vortex core and occurring beyond a few GHz [204, 202, 139, 18, 58, 135, 191]. A coupling between the vortex translation mode and the azimuthal modes leading to a frequency splitting of the azimuthal modes had also been evidenced [142, 89, 74, 6]. Moreover, it was demonstrated and explained that the vortex core could be dynamically reversed by exciting the gyrotropic mode in the strongly nonlinear regime [192, 200, 73].

The main originality of our studies on vortex dynamics in magnetic dots lies in the fact that a bias field normal to the sample plane, *i.e.*, preserving the axial symmetry of the system, is applied. This induces a deformation of the vortex texture into the so-called "cone state", and correspondingly, of its topology, which modifies its linear excitation spectrum. These effects were analytically calculated [91] and simulated [17], but never observed experimentally. Moreover, it is also interesting to spectroscopically investigate the nonlinearities of the gyrotropic mode, and how the dynamical reversal of the vortex core is affected by the presence of the perpendicular bias field.

In these studies, we use MRFM to detect the magnetization dynamics in individual soft magnetic dots made of epitaxial NiMnSb or FeV layers with high dynamical quality (Gilbert damping parameter $\alpha \approx 2 - 3\ 10^{-3}$) [1]. In particular, we show that the applied perpendicular field lifts the frequency degeneracy of the gyrotropic modes associated to

[1] Respectively provided by the teams of Laurens Molenkamp (Universität Würzburg) and Stéphane Andrieu and François Montaigne (Université de Lorraine).

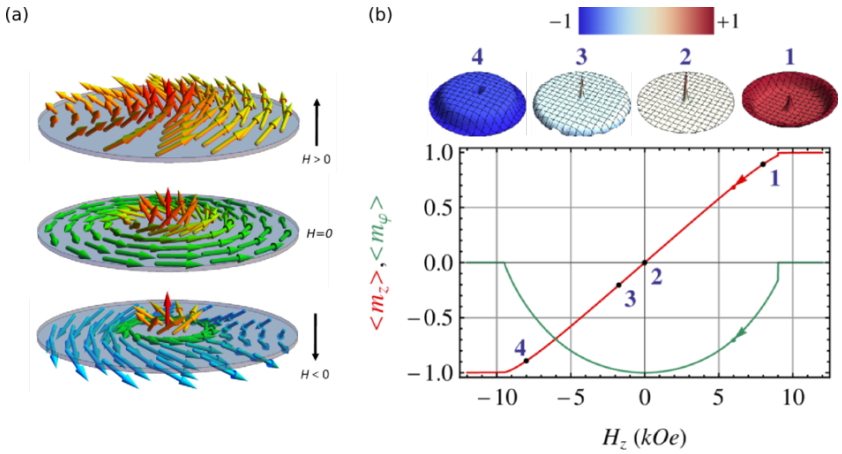

Figure 2.1: ***Equilibrium configuration in the cone state.*** *(a) Magnetic configuration in the vortex state under positive, vanishing and negative perpendicular field, from top to bottom. (b) Computed evolutions of the longitudinal (m_z, red curve) and orthoradial (m_φ, green curve) components of the magnetization of a 50 nm thick, 1 µm diameter Permalloy dot as a function of the decreasing bias perpendicular field H_z. The 3D images on top correspond to the static magnetization configurations for four decreasing values of the magnetic field.*

opposite core polarities $p = \pm 1$, which allows a simple spectroscopic determination of the core orientation with respect to the bias field (section 2.1) [39], and enables deterministic dynamical reversal of the vortex core (section 2.2) [144]. Moreover, taking advantage of the strayfield of the MRFM probe, we determine the anharmonicity of the magnetostatic confinement potential of the vortex core in a nanodot (section 2.3) [172].

Another important aspect of the work presented in this chapter is that it has strong connections with the research activities on vortex-based spin torque oscillators (section 3.2), where applying a perpendicular field and determining nonlinearities are crucial [49].

2.1 Spectroscopy of the cone state

The effect of a bias perpendicular field H_z on the static magnetic configuration of a vortex sate dot is sketched in Fig.2.1a. It mainly tilts the spins in the peripheral region. Fig.2.1b presents the dependence on the decreasing H_z of the longitudinal ($< m_z >$) and orthoradial ($< m_\varphi >$) space-averaged normalized magnetization components of a micron size Permalloy disk determined by 3D micromagnetic simulations [20]. For large magnetic field values ($|H_z| > H_s \simeq 9$ kOe), the disk is uniformly magnetized along z. The deformed vortex state exists in a large range of perpendicular field where $< m_z >$ varies linearly with H_z. The orthoradial component is non-zero only if $|H_z| < H_s$, and passes through an extremum at zero field ($< m_\varphi = -1 >$ corresponds to a clockwise rotation). In addition, $< m_\varphi >$ exhibits a jump at $H_z = H_s$ (first-order phase transition) whereas it is continuous at $H_z = -H_s$ (second-order phase transition) for a downward field sweep. This behavior is inverted for an upward field sweep giving rise to a weak hysteresis.

From the 3D images in Fig.2.1b, it is also clear that the negative perpendicular field switches the vortex core somewhere in between labels by 3 and 4. This process has been studied in details both analytically and numerically in ref. [176] and is attributed to the formation of a Bloch point when the vortex core is squeezed by the applied anti-parallel

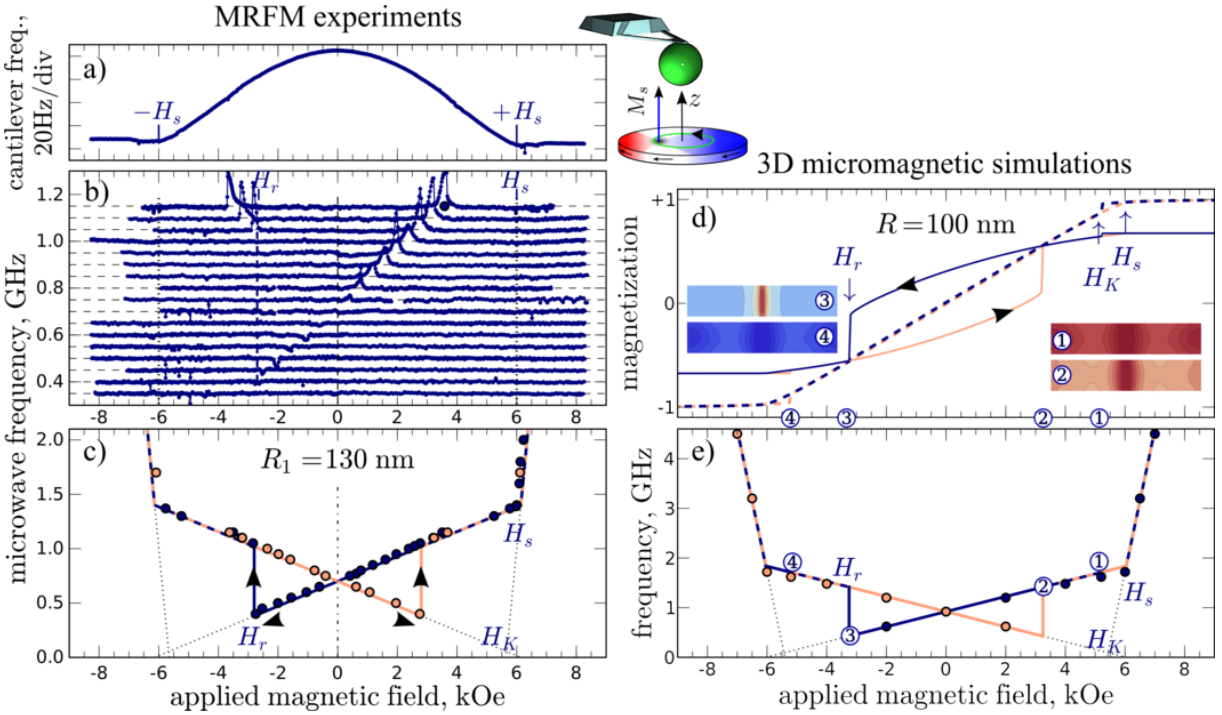

Figure 2.2: ***Spectroscopy of the gyrotropic mode.*** *(a) MRFM cantilever frequency shift, proportional to the perpendicular magnetization component of the $t = 44$ nm, $R = 130$ nm NiMnSb disk sample, as a function of the perpendicular field H_z. H_s is the saturation field of the sample. The inset shows the MRFM detection scheme. (b) MRFM spectra of the gyrotropic mode under microwave irradiation in the cone state ($-H_s < H_z < H_s$). (c) Hysteretic behavior of the gyrotropic frequency as a function of H_z, which displays a jump at the vortex core reversal field H_r. (d) 3D micromagnetic simulation of the static magnetization M_z averaged over the disk volume (dashed loop) and over the vortex core (solid loop). The insets show the spatial distribution of M_z at four values of H_z. (e) Resonance locus calculated by the 3D micromagnetic code (dots) along with the analytical model (solid lines).*

perpendicular field. However, one can note that the vortex core reversal is hardly seen on the magnetization curves, due to the extremely small volume of the core with respect to the micro-disk.

2.1.1 Gyrotropic mode

We now present the results of the spectroscopic MRFM study of a single NiMnSb nanodot (thickness $t = 44$ nm, radius $R = 130$ nm) in the cone state, where we reveal the influence of a perpendicular field on the gyrotropic frequency. When the external magnetic field H_z is reduced below the perpendicular saturation field of the nanodisk $H_s \simeq 6$ kOe (this value can be inferred from the field dependence of the cantilever resonance frequency, see Fig.2.2a), a single magnetic vortex is formed inside the nano-disk. Fig.2.2b shows the dynamical behavior of the disk in the cone state. The absorption peak observed in the spectra corresponds to the excitation of the gyrotropic mode in the disk. It produces a mechanical signal mainly because the contribution of the vortex core to M_z diminishes when it is excited [73]. Such signal is sensitive to the polarity of the vortex core: it is positive when the sphere magnetization and the vortex core are parallel and negative in

the opposite case. Moreover, due to the field dependence of the magnetic moment of the MRFM probe, which vanishes at remanence [109], the amplitude of the MRFM signal decreases as $|H|$ is reduced to zero.

The baseline of each spectrum in Fig.2.2b is set at the excitation frequency. The spectrum for 1.15 GHz has an intense peak at around +3.5 kOe (blue circle) corresponding to the excitation of the gyrotropic mode of the vortex core, as well as its mirror image at −3.5 kOe. The gyrotropic frequency decreases with the bias field H_z, and in the zero field ($H_z = 0$) has the value of 0.7 GHz. In the region of negative bias fields $H_z < 0$ the mode continues to exist, but the corresponding resonance peak has a negative amplitude, which indicates that now the direction of the bias field and the magnetization of the amorphous Fe MRFM nanosphere is opposite to that of the vortex core. The gyrotropic frequency continues to decrease with the same slope until the bias field value of $H_r = -2.8$ kOe, where the resonance peak abruptly changes its sign, frequency, and slope, which indicates reversal of the vortex core polarity. Below the switching field $H_z < H_r$ the gyrotropic frequency of the inverted vortex core increases like it did in positive bias fields before the core reversal. It is important to note, that upon increasing the bias field, the gyrotropic mode persists at reduced frequency until the symmetric reversal field of $H_r = +2.8$ kOe is reached, and the new reversal of the vortex core polarity takes place.

The complete phase diagram demonstrating the dynamic hysteresis loops of the gyrotropic mode frequency in a perpendicular bias magnetic field is presented in Fig.2.2c. The blue dots correspond to the case when the bias field is reduced starting from large positive values, while the red dots correspond to the opposite case, when the field is varied starting from large negative values. In the perpendicular saturated state ($|H| > H_s$), the frequency of the lowest energy mode is the well-known Kittel frequency, sligthly modified to take into account finite size effects [96].

The frequency of the gyrotropic mode in the external perpendicular magnetic field H_z can be calculated as a ratio $\omega_G(H_z) = \kappa(H_z)/G(H_z)$ of the field-dependent vortex stiffness $\kappa(H_z)$ to the field-dependent magnitude $G(H_z)$ of the z-component of the vortex gyrovector using the method of Thiele equation that was used in [65] to calculate this frequency in the case when $H_z = 0$. The gyrovector can be calculated by integration over the vortex core as follows [178]: $\boldsymbol{G} = tM_s/\gamma \int d^2\boldsymbol{\rho} \sin\Theta(\nabla\Phi \times \nabla\Theta)$, where Θ and Φ are the polar angles which parametrize the magnetization vector at point $\boldsymbol{\rho}$ in the disk. The form of this topological quantity, directed along the normal to the disk plane, and whose value corresponds to the solid angle covered by the magnetization texture on the unit sphere, is key to the gyrotropic dynamics. When the perpendicular bias field is introduced it can be written as $G(H_z) = G(0)(1 - p\cos\theta)$, where $p = \pm 1$ is the vortex core polarity, $G(0) = (2\pi ptM_s)/\gamma$ is the gyrovector in zero bias field, and θ is the polar angle of the static magnetization at the disk lateral boundary. For a sufficiently large disk radius (much larger than the radius of the vortex core) is is possible to estimate θ from the standard electrodynamic boundary conditions at the vertical boundaries of the disk as $\cos\theta = H_z/H_s$.

The field-dependent vortex stiffness $\kappa(H_z)$ can be found from the assumption that the main contribution to the vortex energy comes from the dipolar interaction of the volume magnetostatic charges created by the in-plane magnetization component of the shifted vortex outside the core [65]. In this region the in-plane magnetization components depend of the direction of the external bias field as $\sin\theta$, and the stiffness $\kappa(H_z)$, that is proportional to the square of the radial derivative of the in-plane magnetization,

is expressed as $\kappa(H_z) = \kappa(0)\sin^2\theta$, where $\kappa(0)$ is the vortex stiffness in the zero bias field defined in [65]. Thus, we can write the explicit expression for the gyrotropic mode frequency in the perpendicular bias field as

$$\omega_G(H_z) = \omega_G(0)\left(1 + p\frac{H_z}{H_s}\right), \tag{2.1}$$

where $\omega_G(0)$ is the gyrotropic mode frequency at zero bias field, which in the limit of small aspect ratio $t/R \ll 1$ can be approximated by $\omega_G(0) = (20/9)(t/R)\gamma M_s$ [65].

The dependence of the gyrotropic frequency on the perpendicular field Eq.(2.1) (solid lines in Fig.2.2c) is a direct consequence of the evolution of topology in the cone state. Moreover, it is clear from this equation that the perpendicular field induces a frequency splitting between the gyrotropic modes associated to opposite polarities, which allows to spectroscopically determine the vortex core orientation. This simple analytic theory does not account for the reversal of the vortex core polarity observed experimentally at $H_z = H_r$. Therefore, we performed micromagnetic simulations to reproduce this effect. The numerically calculated static hysteresis loop of $M_z(H_z)$ (where the vertical component of the static magnetization M_z was averaged over the disk volume) is shown in Fig.2.2d by a dashed line. Although the vortex core switching is not seen in this averaged static hysteresis loop (as already noted in Fig.2.1b), it is clearly revealed when the averaging of the static M_z component is done over the spatial region occupied by the vortex core ($\simeq 15$ nm), as demonstrated by the solid lines, where the core polarity switching appears as a jump at $|H_r| = 3.25$ kOe. The dynamic hysteresis loop (*i.e.*, the dependence of the gyrotropic mode frequency on the perpendicular bias magnetic field H_z) shown in Fig.2.2e was numerically calculated using a code which computes the full dynamic susceptibility tensor χ'' from linearization of the LLG equation around the equilibrium configuration [17]. It clearly demonstrates the effects of the bias-field-induced dynamic bistability in the field interval $|H_z| < H_r$.

It is also possible to follow the evolution of the damping of the gyrotropic mode in the cone state. This is shown in Fig.2.3b, which displays the damping ratio $d = \Delta f/(2f)$ determined by MRFM spectroscopy at several fixed perpendicular fields, by sweeping the excitation frequency f and fitting the linewidth Δf of the resonance curve. In the saturated state, which corresponds to resonance frequencies above 1 GHz (see Fig.2.3a), the damping is found to be constant and equal to the Gilbert damping parameter of the NiMnSb material, here $2.5\ 10^{-3}$. In the cone state, the damping ratio, similarly to the gyrovector, is renormalized by topology [178]. Experimentally, it increases from about $5\ 10^{-3}$ to $8\ 10^{-3}$ as the frequency decreases from 450 MHz down to 190 MHz (*i.e.*, the perpendicular field decreases from 0.65 T down to -0.15 T). Close to $H_z = 0$, the experimental value $d = d_{\text{vortex}} = 0.0075 \pm 0.001$ is in good agreement with the predicted value [66] $d_{\text{vortex}} = \alpha\,[1 + \ln(R/b)/2] \simeq 0.007$ ($R = 500$ nm and $b \simeq 15$ nm are respectively the disk and vortex core radii).

2.1.2 Spin-wave modes

MRFM also allows to detect higher frequency spin-wave modes than the gyrotropic mode in the cone state. Fig.2.4a shows several MRFM spectra of an individual 44 nm thick, 1 μm diameter disk of NiMnSb by sweeping the perpendicular bias field H_z at fixed frequencies ranging between 1.8 GHz and 3.1 GHz. The perpendicular saturation field

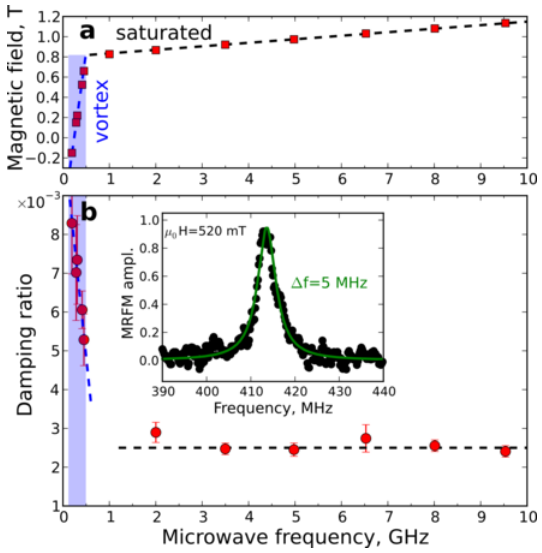

Figure 2.3: ***Damping of the gyrotropic mode.*** *The sample is $t = 44$ nm, $2R = 1$ μm NiMnSb disk. (a) Frequency – perpendicular field dispersion relation of the uniform mode in the saturated state ($\mu_0 H_z > 0.8$ T) and of the gyrotropic mode in the cone state ($\mu_0 H_z < 0.8$ T). (b) Damping ratio $d = \Delta f/(2f)$ obtained from MRFM spectroscopic measurements. The center frequency f and the frequency linewidth Δf are obtained from lorentzian fits of the resonance peaks (the inset shows such a fit at a fixed field in the cone state).*

of this disk, $H_s = 8.1$ kOe, is indicated by a dashed vertical line. When $H_z > H_s$, the sample is fully saturated along its normal, and a series of stationary spin-wave modes [96] can be observed in the blue region of the spectra. When $H_z < H_s$, the NiMnSb disk is in the vortex cone state, and up to four well-resolved spin-wave modes can still be observed at lower field, in the red region of the spectra in Fig.2.4a. It should be noted, that these modes are very similar with those observed in broadband FMR experiments performed on arrays of Permalloy disks [20].

To gain further insight about the nature of the spin-wave modes which can be excited above and below the saturation field, we have plotted in Fig.2.4b their frequency–field dispersion relation in blue and red symbols, respectively. In the saturated state, the lowest energy spin-wave mode is the most uniform mode $n = 0$ with a constant precession phase everywhere in the disk, and its dispersion relation follows a standard Kittel equation [blue continuous line]. The higher energy modes correspond to harmonics with an increasing number of precession nodes in the radial direction [96, 104]. In the vortex state, the fundamental SW mode is the gyrotropic mode (labeled 0_-), whose frequency increases linearly with the perpendicular bias field [red continuous line, Eq.(2.1)]. The higher energy modes correspond either to vortex core excitations or coupled modes between the vortex core and the disk edge, as determined from micromagnetic simulations [20]. The frequency of these modes decreases with the perpendicular magnetic field, and shows a minimum at the compensation point $H_z = H_s$. This negative slope of the frequency–field dispersion relation is related to the decrease of the effective field probed by these spin-wave modes in the unsaturated state as H_z increases. It should also be noted that the MRFM signal corresponding to these modes in the vortex state is negative, meaning that the averaged component of magnetization M_z along the applied field H_z increases at resonance, in contrast to the standard case observed in the saturated state [104].

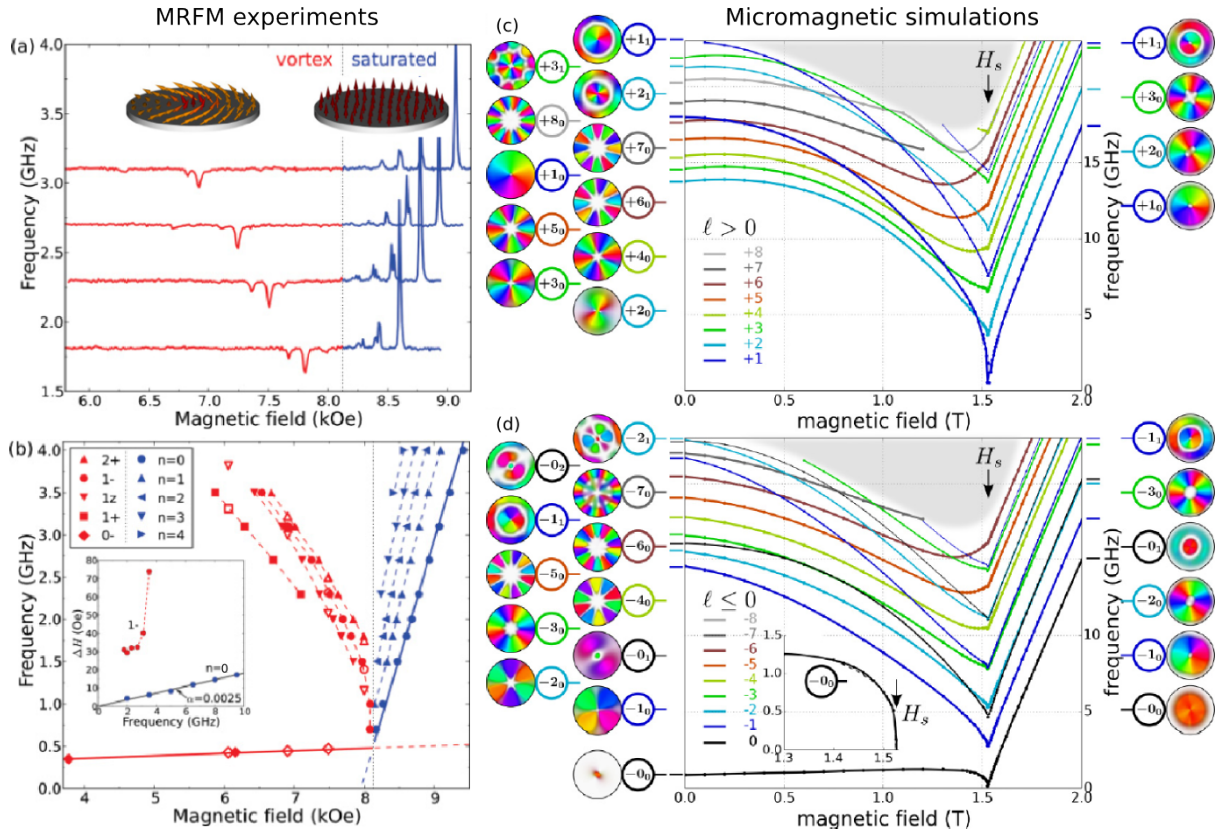

Figure 2.4: ***Spin-wave modes in the cone state.*** *(a) MRFM spectra obtained on an individual disk of NiMnSb ($t = 44$ nm, $2R = 1$ μm). (b) Dispersion relation of the different spin-wave modes observed experimentally. The inset shows the variation of the full linewidth ΔH as a function of frequency for the modes $n = 0$ and 1_-. (c), (d) Simulated spin-wave spectra of a ($t = 10$ nm, $R = 100$ nm) nano-disk as a function of the perpendicular field H_z. Modes are labeled (ℓ_m), respectively, the azimuthal and radial indices. The two panels differentiate spin-waves depending on their sense of gyration: (c) $\ell > 0$ and (d) $\ell \leq 0$. Snapshot images of the eigenvectors in the vortex ($\mu_0 H_z = 0$ T) and saturated states (2 T) are shown on the left and right sides, respectively (color code: amplitude/phase = luminance/hue). The inset in (d) shows a zoomed-in view of the softening of the gyrotropic mode at H_s.*

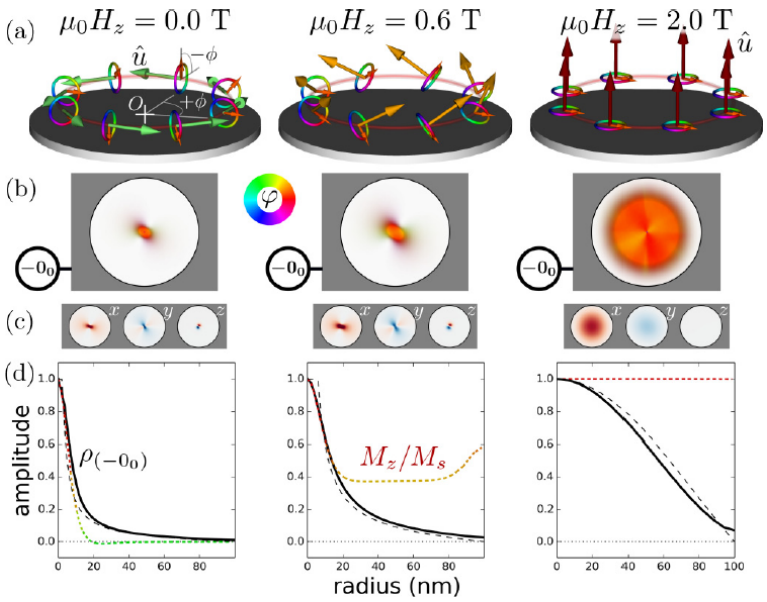

Figure 2.5: ***Spatial profile of the gyrotropic mode.*** *(a) Dynamical magnetization (short arrow) in the local frame of the magnetization texture (long arrow) for the mode with a uniform phase, from left to right in the vortex, cone, and saturated states. (b) Corresponding eigenmode profiles using the amplitude/phase representation and (c) the cartesian directions. (d) Simulated (solid) and analytical (dashed) radial profiles of the dynamic magnetization; the simulated static magnetization M_z is shown using a dotted color line.*

To better understand the transition between the vortex cone state and the perpendicularly saturated state, we use the SpinFlow3D micromagnetic simulation package to calculate the eigenstates of the lossless linearized Landau-Lifshitz equation [175]. The results of these simulations are shown in Figs.2.4c and d. Although the material and geometrical parameters are not the same as for the experimentally investigated NiMnSb sample, we emphasize that the simulated frequency–field relation dispersions are in good qualitative agreement with the data.

Three remarkable features are observed in these simulations. The first one is the apparent one-to-one mapping between the eigenmodes in the cone state and the saturated state. Knowing that in the saturated state the spin-wave spectrum is fully mapped by an azimuthal (ℓ) and a radial (m) index [104], it suggests that this labeling extends all the way down to the vortex state at remanence. This is confirmed by a careful inspection of the eigenvectors shown on the left and right sides of Figs.2.4c and d. We note that a recent work on the sum rule invariance of the magnetic susceptibility has also underlined the continuity of the spectrum independently of the magnetization texture [177]. The second remarkable feature is the behavior of the lowest energy mode shown in black in Fig. 2.4d. This mode is the gyrotropic mode below H_s and the Kittel mode above it. Its frequency uniquely vanishes at H_s, while the eigenmodes above the gyrotropic mode always resonate at finite frequency. Similarly to the Kittel mode in the saturated state, the gyrotropic mode can be continuously viewed as the uniform phase precession, but on top of the non-uniform cone state magnetization texture, as shown in Fig.2.5. In particular, it is interesting to follow how the spatial profile of this eigenmode evolves from the pure gyrotropic profile at zero field [74] to the Bessel profile in the saturated state, see Fig.2.5d. The third one is that, contrary to the saturated state where the modes evolve in parallel

as a function of the applied magnetic field, in the cone state the higher-order energy levels can intercept each other. This suggests that a careful analysis of the continuity of the mode character is required: as a matter of fact, mode hybridization can be observed at level anticrossings [175].

Related publications

1. G. de Loubens, A. Riegler, B. Pigeau, F. Lochner, F. Boust, K. Y. Guslienko, H. Hurdequint, L. W. Molenkamp, G. Schmidt, A. N. Slavin, V. S. Tiberkevich, N. Vukadinovic, O. Klein, *Bistability of Vortex Core Dynamics in a Single Perpendicularly Magnetized Nanodisk*, Phys. Rev. Lett. **102**, 177602 (2009).
2. V. Castel, J. Ben Youssef, F. Boust, R. Weil, B. Pigeau, G. de Loubens, V. V. Naletov, O. Klein, N. Vukadinovic, *Perpendicular ferromagnetic resonance in soft cylindrical elements: Vortex and saturated states*, Phys. Rev. B **85**, 184419 (2012).
3. B. Taurel, T. Valet, V. V. Naletov, N. Vukadinovic, G. de Loubens, O. Klein. *Complete mapping of the spin-wave spectrum in a vortex-state nanodisk*, Phys. Rev. B **93**, 184427 (2016).

2.2 Dynamical reversal of the vortex core

The excitation of the gyrotropic motion leads to a dynamical distortion of the vortex core profile, as predicted by micromagnetic simulations and theoretical analysis [73], and established experimentally [188]. In a period of the core motion, the in-plane magnetization enclosed by the orbit of the core undergoes a full inversion on a time scale that is the shortest in the vicinity of the core. When the vortex core moves between two locations, the in-plane magnetization situated at the middle of the chord of the trajectory must also undergo a full inversion during the same time lapse. As a result, a strong *gyrofield* ($\propto \boldsymbol{M} \times \dot{\boldsymbol{M}}/(\gamma M_s)$) [73] perpendicular to the dot plane and opposite to the polarity of the core is created in this region. It leads to a distortion of the vortex core profile and a tail of perpendicular magnetization opposite to the core appears. This distortion increases with the linear velocity of the vortex core and opposes the core polarity, until the critical velocity $V_c \simeq 1.66\gamma\sqrt{A_{\text{ex}}}$ (A_{ex} is the exchange constant of the material) is reached and the vortex core polarity is reversed [115].

In zero magnetic field, dynamical control of the polarity is difficult due to the degeneracy of the gyrotropic frequencies associated to opposite polarities $p = \pm 1$, which can lead to multiple core switching [200, 87]. Still, selective core polarity reversal was demonstrated using a circularly polarized microwave magnetic field because the sense of the core rotation is linked by a right-hand rule to its polarity [34]. Control of polarity switching was also be achieved by precise timing of non resonant magnetic field pulses [196]. It is important to note that resonant amplification of the vortex gyrotropic motion enables to reverse the core polarity with minimum excitation power [34, 188], as it allows to concentrate the energy in a narrow frequency band. In this scheme, the damping ratio is a crucial parameter because it controls the minimum amplitude of the resonant excitation required to switch the core [115], therefore it would be nice to probe it close to the reversal threshold, which is a highly nonlinear phenomenon.

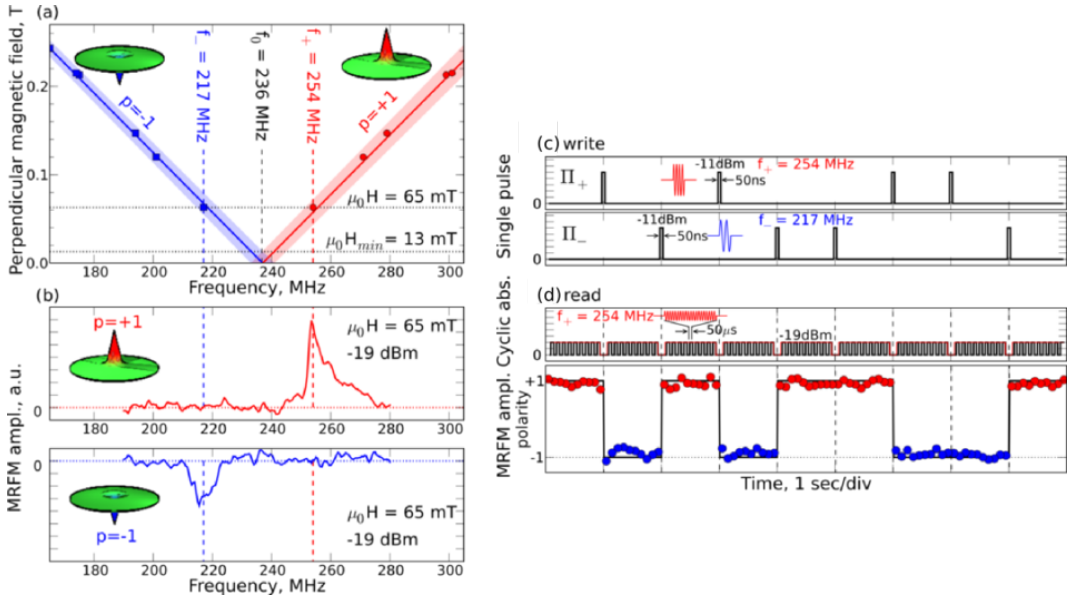

Figure 2.6: ***Frequency-controlled magnetic vortex memory.*** *(a) Frequency splitting induced by a perpendicular magnetic field between the gyrotropic modes corresponding to the two opposite core polarities $p = \pm 1$. The shaded area illustrates the broadening associated with the linewidth of the gyrotropic mode. (b) The red and blue traces are the MRFM absorption signals measured at $\mu_0 H_z = 65\ mT$ for $p = \pm 1$. (c) The writing is performed every second by applying a single microwave pulse ($\tau_w = 50\ ns$, $P_w = -11\ dBm$) whose carrier frequency is tuned at either f_+ or f_-. (d) The reading ($P_r = -19\ dBm$) is performed continuously between the writing pulses by MRFM using a cyclic absorption sequence at the cantilever frequency ($\sim$ 10 kHz or half-period 50 μs).*

We also emphasize in most of the experimental studies, vortex core reversal events are detected using time-resolved imaging techniques based on X-ray magnetic circular dichroism, which are very powerful, as they enable direct determination of the vortex core trajectory [188]. However, they require to average many events and the interpretation can become more complicated due to multiple reversal processes.

2.2.1 Deterministic reversal under a perpendicular magnetic field

In order to investigate the coupling between resonant microwave pulses and vortex dynamics near the core reversal threshold, we use MRFM in combination with a bias magnetic field applied perpendicularly to the disk plane, that induces two distinct resonant gyrotropic frequencies associated to opposite core polarities as shown in Fig.2.2c and Fig.2.6a. As explained in section 2.1.1, this frequency splitting can be used for a simple, single shot spectroscopic reading (Fig.2.6b) of the polarity state using MRFM. Moreover, it enables deterministic reversal of the vortex core by single microwave pulses: once inverted, the final polarity state is out of resonance with the microwave pulse, so that the polarity cannot be switched back, see Figs.2.6c and d. This allowed us to propose a frequency-controlled magnetic vortex memory [145].

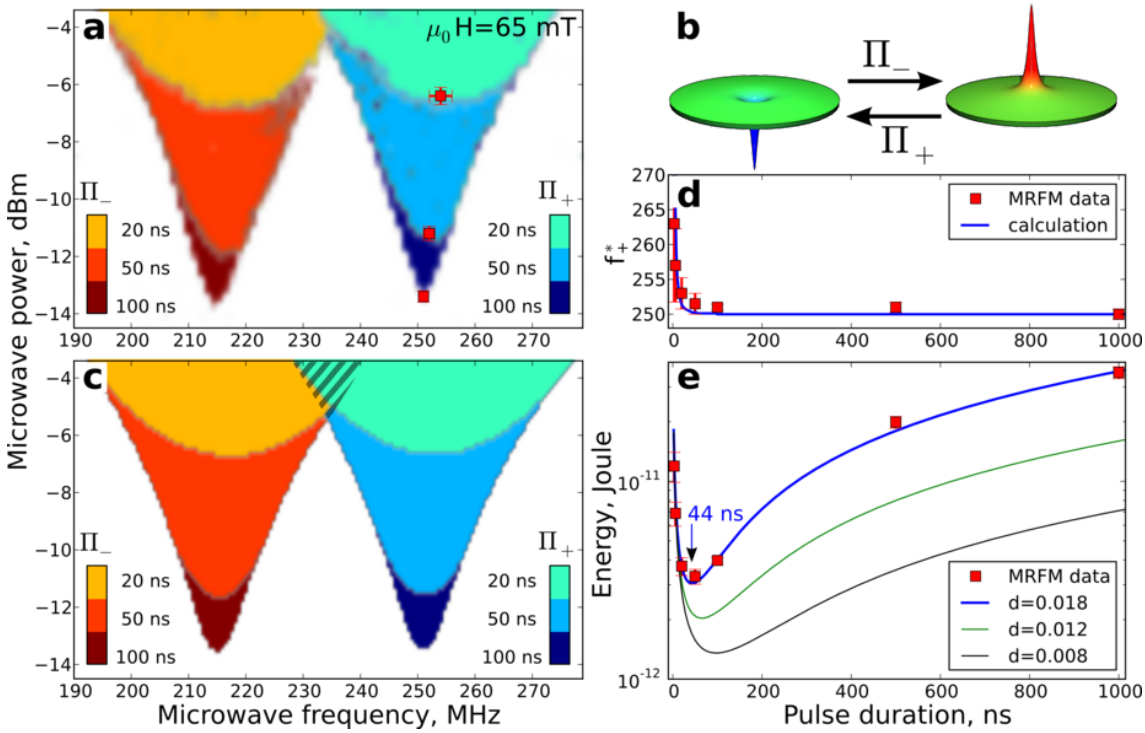

Figure 2.7: ***Vortex core resonant reversal by a single microwave pulse.*** *(a) Efficiency of the* Π_- *and* Π_+ *pulses (see panel b) to reverse the vortex core at* $\mu_0 H_z = 65$ *mT measured as a function of power and frequency. For each pulse type, a colored pixel (*Π_-*: red shade,* Π_+*: blue shade) marks a successful reversal. The transparency gives the switching probability averaged over 16 attempts. Experiments corresponding to three values of the pulse duration w are displayed. For each w we define* (f_+^*, P^*)*, the optimal working point of the* Π_+ *pulse located at the bottom of the corresponding contour plot. (c) Numerical calculation of the experiments presented in (a). This calculation is not valid within the shaded area, where multiple vortex core reversals can occur. (d), (e), Experimental (squares) and calculated (lines) dependences on w of the optimal frequency* f_+^* *(d) and of the optimal pulse energy* $E^* = P^* w$ *(e) on the pulse duration. The best agreement is obtained for a damping ratio* $d^*_{forced} = 0.018$*. The absolute value of the energy is also fitted in the calculation, which enables to extract the critical velocity for vortex core reversal,* $V_c \simeq 190$ *m/s.*

2.2.2 Optimal and coherent control

We also explored in details the efficiency of single microwave pulses to switch the vortex core, depending on their duration, frequency and power, see Fig.2.7. Π_- pulses are defined as single pulses that reverse the polarity from $p = -1$ to $p = +1$ and Π_+ pulses from $p = +1$ to $p = -1$ (Fig.2.7b). The contour plots presented in Fig.2.7a with different shades of red (blue) show the superposition of the results for Π_- (Π_+) pulses with three different durations w: 100, 50 and 20 ns (an opaque pixel marks pulse settings for which reversals are recorded with a 100% success rate, while a blank pixel means that no reversal is recorded.). The frequency splitting introduced by the perpendicular bias field clearly appears. Due to the resonant character of the investigated switching process, a pronounced minimum in the power level required to reverse the vortex core is observed at a frequency f_-^* (f_+^*) close to the gyrotropic frequency associated to the initial core polarity, for each duration of the Π_- (Π_+) pulses. This frequency discrimination introduced by H_z allows most of the recorded results to be fully deterministic.

The minimum power P^* required to reverse the core polarity increases as the pulse duration w decreases. We have plotted the dependences on w of the optimal frequency f_+^* (Fig.2.7d) and of the optimal pulse energy $E^* = P^* w$ (Fig.2.7e). There is a clear minimum in the optimal pulse energy that occurs around $w = 50$ ns. The position of this minimum yields an estimation of the characteristic decay time. If the pulse duration exceeds this characteristic time, the vortex core dynamics reaches steady-state before the end of the pulse, *i.e.*, the pulse duration is uselessly too long. On the contrary, if the pulse duration is shorter than this characteristic time, some energy is wasted outside the resonance line. Due to the transient response of the vortex core to the excitation pulse, the optimal frequency f_+^* measured for pulses shorter than 50 ns shifts to higher frequency (see Fig.2.7d), a general behavior of any harmonic oscillator forced on time scales shorter than its decay time.

To be more quantitative, we have performed a numerical calculation based on the analytical approach developed for zero applied magnetic field [115], with the new ingredient that due to the bias perpendicular field, f_- and f_+ are distinct frequencies. Fig.2.7c illustrates the good agreement of the model with the experimental data of Fig.2.7a on the whole range of pulse parameters. The behavior of the optimal pulse energy as a function of w can be reproduced with an analytical formula where the damping ratio d^*_{forced} is an adjustable parameter (blue solid line in Fig.2.7e). The best fit is obtained for $d^*_{\text{forced}} = 0.018$. This value, inferred in the highly nonlinear forced regime, is more than twice larger than the one measured in the small oscillation regime of the gyrotropic mode, found to be $d = 0.0075$ (see Fig.2.3b).

Next, we investigate in Fig.2.8 the vortex core dynamics in the free decay regime by monitoring the core reversal induced by two consecutive microwave pulses. In these experiments, the pulse duration is set to $w = 9$ ns and the power to $P = -1.8$ dBm, *i.e.*, slightly below the minimum power $P^* = -1$ dBm required to reverse the core polarity p for such a short pulse. Contrary to a single pulse, two pulses separated by a delay τ (Fig.2.8a: Π_-–τ–Π_-; Fig.2.8b: Π_+–τ–Π_+) can reverse p. The striking oscillatory dependence on the pulses carrier frequency and on the delay τ enlightens the phase coherent coupling between the vortex gyrotropic motion and the microwave excitation. During the pulse duration, the gyrotropic motion is forced at the pulse frequency, while in the free decay regime, the core oscillates towards its equilibrium position at its natural frequency, therefore acquiring

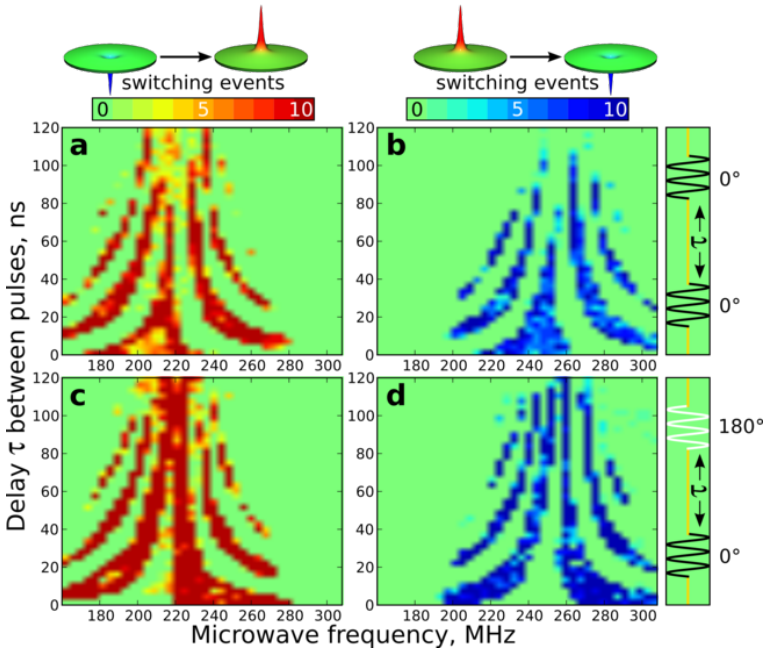

Figure 2.8: ***Oscillatory dependence on frequency and delay between two consecutive pulses of the vortex core reversal efficiency.*** *(a-d) Number of switching events out of ten attempts as a function of the delay τ separating the two pulses ($w = 9$ ns, $P = -1.8$ dBm) and of the carrier microwave frequency (stepped by increments of 3 ns and 4 MHz, respectively). The bias magnetic field is $\mu_0 H_z = 65$ mT. The initial polarity state is $p = -1$ in the left graphs (a, c) and $p = +1$ in the right graphs (b, d). As depicted in the right-side panels, the phase difference between the two pulses is zero in the upper graphs (a, b) and π in the lower graphs (c, d).*

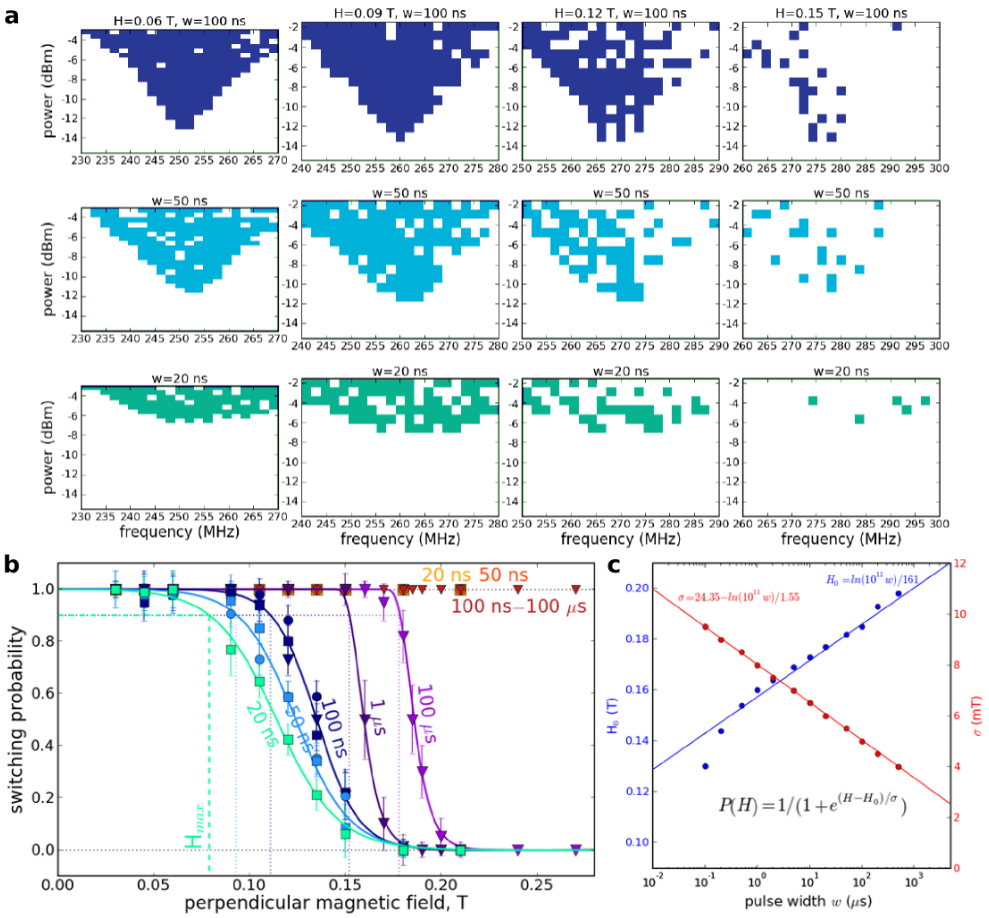

Figure 2.9: ***Hard reversal: switching the vortex core against the perpendicular field.*** *(a) Evolution of the core reversal diagrams of Fig.2.7 (from polarity parallel to anti-parallel to the bias perpendicular field) as a function of the applied perpendicular field, from 0.06 (left) to 0.15 T (right). No averaging was performed. (b) Dynamical reversal probability vs. perpendicular field for increasing microwave pulse durations. The "easy" switching is represented by orange-red-brown symbols while the "hard" reversal are the green-blue-violet symbols. The parameters of the fitting curves (continuous lines) are plotted in panel (c).*

a phase shift with respect to the excitation carrier. As a result, the efficiency of the second pulse to drive the vortex core to the reversal threshold depends on the microwave frequency and on the delay between pulses in an oscillatory manner (the oscillation period scales as the inverse frequency detuning). To illustrate further this effect of coherence, similar experiments with a π phase shift introduced between the two pulses have been carried out. It is clear that the regions where successful reversal are observed in Figs.2.8c and d are complementary to those in Figs.2.8a and b, respectively. Thus, phase control of the microwave excitation can trigger vortex core switching.

Hence, Figs.2.7 and 2.8, demonstrate optimal and coherent control of vortex polarity by single- and double-microwave pulse sequences. We note that at much higher powers than investigated in this study, we observe interesting patterns in the switching diagrams, because the regions of Π_- and Π_+ reversals overlap. Moreover, we emphasize that upon increasing of the bias perpendicular field, which was set here to a rather small value, a clear asymmetry appears in the switching probability between "easy" and "hard" vortex core

reversals (from anti-parallel to parallel to the field, and vice versa), but not in the minimal switching power (Fig.2.9a). The hard switching probability sharply drops beyond a critical field, which depends on the pulse duration and power (Fig.2.9b). This behavior was not commented at all in studies of vortex core reversal in the presence of a perpendicular field using micromagnetic simulations [98, 201].

Related publications

1. O. Klein, G. de Loubens, B. Pigeau. *Dispositif de stockage à tourbillon magnétique.* Année de dépôt 23/04/2009, WO/2010/122126.
2. B. Pigeau, G. de Loubens, O. Klein, A. Riegler, F. Lochner, G. Schmidt, L.W. Molenkamp, V.S. Tiberkevich, A.N. Slavin, *A frequency-controlled magnetic vortex memory*, Appl. Phys. Lett. **96**, 132506 (2010).
3. B. Pigeau, G. de Loubens, O. Klein, A. Riegler, F. Lochner, G. Schmidt, L.W. Molenkamp, *Optimal control of vortex-core polarity by resonant microwave pulses*, Nature Phys., **7**, 26–31 (2011).

2.3 Nonlinearity of the confinement potential

In the previous section, it has been seen that nonlinearities of the gyrotropic dynamics can lead to the reversal of vortex core. Without reaching this extreme situation, it is also crucial to understand the nonlinear frequency shift of vortex-state spin torque oscillators (see section 3.2), when they are driven in the large amplitude regime. The most common way to describe the gyrotropic dynamics is based on the Thiele equation, where the vortex core is parametrized by its vector position $\boldsymbol{X}$ inside the magnetic dot. For a circular nanodot, the magnetostatic energy is isotropic in the dot plane and it can be expressed as a series expansion of even powers of $\boldsymbol{X}$:

$$W^{(\mathrm{M})} = W_0^{(\mathrm{M})} + \frac{1}{2}\kappa|\boldsymbol{X}|^2 + \frac{1}{4}\kappa'|\boldsymbol{X}|^4 + \mathcal{O}(|\boldsymbol{X}|^6)\,. \tag{2.2}$$

The parabolicity of the confinement, which determines the linear gyrotropic frequency, is well characterized and understood [65]. Still, a precise measurement of higher order terms is lacking. Furthermore, accurate theoretical expressions for the latter are not available.

In the following, we use the MRFM technique and a high quality single crystal FeV nano-disk to determine the anharmonic coefficient $\lambda \equiv \kappa'/\kappa$ through a variational approach, *i.e.*, by monitoring the change of the frequency of the gyrotropic mode probed in the small excitation regime upon the large static displacement $\boldsymbol{X}_0$ of the vortex core equilibrium position. We note that former attempts to perform this measurement were unsucessful, instead they revealed inhomogeneities of the potential well leading to the local pinning of the core [31, 19]. We also present some data of the reciprocal experiments, where the gyrotropic dynamics is probed in the large amplitude dynamics with the equilibrium position of the core being in the center of the nano-disk.

2.3.1 Direct measurement of the anharmonicity

In the experiment presented in Figs.2.10a and b, we rely on the nonuniform stray field of the magnetic spherical MRFM probe to shift the vortex core away from the nanodot

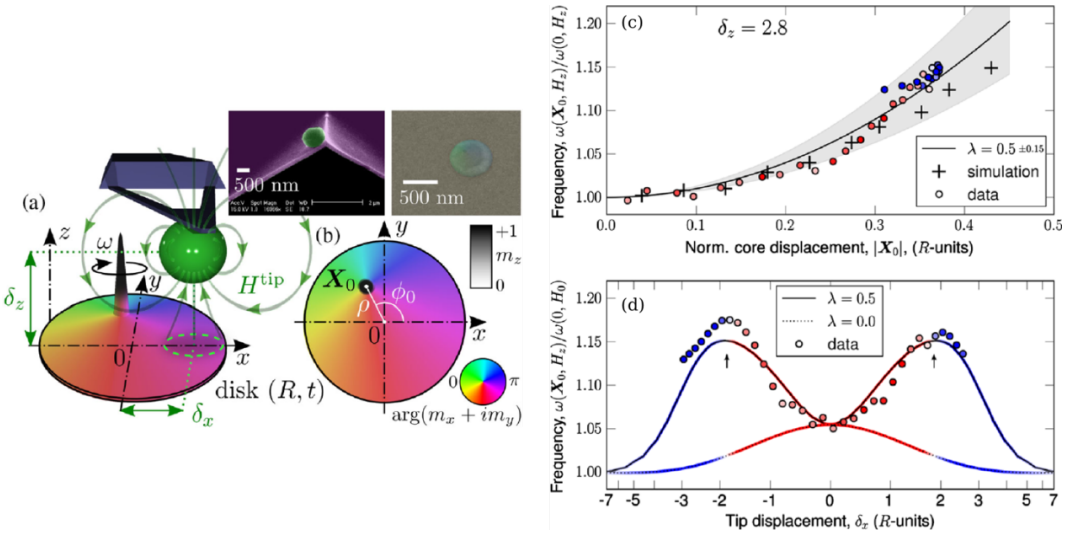

Figure 2.10: ***MRFM spectroscopy of the vortex core confinement potential.*** *(a) Side and (b) top views of the experimental setup: the stray field of the MRFM tip is used to displace the static position $\boldsymbol{X}_0$ of the vortex core. The insets are microscopy images of the magnetic tip (a 700 nm Fe nanosphere) and disk sample (a $t = 27$ nm, $2R = 600$ nm FeV disk). (c) Plot of the relative variation of eigenfrequency of the gyrotropic mode as a function of $|\boldsymbol{X}_0|$. A fit by a parabola yields $\lambda = 0.5 \pm 0.15$. The crosses are the results of micromagnetic simulation. (d) Relative variation of the eigenfrequency as a function of the tip displacement. The lines show the analytical behaviors for a vanishing and a finite anharmonic coefficient using Eq.2.3.*

center. We record the gyrotropic resonance of the nano-disk as a function of the lateral position of the MRFM tip above it (the scan height is 0.9 μm), and plot its relative frequency against the tip displacement in Fig.2.10c. The equilibrium position $\boldsymbol{X}_0$ of the vortex core can be calculated by minimizing the sum of the magnetostatic self-energy of the vortex ground state and the Zeeman energy with the external magnetic field, composed of the homogeneous perpendicular bias field and inhomogeneous MRFM tip strayfield. This allows to plot the experimental relative frequency shift against $\boldsymbol{X}_0$ and to fit it to

$$\frac{\omega(\boldsymbol{X_0}, H_z)}{\omega(0, H_z)} = 1 + 2\lambda\,|\boldsymbol{X_0}|^2 + \mathcal{O}(|\boldsymbol{X}|^4)\,, \tag{2.3}$$

as shown in Fig.2.10b. In our experiment, the maximal shift of the core from the disk center is found to be about 0.35 times its radius, which results in an increase of the gyrotropic frequency by about 15%. The anharmonicity extracted from the MRFM data is $\lambda = +0.5 \pm 0.15$ (see continuous line), in agreement with micromagnetic simulations (see crosses). Our measurements are also compatible with recent analytical expressions [126] and with the numerical results obtained in ref. [49], in which the perpendicular field dependence of spin-transfer-induced vortex dynamics in the nonlinear regime is studied.

2.3.2 Nonlinear ferromagnetic resonance in the vortex state

We also conducted FMR measurements of the gyrotropic dynamics in the nonlinear regime as a function of the excitation power. The corresponding spectra shown in Fig.2.11 are acquired in the standard mode of MRFM spectroscopy, *i.e.*, with the MRFM probe positioned above the center of the nano-disk to preserve the axial symmetry. We note

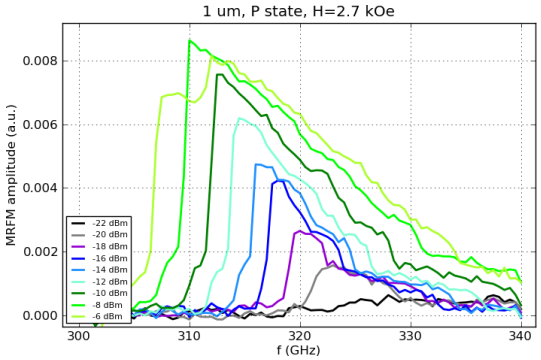

Figure 2.11: ***FMR of the gyrotropic mode in the nonlinear regime.*** *Evolution with the increasing microwave power of the MRFM signal associated to the gyrotropic dynamics of a vortex-state NiMnSb micro-disk ($t = 44$ nm, $2R = 1$ μm).*

that this axial symmetry is necessary to avoid the additional complexity of nonisotropic potential like for instance in square-shaped elements [46]. It is found that the maxima of the resonance curves shift towards *lower* frequency (foldover red shift) as the excitation power is increased, which seems to be in disagreement with the previous determination of a *positive* anharmonic coefficient. However, one should not directly compare these two studies, as the previous variational study (Fig.2.10) is performed in the linear regime of gyrotropic dynamics, whereas the foldover study (Fig.2.11) is performed in the strongly nonlinear regime. In the latter case, one cannot neglect the effects of deformation of the vortex core, which are not taken into account in the Thiele approach. When the gyrotropic mode is excited in the nonlinear regime, other spin-waves on top of the moving background cannot be neglected, which give rise to a vortex mass [68] and qualitatively affects its dynamics. Some other studies have shown that it is the thickness of the magnetic element that determines whether the resonance frequency shifts to the red or to the blue (thicker elements exhibiting red shift) [46]. In principle, this could also be interpreted introducing a vortex mass, which becomes non negligible for thick vortex-state platelets, and should be taken into account to interpret the excitation spectrum even in the linear regime [72]. Finally, we note that the nonlinear contribution to the damping complicates the analysis of the foldover experiment as well.

Related publications

1. O. V. Sukhostavets, B. Pigeau, S. Sangiao, G. de Loubens, V. V. Naletov, O. Klein, K. Mitsuzuka, S. Andrieu, F. Montaigne, K. Y. Guslienko, *Probing the Anharmonicity of the Potential Well for a Magnetic Vortex Core in a Nanodot*, Phys. Rev. Lett. **111**, 247601 (2013).

Résumé en français

La technique MRFM est suffisamment sensible pour sonder la dynamique du cœur de vortex (rayon $\simeq$ longueur d'échange) dans des nano-disques isolés. Nous avons étudié en détail la transition entre l'état saturé et l'état vortex en présence d'un champ magnétique perpendiculaire d'un point de vue spectroscopique, qui est accompagnée par une évolution continue de leurs spectres d'onde de spin (Fig.2.4). Nous avons démontré que la fréquence du mode gyrotropique, le mode de plus basse énergie qui correspond à une rotation du cœur autour de sa position d'équilibre, dépendait linéairement du champ perpendiculaire appliqué en raison de la déformation de la texture du vortex par ce dernier. De plus, ce dernier permet de lever la dégénérescence en fréquence des modes gyrotropiques associés aux polarités $p = \pm 1$, ce qui permet une détermination simple de l'orientation du cœur de vortex (Fig.2.2). Cela nous a permis de proposer une mémoire magnétique stockant l'information dans la polarité, et basée sur son contrôle déterministe par retournement dynamique sous champ perpendiculaire (Fig.2.6). En effet, lorsque le mode gyrotropique est excité à suffisamment grande amplitude, le profil d'aimantation autour du cœur de vortex se déforme et une instabilité dynamique aboutit à son renversement. Nous avons déterminé l'énergie optimale à injecter dans le système pour induire ce processus résonant, et avons démontré un contrôle cohérent de la polarité par des séquences d'impulsion micro-ondes (Fig.2.7). Ces expériences ont aussi permis de mesurer un temps de relaxation deux fois plus court dans ce régime fortement non-linéaire que dans le régime linéaire.

La technique MRFM a également été utilisée pour déterminer l'anharmonicité du potentiel de confinement magnétostatique du cœur de vortex dans un nano-disque, qui intervient dans la tunabilité de oscillateurs à transfert de spin basés sur le mode gyrotropique. Le champ de fuite de la sonde MRFM permet en effet de déplacer la position d'équilibre du cœur de vortex et de détecter la variation de fréquence du mode gyrotropique résultante (Fig.2.10). Les expériences sont en accord avec les simulations micromagnétiques et de récents calculs analytiques.

Chapter 3

Spin torque nano-oscillators

Spin torque nano-oscillators (STNOs) are spintronic devices capable of generating a tunable oscillation voltage in the microwave range while being biased by a dc current. They are based on two reciprocal physical phenomena, the spin transfer and magnetoresistive effects. Their microwave properties are directly related to the magnetization dynamics excited in the heterostructure and to its magnetoresistance properties. A striking particularity of such devices compared to other oscillators is their strong nonlinear properties [163], that are inherited from the equation of motion of magnetization Eq.(1.1). From a fundamental point of view, this makes them a very unique platform to study highly nonlinear oscillators, which are seldom in nature. From a practical point of view, this yields very interesting and attractive properties for applications. In particular, since the oscillation frequency strongly depends on the amplitude of the magnetization dynamics, and the latter can be varied by the injected spin polarized current, the emission frequency of spin torque oscillators is highly tunable. Moreover, these large nonlinearities make STNOs very sensitive to external stimuli. This has advantages, because STNOs can easily adapt their auto-oscillation frequency to phase-lock to an external signal, or synchronize to other oscillators. But this has also drawbacks, as their sensitivity to noise is exacerbated by the nonlinear phase-amplitude coupling.

From these general considerations, is is clear that the spectroscopic study of heterostructures is crucial to understand and improve STNOs characteristics. As a matter of fact, these are the energy, relaxation and nonlinear properties of STNOs spin-wave eigenmodes that determine their emission frequency and their spectral purity. Moreover, their spatial symmetries impose their selection rules and indicate which coupling mechanisms can be at play intra- or inter-STNOs.

Very early we realized that despite the growing literature on the topic, there was no in-depth investigation of magnetization dynamics in a very simple and high symmetry STNO, which would allow a comprehensive understanding of its high frequency properties. Therefore, we chose to study in a pedestrian way the archetype of STNO, namely a circular spin-valve Py|Cu|Py (Py=$Ni_{80}Fe_{20}$) nanopillar of diameter 200 nm, with a thick 15 nm Py "fixed" layer, and a thin 4 nm Py "free" layer [1]. In its perpendicularly saturated configuration, the high cylindrical symmetry allows to develop an analytical approach to identify the spin-wave modes [96, 104] and to quantitatively evaluate the influence of spin transfer torque on the free layer dynamics [163].

[1] This sample, as well as all others in this chapter, were provided by the UMR CNRS/Thales team of Julie Grollier and Vincent Cros.

In section 3.1, we identify its spin-wave eigenmodes and their selection rules by MRFM spectroscopy. Then, by quantitatively monitoring its emitted power we unambiguously identify the first spin-wave mode to auto-oscillate in the autonomous regime, while driven by spin transfer torque. We also study the case of slightly broken axial symmetry by tilting the applied magnetic field 2° away from the normal to the plane, where a regime of bi-modal excitation is observed, and some nonlinear coupling between the two auto-oscillating modes is identified.

In section 3.2 we study by means of high frequency transport techniques the very same STNO in a configuration where a magnetic vortex is stabilized in both magnetic layers. We detect a highly coherent auto-oscillating mode, which corresponds to the coupled dynamics of the thick and thin vortex-state layers. We also reveal the influence of damped spin-wave modes on the spectral purity of the spin-transfer-driven dynamics in this system. Moreover, we demonstrate that the latter is very efficiently synchronized to a weak external microwave field, since perfect phase-locking is observed.

In the last section 3.3, we investigate the possibility of mutual synchronization of STNOs. The main idea here is to replace the external microwave field by the dipolar stray field of an adjacent STNO. We first present an original MRFM spectroscopic measurement of the dynamical dipolar coupling in adjacent nanomagnets. We then perform the study of mutual synchronization on pairs of STNOs in the vortex state (each STNO is similar to the previously well characterized single STNO), and demonstrate that the strength of the dipolar interaction is controlled by the relative alignment of vortex polarities in the thick Py layers. Finally, we go one step further and introduce an external source in the game, which can be considered as a third reference oscillator and enables to determine the strength and phase shift of the dipolar coupling between the two STNOs.

3.1 Perpendicularly magnetized nanopillar

3.1.1 Spin-wave spectroscopy

The sample design used in this study is presented in Fig.3.1. Its originality lies in the two independent excitation circuits, which are patterned around the spin-valve nanopillar to allow the generation of a in-plane microwave field h_{rf} (blue tone) and the injection of a microwave current perpendicular-to-plane through the nano-pillar i_{rf} (red tone). The second circuit also allows the injection of a bias dc current through the sample, to apply spin transfer torque. The comparative spectroscopic study performed by MRFM at 8.1 GHz on the normally magnetized spin-valve nano-pillar is presented in Figs.3.1a and b. In these experiments, there is no dc current flowing through the device, and the spectra are obtained in the small excitation regime. Panel (a) shows the spin-wave spectrum excited by the uniform microwave field h_{rf}, while panel (b) displays the spectrum excited by the microwave current i_{rf}. The striking result is that these two spectra are different: none of the modes excited by h_{rf} is present in the spectrum excited by i_{rf}, and vice versa.

Considering the high cylindrical symmetry of the sample configuration, the general theory of linear spin-wave excitations can be used to classify and calculate quite accurately the frequencies of the spin-wave eigenmodes using Eq.(1.2). The full treatment, which also takes into account the dynamical dipolar coupling between the two magnetic layers, is presented in ref. [134]. Here, we only present the results of full 3D micromagnetic simu-

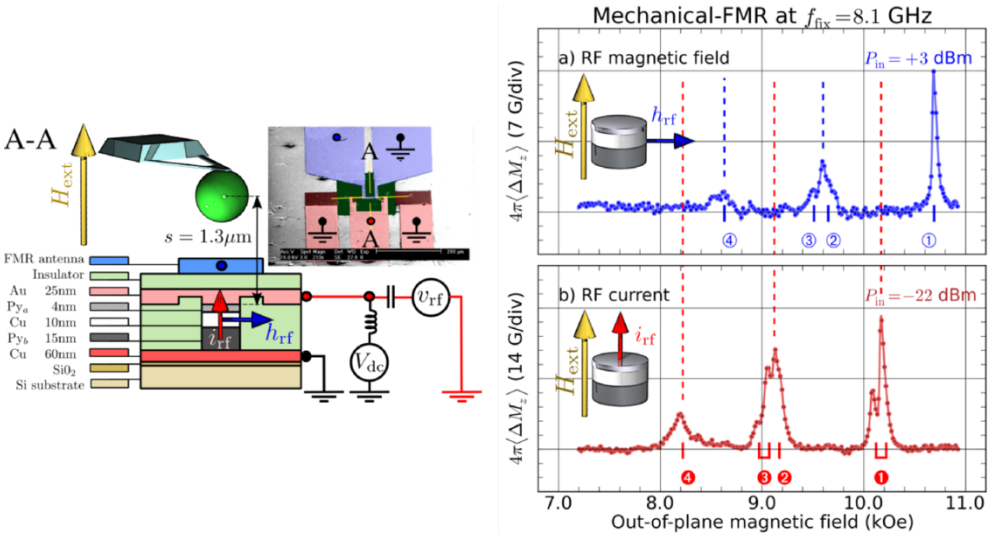

Figure 3.1: ***Comparative spin-wave spectroscopy of a spin-valve nanopillar.*** *Schematic representation of the experimental setup and sample design. The latter is a circular Py|Cu|Py nanopillar. The inset is a microscopy image of the two independent excitation circuits: in blue the circuit allowing the generation of an rf in-plane magnetic field (h_{rf}, blue arrow); in red the circuit allowing the injection of an rf current perpendicular-to-plane through the nano-pillar (i_{rf}, red arrow). The corresponding experimental spin-wave spectra at 8.1 GHz are presented in (a) and (b), respectively.*

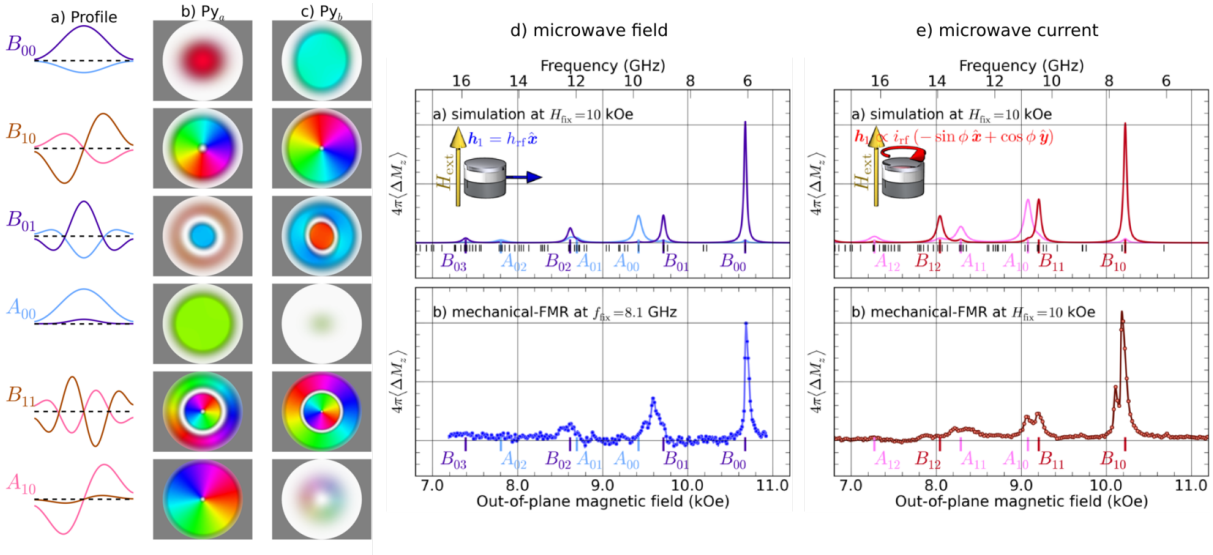

Figure 3.2: ***Micromagnetic simulations of the spin-wave eigenmodes.*** *(a) Simulated precession profiles across the thin (light color) and thick (dark color) Py layers. Columns (b) and (c) show the dynamics in the thin and thick Py layers, respectively. Panels (d) and (e) show the comparison between the simulated (top) and the experimental (bottom) spectra, excited respectively by h_{rf} and i_{rf}. The peaks are labeled according to their precession profiles shown in panel (a).*

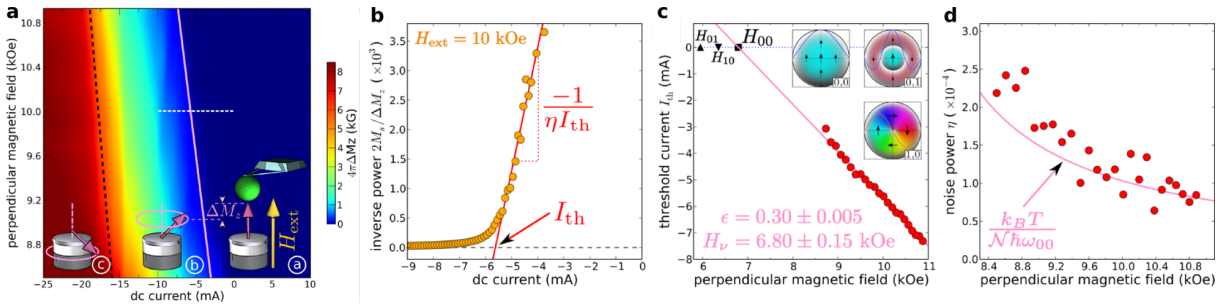

Figure 3.3: ***Quantitative MRFM study in the autonomous regime.*** *(a) Phase diagram of the STNO autonomous dynamics measured by MRFM. (b) Determination of the threshold current I_{th} and noise power η at $H_{ext} = 10$ kOe, from the inverse MRFM signal in the subcritical regime. Dependencies of the threshold current (c) and noise power (d) on the perpendicular magnetic field.*

lations, using a finite element code that calculates the eigenstates of the lossless linearized Landau-Lifshitz equation. The simulated precession profiles in both magnetic layers, and the comparision of the simulated and experimental spectra are shown in Fig.3.2. As can be seen in panels (d) and (e), there is really an excellent agreement between the MRFM data and simulations. From the inspection of the spin-wave mode profiles in columns (b) and (c), it is found that the spatially uniform rf field excites the axially symmetric modes having azimuthal index $\ell = 0$, and that the rf current flowing through the nanopillar excites the modes having azimuthal index $\ell = +1$, due to the orthoradial symmetry of the induced Oersted field. Moreover, one observes that each eigenmode is slightly hybridized between thick and thin layers individual modes, due to the dipolar interaction. The modes dominated by the thick layer (labeled by $B_{\ell m}$) induce a rather large out-of-phase dynamics in the thin layer, while modes dominated by the thin layer (labeled by $A_{\ell m}$) drive a rather weak in-phase precession in the thick layer.

3.1.2 Auto-oscillations driven by spin transfer torque

Next, we continue to investigate the dynamics of the same STNO in the normally magnetized configuration, but this time in the autonomous regime, *i.e.*, under the sole action of the dc current flowing through the nanopillar. For this, we can still use the MRFM technique which sensitively measures the variation of the longitudinal magnetization ΔM_z over the whole volume of the magnetic body, a quantity *directly* proportional to the normalized power $p = \Delta M_z/(2M_s)$ emitted by the STNO [163], where M_s is the saturation magnetization.

First, we measure the phase diagram of the STNO autonomous dynamics as a function of $I_{\rm dc}$ and $H_{\rm ext}$, see Fig.3.3a. Three different regions can be distinguished. At low negative or positive current (region ⓐ), ΔM_z is negligible, because in the subcritical region, the spin transfer torque is not sufficient to destabilize the magnetization from the perpendicular applied field direction. As $I_{\rm dc}$ is reaching a threshold negative value (from -3 to -7 mA as $H_{\rm ext}$ increases from 8.5 to 10.7 kOe, see pink solid line), the MRFM signal starts to smoothly increase in region ⓑ. It corresponds to the onset of spin transfer driven oscillations in the thin layer. As $I_{\rm dc}$ is further decreased towards more negative values, the angle of precession increases in the thin layer, until it eventually reaches 90°:

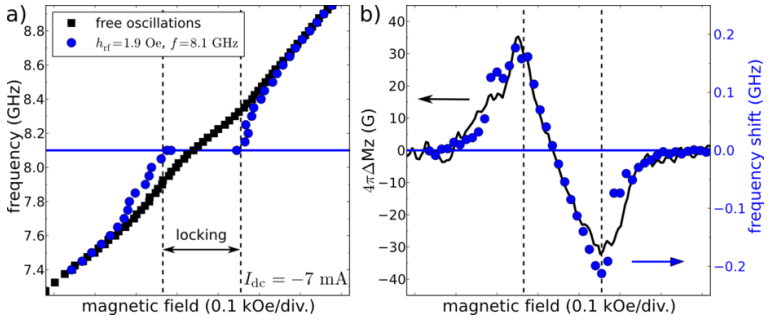

Figure 3.4: ***Phase-locking to the external microwave field.*** *(a) Magnetic field dependence of the STNO frequency in the free and forced regimes (the external source at 8.1 GHz is h_{rf}). (b) Comparison between the STNO frequency shift deduced from (a) and the MRFM signal.*

at the boundary between regions ⓑ and ⓒ (see black dashed line) $4\pi\Delta M_z$ equals the full saturation magnetization in the thin layer, $4\pi M_s = 8$ kG. It is interesting to note that owing to the GMR effect, this phase diagram can also be measured from the variation of the dc resistance of the spin-valve nanopillar, but the MRFM detection is by far more sensitive (the signal to noise ratio is one order of magnitude better).

We now turn to the quantitative analysis of the subcritical region ⓐ. We introduce $\mathcal{N} = VM_s/(g\mu_B)$, the number of spins in the thin layer (V is its volume, g the Landé factor, μ_B the Bohr magneton). The averaged normalized power p in the subcritical regime ($|I_{\rm dc}| < I_{\rm th}$) is evaluated in the stochastic nonlinear oscillator model described in section VII of ref. [163]. Under the assumption that only one spin-wave mode dominates the STNO autonomous dynamics,

$$\frac{\Delta M_z}{2M_s} = \frac{k_B T}{\mathcal{N}\hbar\omega_\nu}\,\frac{1}{1 - I_{\rm dc}/I_{\rm th}}\,, \tag{3.1}$$

where $I_{\rm th} = 2\alpha\omega_\nu\mathcal{N}e/\epsilon$ is the threshold current for auto-oscillation of the spin-wave mode ν with frequency ω_ν (α is the Gilbert damping constant in the thin layer, e the electron charge, and ϵ the spin torque efficiency). In Eq.(3.1), the prefactor $\eta \equiv k_B T/(\mathcal{N}\hbar\omega_\nu)$ is the noise power, *i.e.*, the ratio between the thermal energy $k_B T$ and the maximal energy stored in the SW mode ν. From Eq.(3.1), the inverse power is linear with the bias current $I_{\rm dc}$ in the subcritical region. A measurement at $H_{\rm ext} = 10$ kOe is shown in Fig.3.3b. From a linear fit, one can obtain the threshold current $I_{\rm th}$ and the noise power η. The dependencies of $I_{\rm th}$ and η on the perpendicular magnetic field are plotted in Figs.3.3c and d, respectively.

The parameters V, M_s, g (hence, $\mathcal{N} \simeq 6.3 \times 10^6$) and $\alpha = 0.014$ of the thin layer have been determined from the extensive MRFM spectroscopic at $I_{\rm dc} = 0$ presented in the previous section [134]. This study also yields the dispersion relations $\omega_\nu = \gamma(H_{\rm ext} - H_\nu)$ of the thin layer modes ($\gamma = g\mu_B/\hbar = 1.87\ 10^7$ rad/s/Oe, H_ν is the Kittel field associated to the mode ν). By injecting ω_ν in the expression of the threshold current, it is found that the latter depends linearly on the perpendicular bias field, $I_{\rm th} = (2\alpha\mathcal{N}e/\epsilon)\gamma(H_{\rm ext} - H_\nu)$, as observed in Fig.3.3c. The linear fit of $I_{\rm th}$ *vs.* $H_{\rm ext}$ yields $H_\nu = 6.80 \pm 0.15$ kOe and $\epsilon = 0.30 \pm 0.005$. This analysis hence provides an accurate determination of the spin torque efficiency, found to be in agreement with the accepted value in similar STNO stacks [155]. Moreover, a comparison with the spin-wave modes of the thin layer shows that the fitted value of H_ν precisely corresponds to the Kittel field of the $(\ell, n) = (0, 0)$

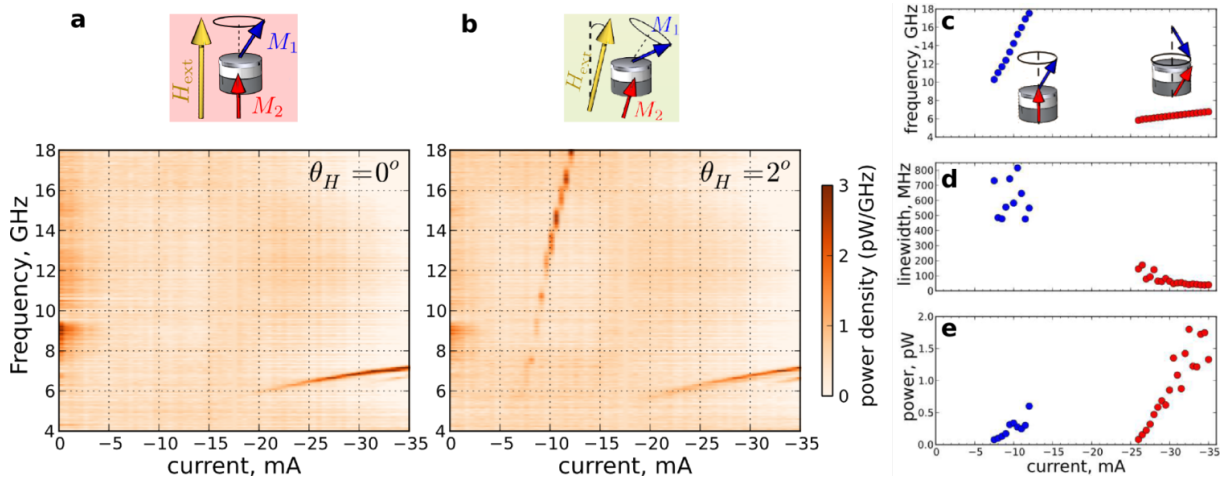

Figure 3.5: ***Spectral analysis of the auto-oscillation signal.*** *Power density map vs. bias dc current as a function of the angle of the applied magnetic field ($H = 8.2$ kOe): along the normal ($\theta_H = 0°$, panel a) and slightly misaligned ($\theta_H = 2°$, panel b). (c-e) Spectral analysis of the data shown in panel (b). The blue color is used to highlight the auto-oscillating mode of the thin layer, while the red color highlights the collective mode between thin and thick layers.*

mode. It thus allows us to conclude about the nature of the mode that first auto-oscillates at $I_{dc} < 0$ as being the fundamental, most uniform precession mode of the thin layer.

Having identified the auto-oscillating mode, we now try to phase-lock it to an external signal. For this, we use spectral analysis to detect the auto-oscillating signal in the frequency domain, and monitor it at fixed dc current ($I_{dc} = -7$ mA) as a function of the magnetic field, in the absence and presence of the external source at 8.1 GHz (see black and blue dots in Fig.3.4a, respectively). We note that here a slight tilt of the applied field ($\theta_H = 2°$) is required, because no oscillatory voltage is produced in the exact perpendicular configuration, due to the perfect axial symmetry of the STNO trajectory (compare Figs.3.5a and b). We find that only the rf field h_{rf} has the appropriate symmetry to couple to the auto-oscillating mode. We add that in our axially symmetrical case, no phase-locking behavior is observed with the even synchronization index $r = 2$ [186], neither with i_{rf}, nor with h_{rf}, which is due to the circular STNO precession trajectory. Interestingly, we can compare the MRFM signal recorded in the presence of the phase-locking signal h_{rf} to the frequency shift of the forced oscillations with respect to the free running oscillations, as shown in Fig.3.4b. This demonstrates that in the phase-locking range, the STNO amplitude changes ($\Delta M_z > 0$: increases, $\Delta M_z < 0$: decreases), so as to maintain its frequency equal to the frequency of the source, here fixed at 8.1 GHz. This comparison also allows to estimate the phase-locking bandwidth, found to be as large as 0.4 GHz despite the small amplitude of the external signal ($h_{rf} = 1.9$ Oe). The nonlinear frequency shift is indeed the largest in the perpendicular configuration, $N = 4\gamma M_s \simeq 48$ GHz [163], therefore, a small change of the power emitted by the STNO is sufficient to change its frequency by a substantial amount.

As mentioned in the introduction of this chapter, this large nonlinear frequency shift does not only have advantages, as large frequency tunability and efficiency to adapt to external signals, but also drawbacks, in particular, it yields a severe linewidth broadening [101]. This is due to the nonlinear phase-amplitude coupling ν, defined as the dimensionless ratio of the nonlinear frequency shift to amplitude fluctuations rate [163], which

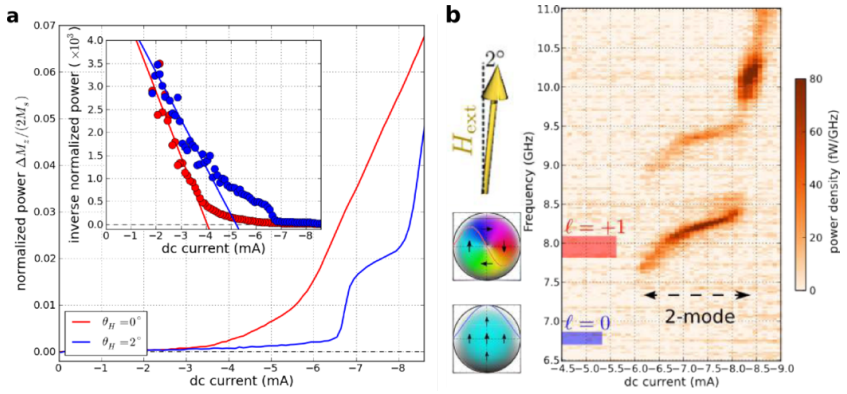

Figure 3.6: ***Bi-modal auto-oscillation in the autonomous regime.*** *(a) Total power p emitted by the STNO as a function of the bias dc current, measured by MRFM at $H = 9.14$ kOe and $\theta_H = 0°$ (red) or $\theta_H = 2°$ (blue). The inset shows the dependence of the inverse power, together with the linear fit that defines the threshold current, as in Fig.3.3b. (b) Power density map vs. bias dc current obtained at $H = 9.14$ kOe and $\theta_H = 2°$. The blue and red ticks show the position of the lowest spin-wave modes with $\ell = 0$ and $\ell = 1$ symmetries, determined by MRFM spin-wave spectroscopy.*

converts amplitude noise into frequency noise. Whereas in standard auto-oscillators, it is much less than one, it can reach large values in STNOs, therefore the emission linewidth $\Delta f = \Delta f_0(1 + \nu^2)$ can be increased by up to four orders of magnitude compared to the value Δf_0 expected in the linear case. The latter is proportional to the thermal noise and to the natural damping rate and inversely proportional to the energy stored in the oscillator [163], hence to its volume, which is very tiny due to the nanometric size of spin torque oscillators.

This is illustrated in the spectral analysis presented in Figs.3.5c-e, where the auto-oscillation of the thin layer mode (blue dots) is characterized by a very large tunability (up to 1.8 GHz/mA, see Fig.3.5c), but also by a very broad generation linewidth (> 500 MHz, see Fig.3.5d). Interestingly, as the dc current is kept increasing, the dynamical magnetization of the thin layer eventually reverses against the field, which changes qualitatively the characteristics of the auto-oscillation mode (red dots). A large downward jump in frequency is observed beyond −20 mA (the frequency drops by at least 20 GHz), accompanied by a much narrower emission peak (linewidth ≈ 50 MHz), and a much smaller frequency tunability (0.12 GHz/mA). This is associated to the dynamics being now a coupled between thin and thick layers, as confirmed by simulations, the spin transfer torque at such large bias currents being sufficient to destabilize a larger volume. We would like to emphasize that these spectral signatures are very similar to the ones reported on the generation of magnetic droplet solitons by spin transfer forque [129].

3.1.3 Bi-modal generation

In this section, I would like to briefly report on interesting experimental observations that we made in the case of slightly broken axial symmetry, with the applied field tilted by 2° from the normal.

If we focus on the behavior observed just above the threshold current in Fig.3.5b, we actually observe not only one, but two auto-oscillating signals in a quite broad range of

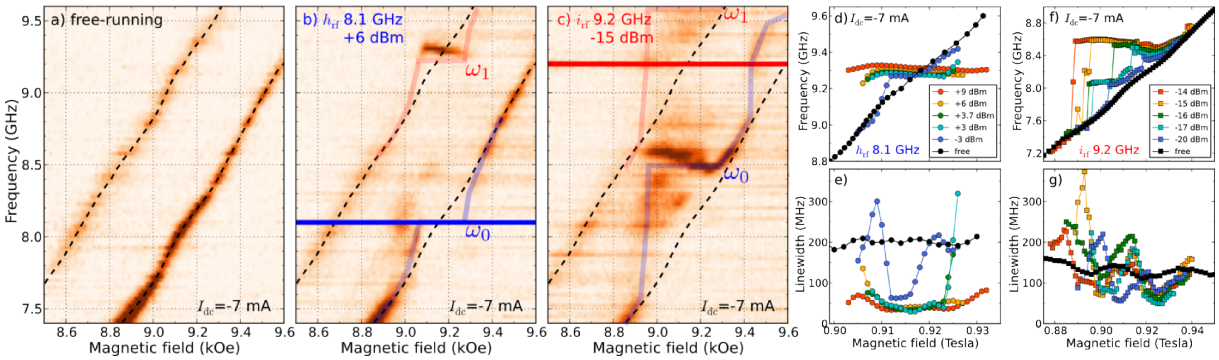

Figure 3.7: ***Bi-modal auto-oscillation in the forced regime.*** *(a) Free-running auto-oscillations at $I_{dc} = -7$ mA vs. magnetic field applied at $\theta_H = 2°$. (b) Behavior in the presence of the uniform rf field generated by the external antenna at $f = 8.1$ GHz ($h_{rf} = 2.5$ Oe, thick blue line) and (c) of the rf current flowing through the nano-pillar at $f = 9.2$ GHz ($i_{rf} = 350$ μA, thick red line). The dashed lines recall the location of the free-running oscillations. The light blue line is a guide for the eye, while the light red one is the same guide translated up in frequency by 1.1 GHz. (d) Frequency and (e) linewidth of the mode $\ell = +1$ as a function of the amplitude of h_{rf} used to lock the mode $\ell = 0$ at 8.1 GHz (see panel b). (f) Frequency and (g) linewidth of the mode $\ell = 0$ as a function of the amplitude of i_{rf} used to lock the mode $\ell = +1$ at 9.2 GHz (see panel c).*

current around -7 mA, separated by approximately 1.1 GHz, as shown in Fig.3.6b. We also observe a striking difference in the behavior of the normalized power measured by MRFM between the high symmetry case ($\theta_H = 0°$), which was studied in Fig.3.3, and the broken symmetry case ($\theta_H = 2°$), where a step-like behavior of the power increase is observed (Fig.3.6a). It turns out that the spectroscopic study presented above allows us to identify these two auto-oscillating modes as being the most uniform $\ell = 0$ and $\ell = 1$ azimuthal modes, see Fig.3.6b. The origin of this bi-modal excitation regime at low current is not completely clear, but it certainly arises from mode competition: due to the broken axial symmetry, $\ell = 0$ and $\ell = 1$ modes actually slightly hybridize with each other [104, 134], and can be simultaneously pumped by the dc spin transfer torque.

The behavior of this bi-modal regime in the presence of an external source is even more interesting, and is presented in Fig.3.7. In this figure, the dc current is now fixed to -7 mA, and the power spectrum density (PSD) maps are recorded as a function of the magnetic field. In the free regime (Fig.3.7a), the bi-modal emission is evidenced by the presence of two emission peaks evolving in parallel on the whole field range investigated. The striking result is that the external signal does not affect only the auto-oscillating mode which has its free-running frequency close to the external frequency and the appropriate spatial symmetry [82], but also the other auto-oscillating mode, in a quite similar way. It is particularly clear on Fig.3.7b, where the external rf field synchronizes the $\ell = 0$ mode between 9 kOe and 9.3 kOe at 8.1 GHz (see blue line): at the same time, the frequency of the $\ell = 1$ mode becomes almost constant at slightly more than 9.2 GHz (see light red line). Note that in contrast, $h_{\rm rf}$ does not affect directly the $\ell = 1$ mode at 8.1 GHz around $H = 8.7$ kOe, because it has the wrong spatial symmetry, as already noted above. The influence of the rf current at $f = 9.2$ GHz on the PSD of Fig.3.7c looks quite more complicated, but clearly, the behavior of mode $\ell = 0$, whose free-running frequency is about 1 GHz below the external source, is also strongly affected on a broad range of

magnetic field.

These features can be ascribed to some nonlinear interaction between coexisting auto-oscillating modes [90]. One consequence of it can be seen in Fig.3.7e, which plots the evolution of the linewidth of the $\ell = 1$ mode (at around 9.2 GHz) while the $\ell = 0$ mode is phase-locked by the microwave field applied at 8.1 GHz and different powers. A strong reduction of the $\ell = 1$ mode linewidth, which drops from almost 200 MHz down to less 50 MHz, is observed. A natural explanation would be some kind of *mode cooling* mechanism: by phase-locking the mode $\ell = 0$ with the external source, its frequency, hence its amplitude, gets stabilized. As a result, its influence on the linewidth of mode $\ell = 1$ through nonlinear cross-terms is suppressed and the latter exhibits its intrinsic linewidth, with the contribution of only self nonlinear interactions.

Related publications

1. V. V. Naletov, G. de Loubens, G. Albuquerque, S. Borlenghi, V. Cros, G. Faini, J. Grollier, H. Hurdequint, N. Locatelli, B. Pigeau, A. N. Slavin, V. S. Tiberkevich, C. Ulysse, T. Valet, and O. Klein, *Identification and selection rules of the spin-wave eigenmodes in a normally magnetized nanopillar*, Phys. Rev. B **84**, 224423 (2011).

2. A. Hamadeh, G. de Loubens, V. V. Naletov, J. Grollier, C. Ulysse, V. Cros, O. Klein, *Autonomous and forced dynamics in a spin-transfer nano-oscillator: Quantitative magnetic-resonance force microscopy*, Phys. Rev. B **85**, 140408(R) (2012).

3. V. V. Naletov, G. de Loubens, S. Borlenghi, O. Klein, *Spin-wave eigenmodes in a normally magnetized nano-pillar* in *Magnonics: from Fundamentals to Applications*, S. O. Demokritov, A. N. Slavin Eds. Topics in Applied Physics **125**, pp. 3–15 (Springer, 2013).

3.2 Spin-valve nanopillar in the vortex state

Spin torque oscillators can be operated in various geometries and magnetic configurations. Of special engineering interests are spin torque vortex oscillators (STVOs) [148, 128]. In fact, a large oscillation amplitude of the free layer is naturally occurring in the vortex configuration. In that case, the excited mode corresponds to the gyrotropic motion of the vortex core around its equilibrium position, which is accompanied by a full in-plane rotation of the magnetization in the region enclosed by the orbit of gyration. This can provide output power in the μW range in magnetic tunnel junctions [184]. Vortex-based oscillators also do not require an external magnetic field to be operated, which is an advantage for applications [48]. Moreover, vortex oscillators are a model system for coupled oscillators in general, because their dynamics is well understood [49], which we will take advantage of in the next section 3.3.

The exact same spin-valve nanopillar devices as those studied in the saturated state in the previous section 3.1 can also be operated in the double vortex state, where one vortex is stabilized in each of the magnetic layers. Thanks to the dc current flowing through the sample and to the applied perpendicular field, the chirality and the polarity of both vortices can be controlled. When the chiralities are parallel, an auto-oscillation signal can be detected only in the state of opposite polarities [120]. The high spectral purity of this microwave emission associated to the gyroptropic mode dominated by the thick Py layer is remarkable (linewidth below 100 kHz, emission frequency in the 600–900 MHz

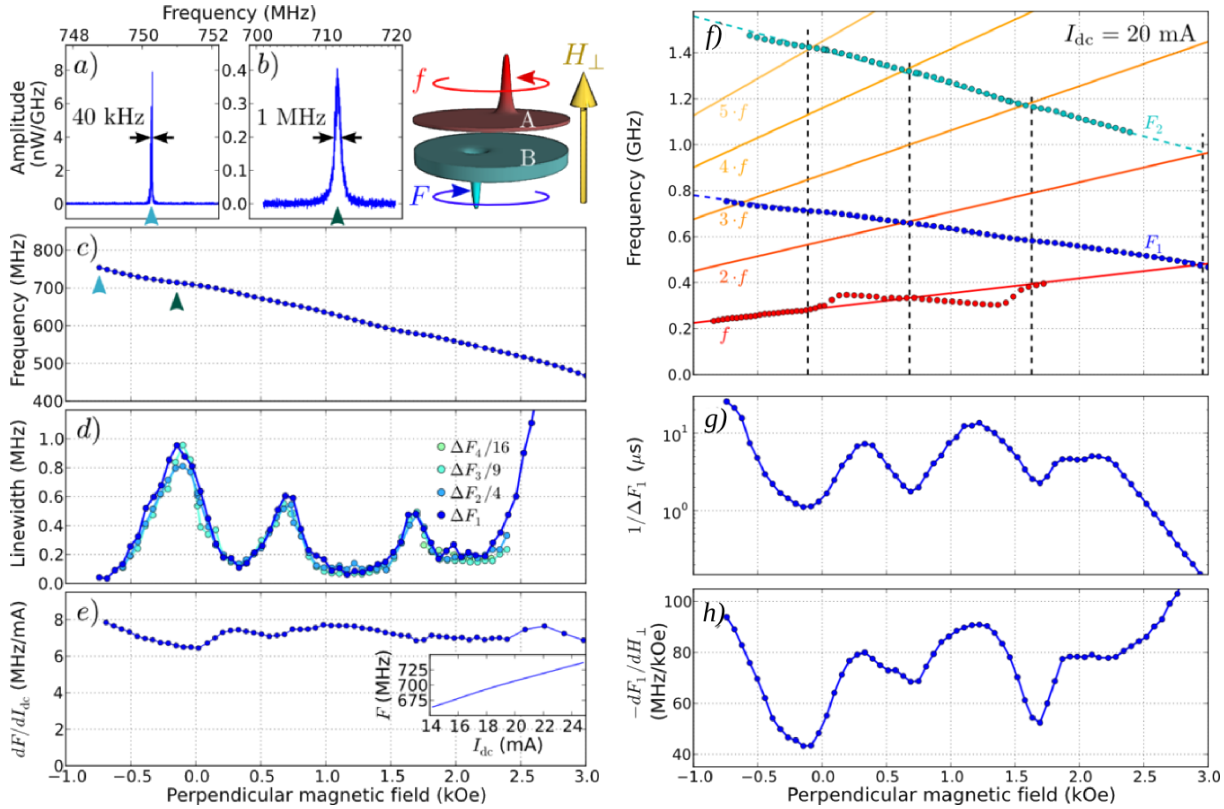

Figure 3.8: ***Origin of spectral purity and tuning sensitivity in a spin torque vortex oscillator.*** *Sketch: STNO based on coupled vortices. (a) Power density spectra measured at $I_{dc} = 20$ mA and a perpendicular magnetic field $H_z = -0.7$ kOe and (b) $H_z = -0.15$ kOe. (c) Dependence of the fundamental oscillation frequency on H_z. (d) Generation linewidths of harmonics $n = 1$ to 4 divided by n^2 as a function of H_z. (e) Frequency tunability vs. H_z. Inset: dependence of the oscillation frequency on I_{dc} measured at $H_z = 0$ kOe. (f) Blue dots: fundamental frequency F_1 and harmonics F_2 of the auto-oscillating mode dominated by the thick layer (vortex core polarity $p_B = -1$) as a function of H_z. Red dots: frequency f of the overdamped mode dominated by the thin layer (polarity $p_A = +1$). Red tone straight lines are guides to the eye and show successive harmonics of f. (g) Evolution of the inverse generation linewidth. (h) Slope of the oscillation frequency F_1 vs. H_z.*

range); it is ten times better than the one observed when only one vortex is present in the nanopillar [119].

In the following, we investigate the collective dynamics of these two coupled vortices driven by spin transfer, to provide insights on its very high coherency, and study its behavior when phase-locked to an external source.

3.2.1 Auto-oscillations in the double vortex state

The microwave characteristics of the double vortex based STVO with opposite polarities are presented in Figs.3.8a-e as a function of the perpendicular bias field H_z. In panel (c), the oscillation frequency linearly decreases with increasing H_z, as expected for a gyrotropic mode dominated by the thick layer vortex, whose polarity is anti-parallel to the applied field (see Eq.(2.1)). The dependence of the generation linewidth ΔF_1 on H_z in panel (d) (dark blue dots) displays minima down to 40 kHz ($F_1/\Delta F_1 \simeq 19000$) and

maxima up to 1 MHz ($F_1/\Delta F_1 \simeq 700$), *i.e.*, a decrease of spectral purity by more than a factor 25 by changing H_z from -0.7 kOe [Fig.3.8a] to -0.15 kOe [Fig.3.8b]. We note that these strong variations of the linewidth observed at $I_{\rm dc} = 20$ mA cannot be attributed to changes of the nearly constant supercriticality ($I_{\rm dc}/I_{\rm th} \simeq 2$). The generation linewidth of a nonlinear auto-oscillator can be written as [101]:

$$\Delta F_{\rm g} = \frac{k_B T}{E_s}\frac{\Gamma_+}{2\pi}(1+\nu^2)\,, \tag{3.2}$$

where E_s is the energy stored in the auto-oscillation, Γ_+ the natural energy dissipation rate, and ν the nonlinear phase-amplitude coupling parameter. The latter is defined as $\nu = Np/\Gamma_p$, the dimensionless ratio between the nonlinear frequency shift N multiplied by the normalized oscillation power p and divided by the damping rate of amplitude fluctuations Γ_p [163]. Since the spectral linewidth $\Delta F_{\rm g}$ depends quadratically on ν, the dependence of this parameter on H_z should be evaluated. For this, we analyze the linewidths of the harmonics of the auto-oscillation signal [151]. We have plotted in Fig.3.8d the evolution of $\Delta F_n/n^2$ ($n = 2$ to 4) together with the one of ΔF_1. Independently of H_z, we observe that $\Delta F_n \simeq n^2 \Delta F_1$. This means that our STVO is quasi-isochronous [151]: $\nu \simeq 0$ in the full field range. Therefore, one can also exclude that the strong variations of linewidth observed are due to some changes of ν with H_z. Actually the expected linear linewidth of our oscillator ($\nu = 0$ in Eq.(3.2)) yields $\Delta F_g = 29$ kHz, a value close to the narrow linewidth of 40 kHz observed at $H_{\rm ext} = -0.7$ kOe.

To elucidate the observed linewidth broadenings, it should be noticed that in addition to the gyrotropic mode dominated by the thick $\rm Py_B$ layer excited by spin torque, there is a gyrotropic mode dominated by the thin $\rm Py_A$ layer, which for $I_{\rm dc} > 0$ is overdamped by spin torque. This mode can be probed by FMR using the microwave field $h_{\rm rf}$ produced by the microwave antenna deposited on top of the sample, and its frequency is reported in Fig.3.8f using red dots. As expected, the gyrotropic mode frequency f dominated by $\rm Py_A$ is lower and has an opposite slope *vs.* H_z than the one F_1 dominated by $\rm Py_B$, due to smaller thickness and opposite core polarity ($p_{\rm A} = +1 = -p_{\rm B}$) [39]. At magnetic fields where the frequencies of the auto-oscillating and overdamped modes are commensurable, $pF_1 = qf$, with $p, q \in \mathbb{N}$ (see dashed vertical lines), a decrease of $-dF_1/dH_\perp$ (Fig.3.8h) concomitant with a decrease of the inverse linewidth (Fig.3.8g) is observed. We attribute this behavior to the interaction between the eigenmodes of the STVO: energy can be transferred from oscillating to overdamped modes, which broadens the generation linewidth at the crossings between harmonics of these modes. This also affects the behavior of the overdamped mode, as explained in details in ref. [110].

The high spectral purity of this double vortex STVO is thus explained by its weak nonlinearities. Interestingly, it should be noted that the latter depend quite substantially on the relative orientation of the vortex polarities [112]. Moreover, despite these weak nonlinearities, the frequency tunability of this STVO is not negligible (8 MHz/mA, see Fig.3.8e) regarding its narrow linewidth, thanks the Oersted field contribution to the confinement potential [49].

3.2.2 Perfect synchronization to an external source

We now turn to the study of the synchronization of this STVO to an external source. Figs.3.9a and b show that it is very efficient when the latter is the external rf field $h_{\rm rf}$,

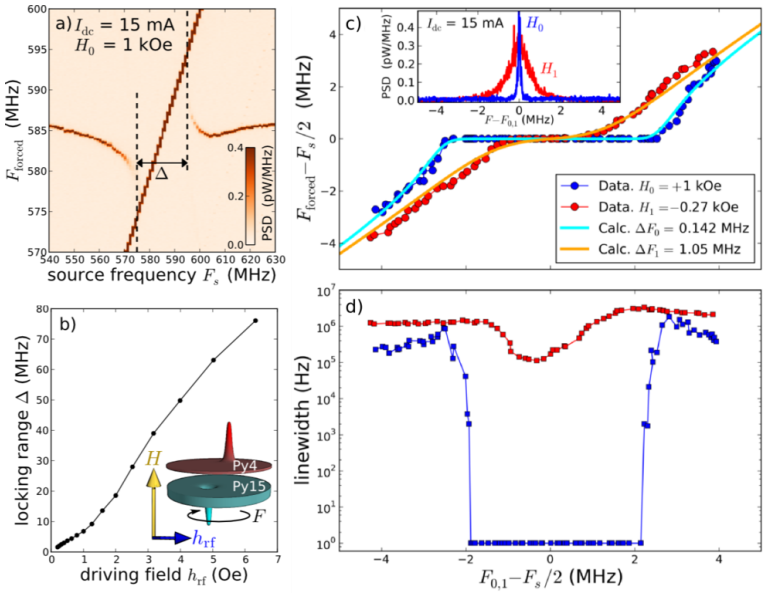

Figure 3.9: ***Perfect phase-locking of the STVO to the microwave field.*** *(a) Power spectrum map at $I_{dc} = 15$ mA and $H_0 = 1$ kOe vs. the frequency F_s of the external microwave field $h_{rf} = 2$ Oe. (b) Locking range Δ vs. drive amplitude. (c) Variation of the frequency mismatch $F_{forced} - F_s/2$ vs. detuning $F_{0,1} - F_s/2$ at $H_0 = +1$ kOe (blue dots) and $H_1 = -0.27$ kOe (red dots) for $h_{rf} = 6.3$ Oe. Continuous lines are fits using Eq.(5) of ref. [57] yielding a coupling strength $\varepsilon = 2.5$ MHz. Inset: emission spectra at H_0 and H_1 in the free running regime. (d) Dependence of the emission linewidth on the frequency detuning at H_0 and H_1.*

which indeed has the appropriate symmetry to couple to the gyrotropic mode. We point out that at $h_{\rm rf} = 6.3$ Oe, the locking range $\Delta = 75$ MHz corresponds to 13% of the oscillator frequency F_0. In order measure the linewidth of the oscillator signal when its frequency is locked, we realize phase-locking at $2F_0$ because in that case the oscillation signal is not hindered by the source signal [150, 50].

To investigate the influence of fluctuations [59] on the actual characteristics of our vortex oscillator when it is phase-locked, we compare the synchronization of auto-oscillation signals having different generation linewidths. We use two different applied fields, $H_0 = +1$ kOe and $H_1 = -0.27$ kOe, at which the emission frequencies at $I_{\rm dc} = 15$ mA slightly differ ($F_0 = 586$ MHz and $F_1 = 684$ MHz, respectively), and the generation linewidth varies by more than a factor seven, from $\Delta F_0 = 142$ kHz to $\Delta F_1 = 1.05$ MHz (see inset of Fig.3.9a and explanation in previous section [83]). Using blue and red dots at H_0 and H_1, respectively, we plot the experimental frequency mismatch $F_{\rm forced} - F_s/2$ (Fig.3.9a) and the linewidth in the forced regime (Fig.3.9b) as a function of the detuning $F_{0,1} - F_s/2$ between the natural oscillator frequency and half the source frequency. The strong differences observed in the characteristics of the synchronization at these two fields reveal the role played by the fluctuations in the phase dynamics of STNOs. When the latter are weak (narrower generation linewidth at H_0), the locking range is large (more than 4 MHz) and the synchronized signal acquires the spectral quality of the source (less than 1 Hz). When the noise is larger (broader generation linewidth at H_1), it competes against the coupling to the external source, which results in a smaller apparent locking range and a poorest spectral quality of the forced oscillation. Here, increasing the linewidth by a factor $\Delta F_1/\Delta F_0 \simeq 7$ has a huge influence on the signal coherency in the phase-locked

regime since its improvement with respect to the free running case drops from a factor 10^5 to only 10.

In conclustion, the phase-locking to the external microwave field of this double vortex STVO can be very robust. This has also been confirmed by direct measurement of the oscillator phase deviation, where perfect phase-locking was observed [111].

Related publications

1. N. Locatelli, V. V. Naletov, J. Grollier, G. de Loubens, V. Cros, C. Deranlot, C. Ulysse, G. Faini, O. Klein, A. Fert, *Dynamics of two coupled vortices in a spin valve nanopillar excited by spin transfer torque*, Appl. Phys. Lett. **98**, 062501 (2011).

2. A. Hamadeh, N. Locatelli, V. V. Naletov, R. Lebrun, G. de Loubens, J. Grollier, O. Klein, V. Cros, *Perfect and robust phase-locking of a spin transfer vortex nano-oscillator to an external microwave source*, Appl. Phys. Lett. **104**, 022408 (2014).

3. A. Hamadeh, N. Locatelli, V. V. Naletov, R. Lebrun, G. de Loubens, J. Grollier, O. Klein, V. Cros, *Origin of spectral purity and tuning sensitivity in a vortex-based spin transfer nano-oscillator*, Phys. Rev. Lett. 112, 257201 (2014).

4. A. S. Jenkins, E. Grimaldi, P. Bortolotti, R. Lebrun, H. Kubota, K. Yakushiji, A. Fukushima, G. de Loubens, O. Klein, S. Yuasa, V. Cros, *Controlling the chirality and polarity of vortices in magnetic tunnel junctions*, Appl. Phys. Lett. 105, 172403 (2014).

5. N. Locatelli, R. Lebrun, V. Naletov, A. Hamadeh, G. de Loubens, O. Klein, J. Grollier, V. Cros, *Improved spectral stability in spin transfer nano-oscillators: single vortex versus coupled vortices dynamics*, IEEE Trans. Magn. **51**, 4300206 (2015).

6. A. S. Jenkins, R. Lebrun, E. Grimaldi, S. Tsunegi, P. Bortolotti, H. Kubota, K. Yakushiji, A. Fukushima, G. de Loubens, O. Klein, S. Yuasa, V. Cros, *Spin-torque resonant expulsion of the vortex core for an efficient radiofrequency detection scheme*, Nature Nanotech. **11**, 360–364 (2016).

7. R. Lebrun, J. Grollier, F. Abreu Araujo, P. Bortolotti, V. Cros, A. Hamadeh, X. de Milly, Y. Li, G. de Loubens, O. Klein, S. Tsunegi, H. Kubota, K. Yakushiji, A. Fukushima, S. Yuasa. *Driven energy transfer between coupled modes in spin-torque oscillators*, Phys. Rev. B **95**, 134444 (2017).

3.3 Control of synchronization in nonlinear auto-oscillators

Owing to their intrinsically large nonlinearities, sub-micron dimensions, simple signal extractions from magnetoresistance, and ease of being coupled, spin torque oscillators are particularly suitable to study synchronization phenomena [147]. They offer an ideal playground to design novel functionalities [117] and have been recently proposed for oscillator-based neuromorphic computing [136]. They have an exceptional ability to phase-lock to external signals, as demonstrated using either a microwave current passing through the device [152, 57, 150, 50] or a microwave field produced by a nearby antenna [186, 82, 84]. Moreover, it was realized quite early that mutual nonlinear synchronization [164] of several of these nanodevices could be achieved to increase their output power and reduce their phase noise [60]. In parallel, experimental evidences of mutual synchronization of a

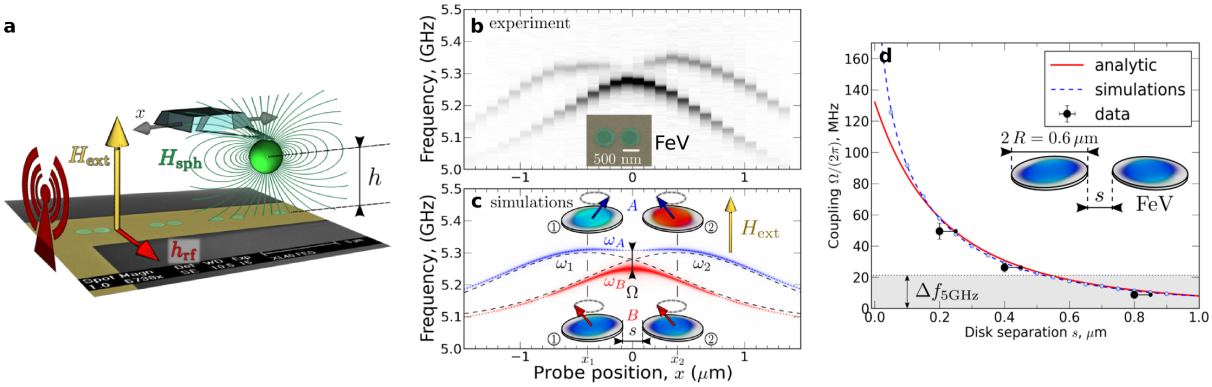

Figure 3.10: ***MRFM spectroscopy of the dynamical dipolar coupling in adjacent nano-disks.*** *(a) Schematics of the setup: the MRFM probe is scanned laterally above different pairs of 27 nm thick FeV disks excited by a microwave field. (b) Density plot of the experimental MRFM spectra at fixed perpendicular field $H = 17.2$ kOe as a function of the displacement x of the nanosphere above a pair of 600 nm FeV disks separated by $s = 200$ nm (SEM picture in inset). (c) Predicted behavior by micromagnetic simulations. The upper mode (blue) corresponds to the anti-binding mode (A), while the lower (red) shows the binding mode (B). Insets: simulated precession profiles in each disk for modes (A) and (B) at the anti-crossing. The dashed lines show the individual modes of the disks in the absence of dynamical coupling. (d) Coupling strength vs. separation s between two disks. The plot compares the experimental findings to the predicted amplitude of the magnetodipolar interaction (continuous line: analytical calculation, dashed line: micromagnetic simulations).*

few spin torque oscillators mediated by spin-waves [95, 122], exchange [154], and electrical couplings [113] have been obtained.

The results presented in the previous section 3.2 on double vortex STVOs are very promising for the idea of mutually coupling such oscillators through the dipolar interaction [9]. The idea is to replace the external microwave field by the dipolar stray field of an adjacent STVO.

3.3.1 Dipolar coupling between adjacent nanomagnets

As we would like to use the magneto-dipolar interaction between adjacent STNOs to mediate their synchronization, it would first be nice to have an experimental access to this coupling, that will be called throughout this section Ω (expressed in units of rad/s). In Fig.3.10, we demonstrate a smart way of using our MRFM technique to spectroscopically determine Ω in the case of two adjacent FeV nano-disks, uniformly saturated along their normal. We emphasize that we perform this experiment in the passive regime, *i.e.*, the magnetization dynamics is excited by standard FMR (the devices are not self-oscillating). For this, we take advantage of the stray field gradient produced by the magnetic tip of our MRFM (panel a) to continuously tune and detune the relative resonance frequencies between two adjacent nano-objects, as shown in panel b. This reveals the anti-crossing and hybridization of the spin-wave modes in the pair of disks, which form collective binding and anti-binding modes (panel c). At the exact tuning ($\omega_1 = \omega_2$), the measured frequency splitting between the binding and anti-binding modes precisely corresponds to

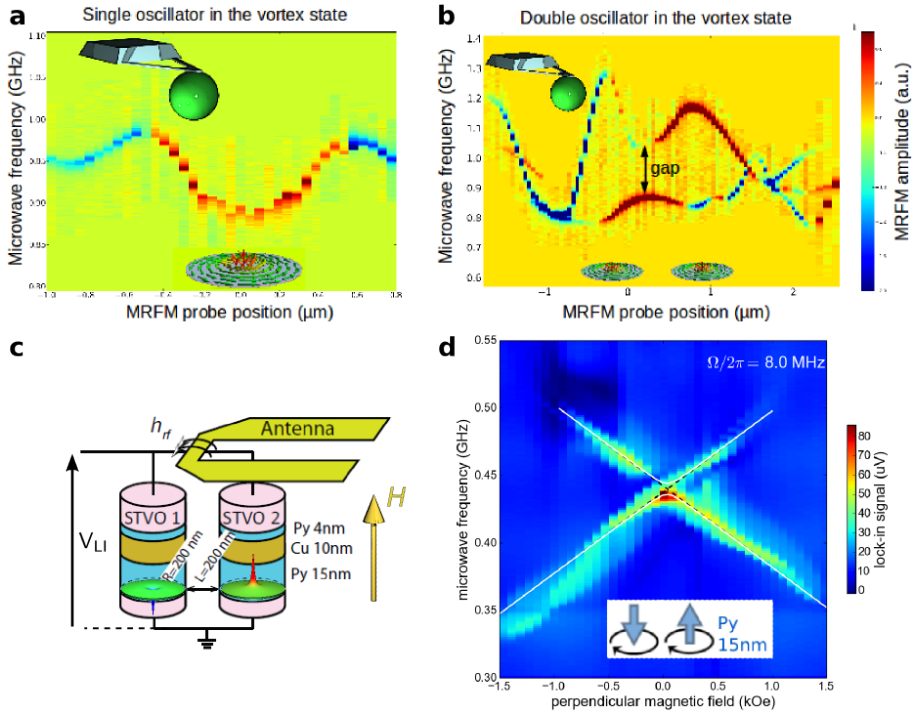

Figure 3.11: ***Spectroscopy of the dynamical dipolar coupling in a pair of vortex oscillators.*** *(a) Evolution of the gyrotropic mode frequency in a* single *FeV nano-disk in the vortex state as a function of the displacement of the MRFM probe above it (same data as in Fig.2.10d). (b) Similar MRFM experiment for a* pair *of vortex-state FeV nano-disks (same sample as in Fig.3.10b). (c) Pair of spin torque oscillators (400 nm in diameter, separated by 200 nm), each of them containing a vortex, with a microwave antenna patterned above it. The latter is used to excite the gyrotropic dynamics, which is detected electrically by measuring the voltage drop across the two nanopillars. (d) It allows to reveal the hybridization of the dynamics at the anti-crossing by sweeping the perpendicular bias field. The two vortex cores have opposite polarities.*

the strength of the dynamical dipolar coupling Ω:

$$\omega_{A,B} = \frac{\omega_1 + \omega_2}{2} \pm \sqrt{\left(\frac{\omega_1 - \omega_2}{2}\right)^2 + \left(\frac{\Omega}{2}\right)^2}, \tag{3.3}$$

where A and B label the anti-binding and binding modes, respectively, and 1 and 2 the individual oscillators. This accurate MRFM determination of Ω is measured as a function of the separation between the nano-disks (panel d), and agrees quantitatively with calculations of the expected dynamical magneto-dipolar interaction in our sample [146].

A similar characterization can in principle be performed in any sample, providing that the frequency splitting induced by the coupling is larger than the FMR linewidth. For instance, we repeated the same study on a system of four nano-disks, or in pairs of "touching" YIG nano-disks, where we determined $\Omega/\gamma = 20$ Oe, to be compared with a field linewidth of 4 Oe at 10 GHz. However, the situation is quite more complex if the samples are in a non-uniform state, such as a vortex, since the strayfield of the MRFM probe will disturb their static equilibrium configuration. This is what is shown in Figs.3.11a and b, for a single vortex nano-disk and a pair of vortex nano-disks, respectively. As shown

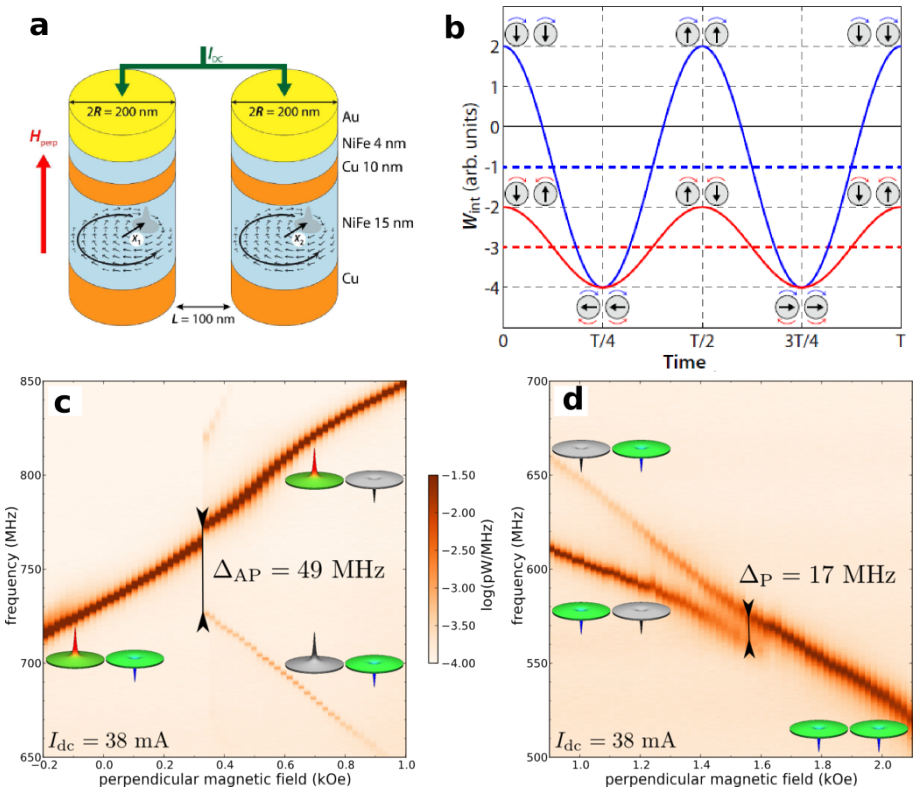

Figure 3.12: ***Dependence of the mutual synchronization bandwidth on the relative vortex core polarities.*** *(a) Pair of spin valve nanopillars with $2R = 200$ nm diameter separated by a distance $L = 100$ nm. Each pillar contains a Py(4 nm)/Cu(10 nm)/Py(15 nm) spin-valve and a vortex is present in each 15 nm Py layers. The current is injected in parallel into the two pillars. (b) Evolution of the dipolar energy between two vortices modeled as macrodipoles oscillating at the same frequency. The blue curve describes the P state, when vortices have identical polarities, and the red curve the AP state, when they have opposite polarities. The corresponding average values of the coupling energy are plotted as dashed lines. (c,d) Power spectrum maps versus perpendicular field, in the AP state (c) and in the P state (d). The injected current is 38 mA.*

in section 2.3, the single nano-disk experiment of Fig.3.11a allows to extract the anharmonicity of the confinement potential of the vortex core. However, the situation becomes inextricable in Fig.3.11b, where obviously the presence of two oscillators is detected, but where it is not possible to extract any coupling amplitude. Fortunately, it is also possible to rely on an electrical detection scheme of the vortex resonance to probe the collective dynamics [169]. Fig.3.11c shows a schematics of two vortex nanopillars, connected in parallel, with a common microwave antenna patterned on top to supply the excitation field. The vortex polarities of the adjacent oscillators are prepared to be opposite, so that the associated gyrotropic frequencies have opposite slope with respect to the applied perpendicular field, as can be seen in Fig.3.11d. In these data, an anti-crossing can be observed, and the value of the dipolar coupling, $\Omega/2\pi = 8$ MHz, fitted using Eq.(3.3).

3.3.2 Mutual synchronization of a pair of spin torque oscillators

Now that we have evidenced the existence of a dynamical dipolar coupling between adjacent vortices in the passive regime, the goal is to demonstrate mutual synchronization. For this, we do not supply anymore a microwave excitation signal to the system, but instead inject a dc current in parallel into the two adjacent STVOs, as sketched in Fig.3.12a. As in Fig.3.8, the current sign is such as to compensate the damping in the thick layer (and to overdamp the thin layer). Hence, owing to their much smaller volumes and limited dynamics, the contribution of the thin-layer vortices to the oscillator-oscillator coupling is weak. Moreover, their vortex core polarity is not purposely controlled in this study. In the following of this chapter, we will thus refer exclusively to the vortices in the thick Py layers of each oscillator, labeled 1 and 2.

The main experimental results of this study are shown in Figs.3.12c and d, which compare situations where the polarities of the thick Py layers vortices are anti-parallel (AP) and parallel (P), respectively. In the two cases, one observes that when the auto-oscillation peaks associated to each oscillator get closer (by sweeping the bias perpendicular field), there is a critical frequency mismatch below which only one auto-oscillation peak subsists. The observation of such a transition from two peaks associated to each auto-oscillator to a single peak is the evidence of the synchronization of the two STVOs. To discard the possibility that this transition might be related to a magnetic switching (*e.g.*, reversal of a vortex polarity), we have verified that this phenomenon is reversible by sweeping the field back and forth around the critical field value. Moreover, on some other measurements [118], frequency pulling can also be observed, which is characteristic of a transition towards synchronized oscillations [147]. On the measurement shown in Fig.3.12c, the appearance of a secondary peak around 800 MHz before synchronization is also characteristic of the interaction of the two oscillators, corresponding to the frequency beating phenomenon [147].

However, there is a quantitative difference in the frequency mismatch measured in Figs.3.12c and d, which is found to be about three times larger for the anti-parallel polarities. To understand this point, it is important to recognize that the mutual dipolar coupling between adjacent vortex oscillators depends on their relative polarities. This originates from the fact that the sense of gyration of a vortex core is dictated by its polarity, and from the form of the dipole-dipole interaction, which is anisotropic:

$$W_{int} = \frac{\boldsymbol{M}_1 \cdot \boldsymbol{M}_2 - 3(\boldsymbol{M}_1 \cdot \boldsymbol{e}_{12})(\boldsymbol{M}_2 \cdot \boldsymbol{e}_{12})}{d^3} \tag{3.4}$$

(d is the distance separating the dipoles $\boldsymbol{M}_1$ and $\boldsymbol{M}_2$, and $\boldsymbol{e}_{12}$ the unit vector joining them). Using a simple macrodipole picture for the magneto-dipolar interaction between adjacent vortices [1], one can plot the time evolution of the interaction energy, which is shown in Fig.3.12b. It can be noticed that the interaction energy between AP vortices is always negative, whereas it changes sign for P vortices, and that its time average is three times larger in the former case than in the latter case. The factor three is approximate, as a multipole expansion is required to correctly treat the mangeto-dipolar interaction between adjacent vortices [171]. Still, $\Omega_{AP} \approx 3\Omega_P$, and since the mutual synchronization bandwidth are proportional to the coupling amplitude enhanced by the dimensionless nonlinear coefficient ν, $\Delta_{AP/P} \simeq \nu\Omega_{AP/P}$ [163], the observation that the critical frequency mismatch depends on the relative vortex polarities is explained providing that the ν coefficients are similar in the two cases.

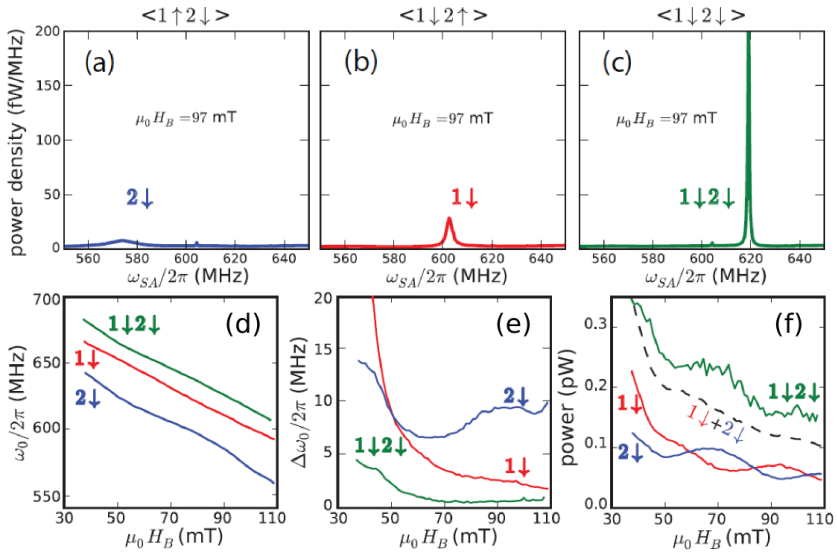

Figure 3.13: ***Improvement of microwave characteristics through mutual synchronization.*** *The sample is a pair of STVO with $2R = 200$ nm diameter separated by a distance $L = 50$ nm. Power spectral density of auto-oscillations in (a) $< 1 \uparrow 2 \downarrow >$ (b) $< 1 \downarrow 2 \uparrow >$ and (c) $< 1 \downarrow 2 \downarrow >$ polarity states at a bias current of 41 mA and a perpendicular field of 97 mT. (d-f) Field dependence of frequency (d), linewidth (e) and integrated power (f). In (f) the black dashed curve shows the power sum of red and blue curves.*

In Fig.3.13 we show additional evidence of efficient mutual synchronization through mutual dipolar coupling. In that case, the separation between the STVOs is twice less than in the previous studies, which increases the dipolar coupling Ω. Panels (a), (b) and (c) show respectively the outputs of the spectrum analyzer when the STVOs are biased with a perpendicular field of 97 mT, in states $< 1 \uparrow 2 \downarrow >$, $< 1 \downarrow 2 \uparrow >$ and $< 1 \downarrow 2 \downarrow >$, respectively. In the two first cases, only one relatively weak and broad auto-oscillation peak is observed, which represents the individual output of each STNO in the $<\downarrow>$ state, because its emission frequency is well separated (> 100 MHz) from its $<\uparrow>$ neighbor, due to the splitting induced by the perpendicular field, see Eq.(2.1). In the parallel polarity state $< 1 \downarrow 2 \downarrow >$, the $< 1 \downarrow >$ and $< 2 \downarrow >$ spectra should be superposed. Instead, only one auto-oscillation peak is observed with a much stronger amplitude and narrower linewidth. The frequencies, linewidths and integrated powers of the three states ($< 1 \downarrow >$, $< 2 \downarrow >$ and $< 1 \downarrow 2 \downarrow >$) can be extracted *vs.* the bias perpendicular field, and are plotted in panels (d), (e) and (f), respectively. For the $< 1 \downarrow 2 \downarrow >$ state, the linewidth is greatly reduced compared to the two individual peaks, by more than a factor of two, in the entire field range; the output power, plotted with the green curve of panel (f), is also larger than the sum of the two devices marked by the black dashed curve. All those evidences show that two STNOs are mutually synchronized, with coherent output and reduced phase noise.

In a final stage, we now would like to add the external microwave field $h_{\rm rf}$ to the system of two mutually coupled STVOs. This can be seen as adding a third reference oscillator. In Fig.3.14a, we first demonstrate that mutual dipolar coupling is at play between the two STVOs, since similarly to the situation shown in Fig.3.12c, oscillators $< 1 \downarrow >$ and $< 2 \uparrow >$ eventually get synchronized as the perpendicular field is reduced, with a critical frequency mismatch of 28 MHz.

We now fix both the biasing current and magnetic field and apply a weak microwave

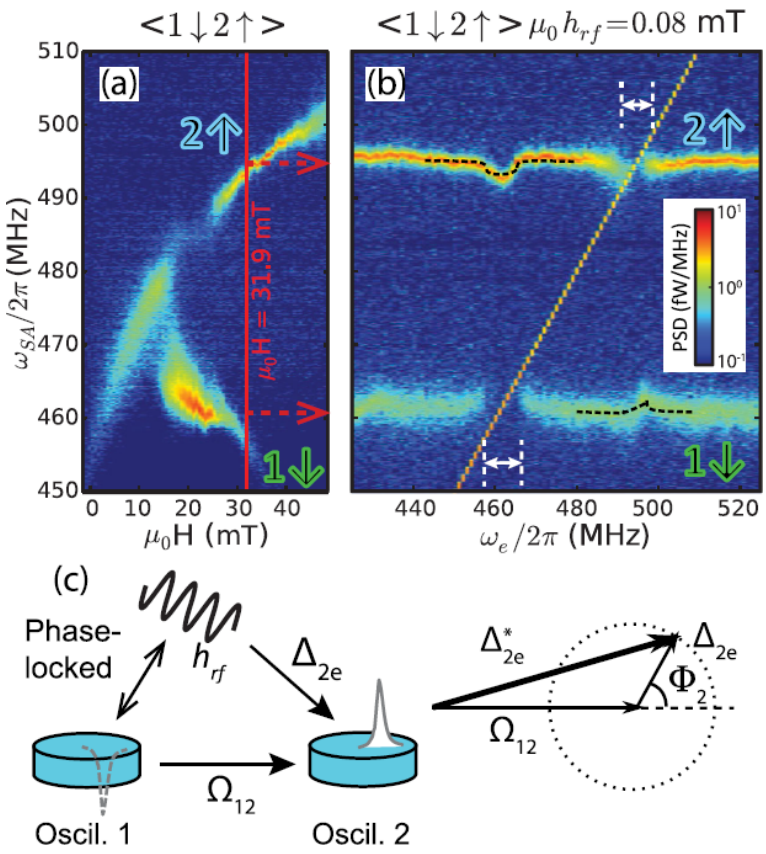

Figure 3.14: ***Probing the dipolar coupling between two STVOs with an external source.*** *(a) Power spectral density maps of auto-oscillation modes in the* $< 1 \downarrow 2 \uparrow >$ *state, for which mutual synchronization is observed between* $\mu_0 H = 17.5$ *and* 26.0 *mT. (b) Auto-oscillation spectra as a function of microwave field frequency for* $\mu_0 H = 31.9$ *mT, indicated in (a). The signal from the source appears as the oblique narrow line. The microwave power is* -23 *dBm, corresponding to* $\mu_0 h_{rf} = 0.08$ *mT. White arrows show the phase-locking bandwidths. Black dashed curves are fits to the analytical theory based on the vector diagram shown in (c) when oscillator 1 is phase-locked to the microwave field.*

field, which couples to both oscillators. The two vortex oscillators are set to an *unsynchronized* state at $\mu_0 H = 31.9$ mT, shown in Fig.3.14a. Fig.3.14b shows the evolution of auto-oscillation peaks of the two oscillators as a function of the external microwave field frequency ω_e. When ω_e crosses the peak of oscillator 1 around 460 MHz, the disappearance of the peak reflects the phase-locking to the external rf source. In addition, we also detect a significant frequency pulling on oscillator 2. This is a striking observation, because the frequency mismatch between oscillators, $(\omega_2 - \omega_1)/2\pi = 35$ MHz, is five times larger than the phase-locking bandwidths, around 7 MHz, of the two oscillators to the external source. The remote frequency pulling is a strong indication of coupling between the two oscillators as it is bound to the phase-locking bandwidth. It is important to note that no obvious frequency shift is observed when ω_e lies between the two auto-oscillation peaks. Reciprocally, a similar effect is also observed on oscillator 1 when oscillator 2 is phase-locked to the microwave field around 495 MHz.

To understand these phenomena, a simplified analytical formalism based on general oscillator equations can be developed. The main idea is that when oscillator i is phase-locked to the microwave field, it can help pulling the frequency of oscillator j towards the frequency of the source from the concerted actions of oscillator-oscillator and source-oscillator couplings, as pictured in Fig.3.14c. The detailed analysis of different sets of data [116] allows to extract the strength and the phase shift of the dipolar coupling between the two STNOs in anti-parallel and parallel sates of polarities, and confirm our previous findings. These results provide a new way to directly reveal and characterize the mutual coupling between oscillators through their attraction to a third reference oscillator, which can be applied to various oscillator systems.

Related publications

1. B. Pigeau, C. Hahn, G. de Loubens, V. V. Naletov, O. Klein, K. Mitsuzuka, D. Lacour, M. Hehn, S. Andrieu, F. Montaigne, *Measurement of the Dynamical Dipolar Coupling in a Pair of Magnetic Nanodisks Using a Ferromagnetic Resonance Force Microscope*, Phys. Rev. Lett. **109**, 247602 (2012).

2. F. Abreu Araujo, A. D. Belanovsky, P. N. Skirdkov, K. A. Zvezdin, A. K. Zvezdin, N. Locatelli, R. Lebrun, J. Grollier, V. Cros, G. de Loubens, O. Klein, *Optimizing magnetodipolar interactions for synchronizing vortex based spin-torque nano-oscillators*, Phys. Rev. B **92**, 045419 (2015).

3. N. Locatelli, A. Hamadeh, F. Abreu Araujo, A. D. Belanovsky, P. N. Skirdkov, R. Lebrun, V. V. Naletov, K. A. Zvezdin, M. Muñoz, J. Grollier, O. Klein, V. Cros, G. de Loubens, *Efficient Synchronization of Dipolarly Coupled Vortex-Based Spin Transfer Nano-Oscillators*, Sci. Rep. **5**, 17039 (2015).

4. Y. Li, X. de Milly, F. Abreu Araujo, O. Klein, V. Cros, J. Grollier, G. de Loubens. *Probing Phase Coupling Between Two Spin-Torque Nano-Oscillators with an External Source*, Phys. Rev. Lett. 118, 247202 (2017).

Résumé en français

L'étude spectroscopique d'hétérostructures est cruciale pour comprendre et améliorer les caractéristiques des STNOs. De fait, l'énergie, la relaxation, et les propriétés non-linéaires des modes d'ondes de spin des STNOs déterminent leur fréquence d'émission et leur pureté spectrale. De plus, leurs symétries spatiales donnent leurs règles de sélection et indiquent quels mécanismes de couplage peuvent exister intra ou inter STNOs.

Dans un premier temps, nous avons identifié les modes propres d'un STNO typique, un nano-pilier circulaire Py|Cu|Py (où Py=$Ni_{80}Fe_{20}$) de 200 nm de diamètre, et leurs règles de sélection. Ceci a été rendu possible par une étude MRFM détaillée de la configuration où les deux couches magnétiques sont aimantées hors du plan par un fort champ perpendiculaire (Fig.3.1), ce qui préserve la symétrie cylindrique et permet une approche analytique. Nous avons démontré que les modes excités par un champ micro-onde uniforme $h_{\rm rf}$ (index azimutal $\ell = 0$) sont différents de ceux qui le sont par un courant micro-onde $i_{\rm rf}$ traversant l'échantillon en raison de la symétrie orthoradiale du champ d'Oersted généré par $i_{\rm rf}$ ($\ell = 1$) (Fig.3.2). Ensuite, nous avons mesuré la puissance émise par transfert de spin par ce STNO dans le régime autonome (Fig.3.3). Cette mesure MRFM quantitative a permis d'identifier le premier mode à auto-osciller : le mode de plus basse énergie (le plus uniforme) dominé par la couche fine de Py. Nous avons aussi vérifié dans le régime forcé que la source externe doit avoir la même symétrie que le mode auto-oscillant pour le verrouiller en phase : $h_{\rm rf}$ doit donc être utilisé plutôt que $i_{\rm rf}$ (Fig.3.4). Le cas où la symétrie cylindrique est légèrement brisée a été également étudié : un régime bi-modal est alors observé (Fig.3.6), et un couplage non-linéaire entre les modes $\ell = 0$ et $\ell = 1$ a été mis en évidence (Fig.3.7).

Le même STNO a été étudié dans la configuration où un vortex est stabilisé dans chacune des couches magnétiques. Grâce au courant dc traversant l'échantillon et au champ perpendiculaire appliqué, la chiralité et la polarité des deux vortex peuvent être contrôlées. Quand les chiralités sont parallèles, seul l'état de polarités opposées conduit à l'émission d'un signal micro-onde. Ce dernier est remarquable par sa grande pureté spectrale (largeur de raie < 100 kHz, fréquence 600–900 MHz), qui est dix fois supérieure que celle observée lorsqu'un seul vortex est présent dans le nano-pilier. Nous avons démontré que contrairement aux STNOs classiques, ce STNO basé sur des vortex couplés est quasi-isochrone (linéaire), ce qui supprime le fort élargissement dû au couplage amplitude-phase non-linéaire. Nous avons aussi mis en évidence l'influence des modes propres amortis du système sur la pureté spectrale du mode auto-oscillant (Fig.3.8). En outre, malgré ses faibles non-linéarités, ce STNO conserve une forte tunabilité en courant (8 MHz/mA) grâce au champ d'Oersted généré par le courant, ce qui est attractif pour les applications. Il est également à noter que ce STNO peut être efficacement synchronisé à une source externe ($h_{\rm rf}$), puisque le signal peut atteindre la pureté spectrale de la source (*i.e.*, le verrouillage de phase est parfait) sur une grande gamme de paramètres (Fig.3.9).

Cette dernière observation est prometteuse pour le mécanisme de synchronisation mutuelle de plusieurs STNOs par interaction dipolaire. Ici, l'idée est de remplacer la source externe par le champ dipolaire rayonné par un STNO voisin. Dans cette optique, nous avons d'abord mesuré quantitativement le couplage dipolaire dynamique dans une paire de nano-disques adjacents en fonction de leur séparation avec un MRFM (Fig.3.10). Nous avons ensuite observé la synchronisation mutuelle par couplage dipolaire de deux STNOs voisins basés sur des vortex. Un résultat notable est que comme attendu,

l'interaction dipolaire dynamique est trois fois plus élevée lorsque les cœurs des vortex présents dans les STNOs adjacents sont anti-parallèles que parallèles (Fig.3.12). Ensuite, nous avons ajouté une source externe (h_{rf}), qui peut-être considéré comme un troisième oscillateur. Nous avons étudié son influence sur la dynamique des deux oscillateurs couplés dipolairement dans le cas où ils ne sont pas synchronisés. Lorsque la source verrouille la phase d'un des deux oscillateurs, la fréquence de l'autre oscillateur est affectée du fait du couplage mutuel entre oscillateurs (Fig.3.14). Ces expériences permettent de déterminer quantitativement l'intensité et le retard de phase du couplage dipolaire entre oscillateurs, deux paramètres cruciaux qui contrôlent l'état de synchronisation des oscillateurs.

Chapter 4

Magnetization dynamics in magnetic insulators / normal metal hybrids

Due to interfacial exchange coupling, the electrons in a normal metal (N) can exchange spin angular momentum with an adjacent ferromagnetic layer (F). This interfacial exchange coupling has been studied for several decades in the situation where the ferromagnet is metallic, *i.e.*, electrons of each layer have the possibility to penetrate the other one at the F|N interface, with a variety of phenomena which are at the heart of the field of spintronics. In particular, it constitutes an additional channel of relaxation for the out-of-equilibrium magnetization of the ferromagnets, which can be referred as spin pumping [183]. Due to Onsager reciprocity, if the ferromagnet can emit a spin current at the F|N interface, it can also absorb some. One recent breakthrough on this topic was to demonstrate that interfacial exchange coupling is also relevant when the ferromagnet is *insulating*. More precisely, a pioneering work [94] showed that it was possible to transmit pure spin currents at a YIG|Pt interface, where YIG = $Y_3Fe_5O_{12}$ stands for Yttrium iron garnet, a ferrimagnetic insulating material, and to produce and detect them owing to the spin Hall effect (SHE) and its inverse (ISHE), respectively, that exist in platinum due to the strong spin-orbit interaction [51, 88].

One outstanding feature in this seminal study was the detection of auto-oscillations in the 1.3 μm thick YIG layer when enough dc current was passed in the 10 nm thick Pt layer. This finding has created a great excitement in the community because one could control electronically the damping of insulators, which can offer improved properties compared to metals (YIG has the lowest damping known in nature, $\alpha = 3\ 10^{-5}$ [167]). Moreover, owing to the spin Hall effect, which allows to produce a spin current transverse to the in-plane charge current, hence to generate a spin-orbit torque all along the F|N interface, the damping compensation could be achieved on large objects, a relevant point for the field of magnonics [107, 29] whose aim is to use spin-waves as carriers of information.

One big surprise to us and other groups was the extremely low threshold current to reach the auto-oscillation regime in such a thick YIG film reported in ref. [94], about $5\ 10^8$ A/m^2, which is three orders of magnitude smaller than expected by simple analysis [199], see Eq.(1.4). The spin-orbit torque being an interfacial effect, it is clear that ultra-thin YIG films of high dynamical quality should be used to observe sizeable effects. This triggered an intense effort to grow ultra-thin films of YIG of high dynamical quality, in particular by pulsed laser deposition (PLD) [173, 141, 85] and off-axis sputtering [194].

In the following, we rely on 20 nm thick YIG grown by PLD in the group of Madjid

Anane (UMR CNRS/Thales) and on YIG films grown by liquid phase epitaxy (LPE) with thickness in the range 20–200 nm, provided by Jamal Ben Youssef (UBO/Lab-STICC), both on Gadolinium Gallium garnet (GGG) (111) substrates. This chapter is divided in two main parts. Based on studies performed on extended hybrid films, section 4.1 presents different experimental evidences of the interfacial coupling between YIG and adjacent heavy metal (Pt and Ta) layers: through the interfacial enhancement of the Gilbert damping parameter in YIG|Pt bilayers, the electrical conversion of the spin current emitted by the dynamical YIG magnetization in the adjacent heavy metal layer by inverse spin Hall effect, and the observation of spin Hall magnetoresistance. We also demonstrate conduction of spin currents through the antiferromagnetic oxide NiO, which is intercalated between YIG and Pt layers. In section 4.2, these hybrid layers are patterned into micro- and nano-disks, and we study the effects of spin-orbit torque provided by the injection of dc current in Pt on the magnetization dynamics. In particular, we demonstrate that it can lead to the auto-oscillations in YIG|Pt micro-disks, whose spectral and spatial characteristics are investigated in details and reveal the importance of nonlinear coupling between spin-wave modes.

4.1 Interfacial coupling in hybrid magnetic systems

4.1.1 Transmission of pure spin currents at a YIG / normal metal interface

Interfacial enhancement of the damping

First, we perform a thorough comparative study of LPE grown YIG and YIG|Pt(7 nm) films as a function of the YIG thickness $t_{\rm YIG}$ by in-plance and out-of-plane broadband FMR, from 1 GHz up to 40 GHz. The summary of the standard analysis allowing to extract the effective fields (panel a), gyromagnetic ratios (b), inhomogeneous contributions to the linewidth (c), and Gilbert damping parameters (d) as a function of $t_{\rm YIG}$ is presented in Fig.4.1. The main result is the observed interfacial increase of the damping parameter α of the YIG|Pt bilayer with respect to the one α_0 of the bare YIG film in panel d (where the red continuous line is a $\propto 1/t_{\rm YIG}$ fit to the data), which allows to extract the spin mixing conductance $g_{\uparrow\downarrow}$ from the following formula,

$$\alpha - \alpha_0 = g_{\uparrow\downarrow}\frac{\gamma\hbar}{4\pi M_{\rm s} t_{\rm YIG}}\,, \tag{4.1}$$

found to lie in the range $2-4\ 10^{18}$ m^{-2}, in agreement with other similar studies on films elaborated by PLD [86, 93, 75]. This damping enhancement is a direct signature that a spin current is being pumped out of the precessing YIG layer and absorbed in the Pt layer.

Other interesting comments should be made concerning the magnetic parameters extracted in Fig.4.1. First, the Gilbert damping parameter of the bare YIG films (blue dots in panel d) also increases inversely to the thickness, which suggests an important role of the GGG|YIG interface. For the thicker 200 nm films, the damping is only slightly larger than bulk YIG (see horizontal dashed line), while below 50 nm, it lies in the $1.5-5\ 10^{-4}$ range, as observed in the best PLD grown films [35]. The inhomogeneous contribution to the linewidth ΔH_0 is only a couple of Oersteds in the whole window of thickness (panel

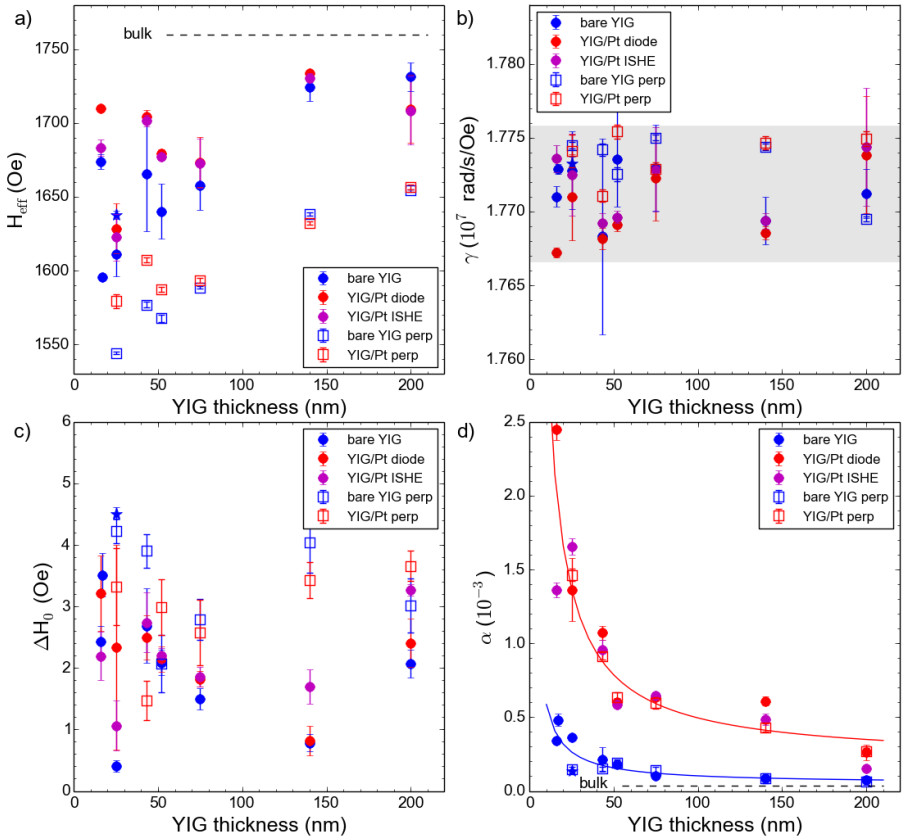

Figure 4.1: ***Thickness dependence of dynamical properties of LPE grown ultra-thin YIG films.*** *(a) Effective field, (b) gyromagnetic ratio, (c) inhomogeneous contribution to the linewidth and (d) Gilbert damping parameter vs. YIG thickness. These parameters are extracted from broadband FMR (1 GHz – 40 GHz), with in-plane (filled dots) and out-of-plane field orientations (open squares). Blue symbols are for bare YIG, red symbols for YIG|Pt(7 nm).*

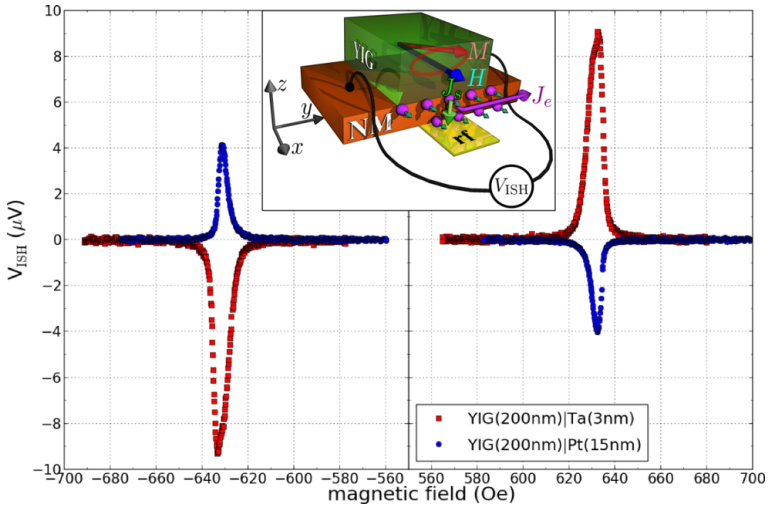

Figure 4.2: ***Comparative study of ISHE in YIG|Ta and YIG|Pt.*** *Inverse spin Hall voltage measured at 3.5 GHz for YIG(200 nm)|Ta(3 nm) and YIG(200 nm)|Pt(15 nm) bilayers. Inset: sketch of the experiment.*

c), which highlights the excellent quality of the films. In panel (b), we do not observe any trend on the behavior of the gyromagnetic ratio γ, which is close to the bulk value ($1.765\ 10^7$ rad/s/Oe). Finally, we observe that the effective field H_{eff} decreases with the YIG thickness in panel (a), which is due to a lower magnetization of the ultra-thin films, as confirmed by VSM measurements. The difference between the values of H_{eff} extracted in parallel (solid dots) and perpendicular geometries (open squares) originates from the cubic anisotropy of YIG [121]. A detailed analysis [123] of angle-dependent FMR experiments at fixed frequency allows to extract accurately its value, as well as a small uniaxial anisotropy.

Inverse spin Hall detection of FMR

Following the work of Kajiwara et al. [94], many groups reported on the electrical detection of spin currents emitted at the YIG|Pt interface by different kinds of spin-waves [158, 108, 189, 28, 21, 194]. In our case, we chose to compare the ISHE voltages produced in Pt and Ta layers, as presented in Fig.4.2. The spin current J_s pumped into the adjacent normal metal by the precessing magnetization in YIG is converted into a charge current by ISHE,

$$J_e = \frac{2e}{\hbar}\Theta_{SH} J_s\,, \tag{4.2}$$

where e is the electron charge, $\hbar$ the reduced Planck constant and Θ_{SH} the spin Hall angle. This leads to a transverse voltage V_{ISHE} (across the length of the YIG|N slab), as sketched in the inset of Fig.4.2. Moreover, V_{ISHE} must change sign upon reversing the magnetization of YIG because of the concomitant reversal of the spin pumped current J_s (hence J_e). This is observed in both the YIG|Pt and YIG|Ta systems, where V_{ISHE} is odd in applied magnetic field, which shows that the voltage generated at resonance is not due to a thermoelectrical effect.

The striking feature to be observed here is the opposite signs of V_{ISHE} in these two samples. It confirms that the spin Hall angles in Ta and Pt have opposite signs, as

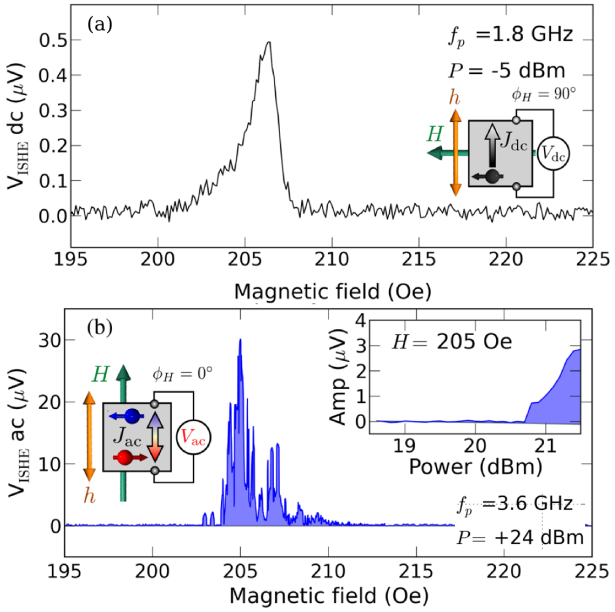

Figure 4.3: ***dc and ac ISHE voltages.*** *(a) Standard FMR with the low power pumping field h at $f_p = 1.8$ GHz oriented perpendicularly to the static magnetic field H. The dc ISHE voltage is measured perpendicularly to H. (b) Parametric excitation with the large power pumping field h at $f_p = 3.6$ GHz oriented parallel to the static magnetic field H. The ac ISHE voltage generated at $f_p/2 = 1.8$ GHz is monitored on a spectrum analyzer. Its amplitude is measured as the bias field is swept from 195 to 225 Oe. The inset shows the threshold behavior ($P_c \simeq +20.7$ dBm) of the power dependence of the spectrum analyzer signal at 1.8 GHz.*

predicted by ab initio calculations [174] and inferred from other measurements [131]. Moreover, from the electrical circuit which was used in the measurements, it can be determined that $\Theta_{SH}^{\mathrm{Pt}} > 0$ while $\Theta_{SH}^{\mathrm{Ta}} < 0$. The precise estimation of the spin Hall angles in these two materials requires a thorough analysis the dependence of the ISHE signal on their thickness [21, 76].

It is interesting to note that the pumped spin current at the YIG|Pt has actually both dc and ac components, as it writes [183]:

$$\boldsymbol{J}_s = \left(\frac{\hbar}{2eM_s}\right)^2 G_{\uparrow\downarrow}\left[\boldsymbol{M} \times \frac{\partial \boldsymbol{M}}{\partial t}\right] . \tag{4.3}$$

In this expression, $G_{\uparrow\downarrow}$ the spin mixing conductance is expressed in units of $\Omega^{-1}{\cdot}\mathrm{m}^{-2}$, and is simply related to the $g_{\uparrow\downarrow}$ introduced in Eq.(4.1) by $g_{\uparrow\downarrow} = G_{\uparrow\downarrow}/G_0$, with $G_0 = 2e^2/h$ the quantum of conductance.

The ac component of spin pumping, which lies in the GHz range, is in principle quite tricky to detect experimentally, due to unavoidable inductive couplings in the circuit [78, 195, 197]. To minimize measuring the parasitic eddy currents induced at the frequency of the microwave source, we proposed to excite the YIG magnetization dynamics at half the frequency using parametric excitation in the parallel geometry, in which the high-wave vector excited spin-waves in the 200 nm thick YIG poorly couple to the inductive detection scheme [79, 78]. This is realized in Fig.4.3, whose panels (a) and (b) respectively show the detection of the dc ISHE voltage at 1.8 GHz in a standard transverse FMR experiment and of its ac counterpart in parallel pumping geometry at twice the frequency. Beyond the

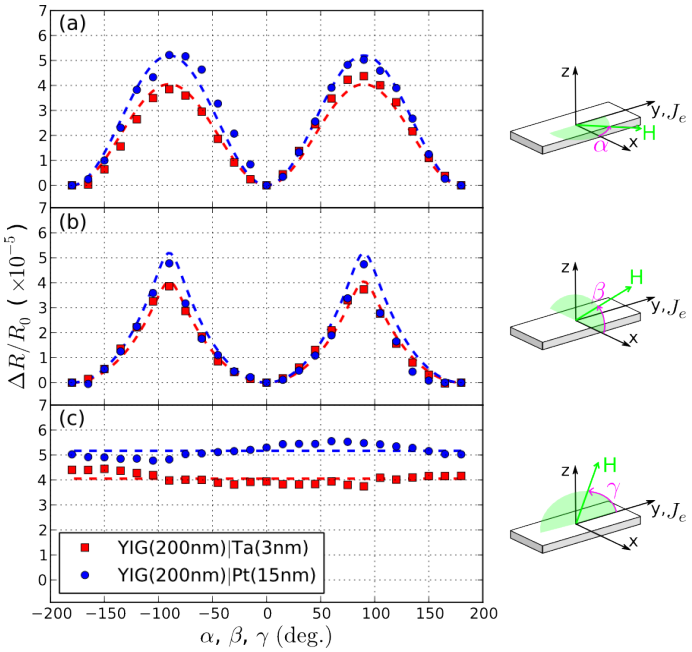

Figure 4.4: ***Spin Hall magnetoresistance.*** *(a-c) Magnetoresistance in YIG|Ta and YIG|Pt as a function of the angle of the applied field ($H = 3$ kOe) sketched on the right (the samples are the same as the ones measured in Fig.4.2). Dashed lines are predictions from Eq.(4.4).*

fact that indeed, an ac component can be detected, those data are interesting because they show that the FMR line, which can be seen in panel (a), is inhomogeneously broadened: many quasi-degenerated spin-wave modes do contribute to it, as it is clear from panel (b).

Spin Hall magnetoresistance

The inferfacial exchange coupling at a F|N interface does also manifest itself in the so-called spin Hall magnetoresistance (SMR) effect [133]. The physical picture is that the electronic transport in the N layer can be affected by the static magnetization in the F layer as electrons spins separated by SHE can undergo different spin-flip scattering on the interface with the F layer. In particular, spin flipped electrons are deflected by ISHE in a direction opposite to the initial current, leading to a reduced total current at constant voltage. This effect depends on the relative angle between the magnetization $\boldsymbol{M}$ of the ferromagnet and the accumulated spins $\boldsymbol{s}$ at the F|N interface [133, 25]:

$$R = R_0 + \Delta R_{\text{max}} \sin^2 (\boldsymbol{M}, \boldsymbol{s}) \,. \tag{4.4}$$

Fig.4.4 displays the variation of resistance in the same samples as the ones studied by ISHE in Fig.4.2, as a function of the angle of the applied field ($H = 3$ kOe) with respect to the three main axes of the slabs, as shown in the sketches on the right of the corresponding panels. With usual anisotropic magnetoresistance (AMR), R depends on the angle between the charge current and the magnetization. Hence, no change of R is expected with the angle β, whereas R should vary with the angle γ, which is exactly opposite to what is observed in Figs.4.4b and 4.4c, respectively. Therefore usual AMR as the origin of the magnetoresistance in YIG|Pt and YIG|Ta bilayers has to be excluded. Instead, we can interpret our data with the SMR scenario and Eq.(4.4). Here, the increase

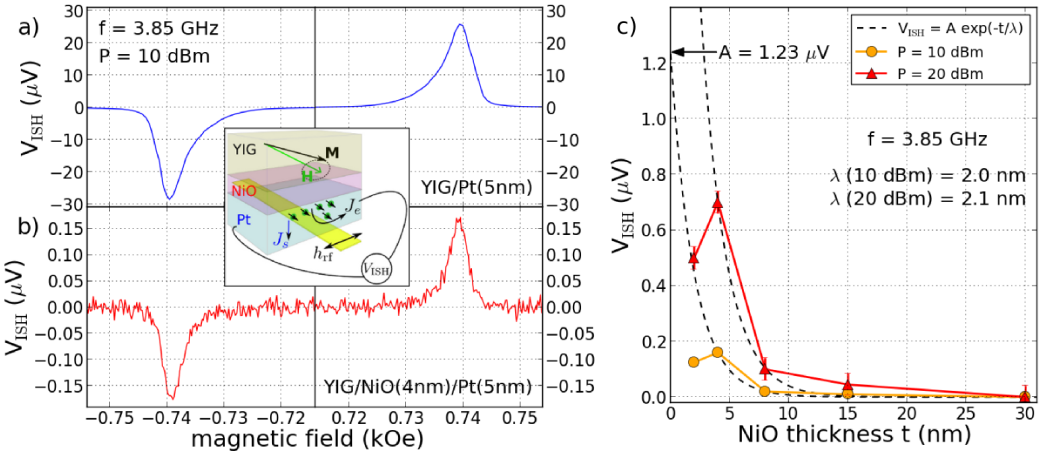

Figure 4.5: ***Conduction of spin currents through NiO.*** *(a) ISHE signal measured in a YIG|Pt bilayer generated by the spin current emitted by the YIG at resonance at a frequency of 3.85 GHz and a power of 10 dBm. (b) Similar signal when a 4 nm NiO layer is inserted between YIG and Pt. Note the difference in scale for the measured ISHE voltage. Inset: geometry of the measurement. (c) NiO thickness dependence of the angular momentum transfer in YIG|NiO(t)|Pt devices at 3.85 GHz and two different powers: 10 and 20 dBm. The diffusion length from the exponential fits is close to 2 nm. The significant difference between the signal extrapolated to zero NiO thickness and that of the pure YIG|Pt sample gives an estimate interface YIG|NiO transparency of 0.05.*

of resistance is maximal when $\boldsymbol{M}$ and $\boldsymbol{s}$ are perpendicular, because the spin-flip scattering governed by $G_{\uparrow\downarrow}$ at the interface is the largest. Hence, the observation of SMR is YIG|Pt and YIG|Ta is another evidence that spin currents can be transmitted at those interfaces, even more, it shows that spin transfer torques, which are crucial to explain the SMR [25], are at play.

4.1.2 Conduction of spin currents through the antiferromagnetic oxide NiO

Like magnons in ferromagnets, antiferromagnetic magnons are intrinsically spin charged as they correspond to the reversal of a single spin in an antiferromagnetic crystal spreading into a somehow more delocalized entity [103]. Therefore, they could potentially be good conductors of spin currents, as YIG. To test this idea, we have performed similar measurements as in Fig.4.2, but with a NiO layer of variable thickness intercalated in between the YIG and Pt. In these experiments, the precessing magnetization of YIG can be seen as the source of spin current via the spin pumping effect (Eq.(4.3)) while the Pt acts as a detector of spin current, via ISHE (Eq.(4.2)). Our experimental results [77], summarized in Fig.4.5 demonstrate that spin currents can indeed be transmitted through NiO (contrary to non-magnetic materials, such as SiO_2, which we used in a control experiment), and were independently confirmed [193]. We note that in the last couple of years, a strong activity activity has started in antiferromagnetic spintronics (see end of section 5.3), here we show that insulating antiferromagnetic materials are potential interesting candidates.

Related publications

1. C. Hahn, G. de Loubens, O. Klein, M. Viret, V. V. Naletov, J. Ben Youssef, *Comparative measurements of inverse spin Hall effects and magnetoresistance in YIG/Pt and YIG/Ta*, Phys. Rev. B **87**, 174417 (2013).
2. O. d'Allivy Kelly, A. Anane, R. Bernard, J. Ben Youssef, C.Hahn, A. H. Molpeceres, C. Carrétéro, E. Jacquet, C. Deranlot, P. Bortolotti, R. Lebourgeois, J.-C. Mage, G. de Loubens, O. Klein, V. Cros, A. Fert, *Inverse spin Hall effect in nanometer-thick yttrium iron garnet/Pt system*, Appl. Phys. Lett. **103**, 082408 (2013).
3. C. Hahn, G. de Loubens, M. Viret, O. Klein, V. V. Naletov, J. Ben Youssef, *Detection of Microwave Spin Pumping Using the Inverse Spin Hall Effect*, Phys. Rev. Lett. **111**, 217204 (2013).
4. C. Hahn, G. de Loubens, V. V. Naletov, J. Ben Youssef, O. Klein, M. Viret, *Conduction of spin currents through insulating antiferromagnetic oxides*, EPL **108**, 57005 (2014).
5. J.-Y. Chauleau, M. Boselli, S. Gariglio, R. Weil, G. de Loubens, J.-M Triscone, M. Viret. *Efficient spin-to- charge conversion in the 2D electron liquid at the LAO/STO interface*, EPL **116**, 17006 (2016).

4.2 Spin-orbit torque driven auto-oscillations in YIG/Pt systems

As noted in the introduction of this chapter, a really exciting possibility offered by the spin-orbit torque that acts at a YIG|Pt interface is to control the relaxation in the YIG layer, and even to compensate it to drive auto-oscillations of the magnetization, similarly to what happens in traditional STNOs. However, despite the seminal report showing such effects at remarkably low current densities, tailoring this experiment on extended films has proven to be elusive. We ourselves tried our best to detect some variation of the FMR linewidth in YIG|Pt bilayers (both on 200 nm thick LPE grown YIG [76] and 20 nm thick YIG PLD grown YIG [35]) at the highest dc current possible in the Pt layer ($\approx 6\ 10^9$ A/m^2, that is, before it evaporates), but without success. It is worth mentioning that reducing further the thickness or the damping parameter of such ultra-thin YIG films does not help much in decreasing the threshold current given by Eq.(1.4), as the relevant value of the damping is that of the YIG|Pt hybrid, which ends up to be completely dominated by the spin-pumping, see Eq.(4.1).

Moreover, none of the high-quality ultra-thin YIG films display a purely homogeneous FMR line [173, 35], even if the values of ΔH_0 can be low (see Fig.4.1c). In fact, in such extended films, there are many degenerate modes with the main, uniform FMR mode (see Fig.4.3b), which through the process of two-magnon scattering broaden the linewidth [4, 124]. Any threshold instability will be affected by their presence, as learnt from LASERs where mode competition is known to have a strong influence on the emission threshold [5]. Hence, a natural idea is to reduce the lateral size in order to lift the degeneracy between spin-wave modes through confinement. Moreover, nanostructuring the YIG|Pt and the metallic electrodes on top of the GGG substrate will help thermalization, and allow to inject larger current densities (possibly up to 10^{12} A/m^2), as in standard STNOs. In the

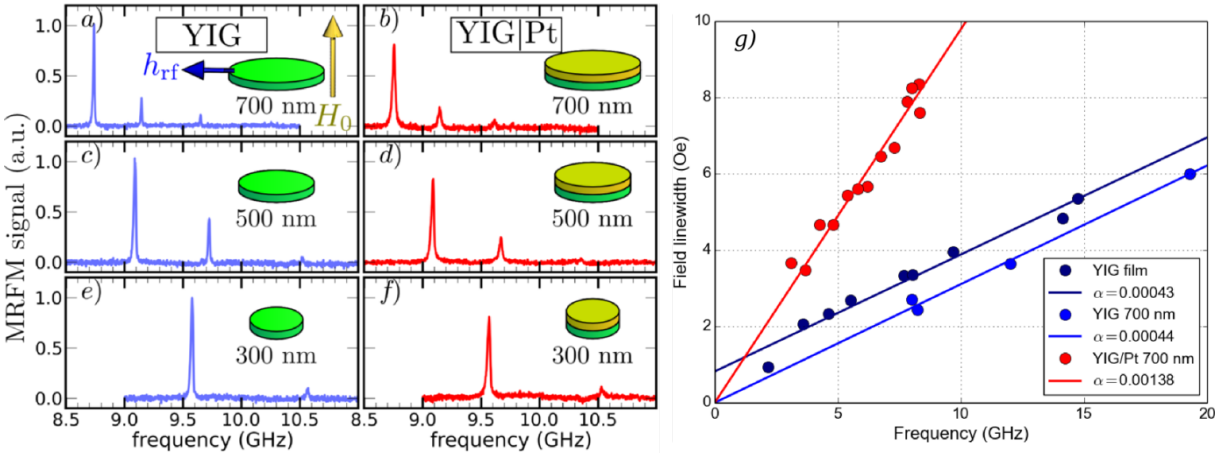

Figure 4.6: ***Spin-wave spectroscopy in YIG and YIG/Pt nano-disks.*** *(a-f) MRFM spectra at H_0=4.99 kOe of 700, 500 and 300 nm diameter YIG nano-disks (20 nm thick) arranged in rows by decreasing lateral size. The spectra of the bare YIG disks are shown in the left column (blue), while the ones covered with 13 nm of Pt are shown in the right column (red). (g) Dependences of the linewidth on the resonance frequency and corresponding linear fits for the reference YIG film, the 700 nm bare YIG disk, and the 700 nm YIG disk covered with Pt.*

following two sections, we thus present spectroscopic studies on nano- and microstructures of YIG and YIG|Pt patterned from 20 nm thick PLD YIG, and investigate the influence of dc spin-orbit torque on their dynamics.

4.2.1 Comparative spectroscopic study of YIG and YIG/Pt nano-disks

Fig.4.6 presents the comparative MRFM spectroscopic study of YIG and YIG|Pt nano-disks, having three different nominal diameters, 700, 500 and 300 nm, in the fully out-of-plane saturated state. The effect of the confinement on the spin-wave mode spectra is obvious [96, 104, 134]. Very remarkably, the addition of 13 nm of Pt on top the disks does not change at all the position of the spin-wave modes, but does affect substantially their linewidth. Fig.4.6g shows the dependence of the latter for the largest 700 nm diameter disks, with and without Pt, as well as of the reference YIG film, from which the disks were patterned. We observe that the patterning does not affect the Gilbert damping parameter at all, found to be slightly larger than 4 10^{-4} in both the reference film and the bare YIG nano-disk. We also observe that the small inhomogeneous contribution to the linewidth, $\Delta H_0 \simeq 0.9$ Oe, observed in the film, completely vanishes in the nano-disk, which is expected due to the complete removal of mode degeneracy in the nanostructure [38, 23].

Besides the results summarized in Fig.4.6 and published a few years ago [80], I would like to mention that these nano-disks of very high quality are still under investigation. Their spin-wave spectra have been measured in the in-plane configuration, where again, the effects of confinement is clearly visible. They have also been measured as a function of temperature, from room temperature down to 10 K, in our variable temperature MRFM. Finally, they are very nice samples to probe the highly nonlinear regime of FMR, as presented in section 5.2.1.

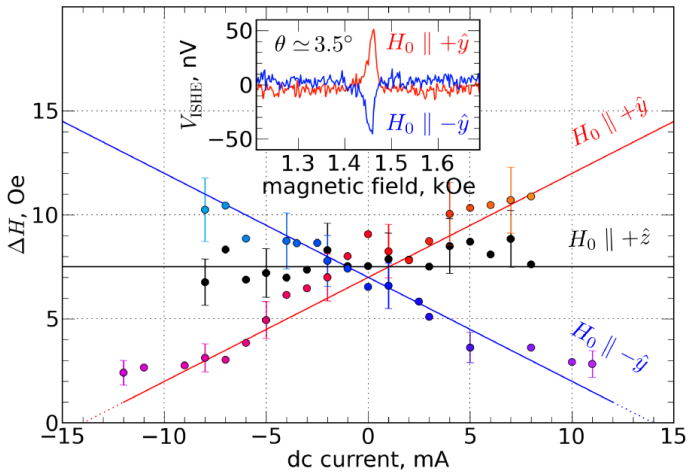

Figure 4.7: ***Full control of the damping using spin-orbit torque****. The sample is a 5 μm diameter YIG(20 nm)|Pt(7 nm) disk. The main panel shows the variation of the full linewidth measured by MRFM spectroscopy at 6.33 GHz as a function of the dc current for out-of-plane field (black) and two opposite in-plane field (red and blue) configurations. The dc current is injected in the direction transverse to the in-plane field. The inset shows the detection of V_{ISHE} in the transverse direction of the in-plane swept magnetic field at $I_{dc} = 0$.*

4.2.2 Electrical control of damping in YIG/Pt micro-disks

The previous YIG|Pt nano-disks are not connected to electrodes, which prevents applying a dc current in the Pt and observing the effect of spin-orbit torque. For this, we instead rely on larger structures, namely, micro-disks (diameter ranging between 2 and 5 μm), to which gold electrodes are contacted. Moreover, in order to maximize the effect of spin-orbit torque, the samples are biased in the plane, with the magnetic field H oriented transversely to the dc current $I_{\rm dc}$ flowing in the Pt layer, as in the sketch of Fig.4.8a. This is the most favorable configuration to compensate the damping and obtain auto-oscillations in YIG, as spins accumulated at the YIG|Pt interface due to SHE in Pt will be collinear to its magnetization.

Using MRFM, we monitor the evolution of the in-plane (negative/positive bias) and out-of-plane spin-wave spectra of a 5 μm diameter YIG|Pt disk as a function of the dc current injected into the 7 nm thick Pt layer. We have reported in FIG.4.7 the values of the full linewidth measured at 6.33 GHz in these geometries with respectively blue/red and black symbols, as a function of current. The blue/red data points follow approximately a straight line, whose slope ± 0.5 Oe/mA reverses with the direction of the bias field, and whose intercept with the abscissa axis occurs at $I^*_{6.33\ \rm GHz} = \mp 12$ mA, which correspond to a current density of about 4 10^{11}A/m^2. The variation of linewidth covers about a factor five on the full range of current explored. In contrast, the linewidth measured in the out-of-plane geometry does not change with current. In fact, no net spin transfer torque is exerted by the spin current on the precessing magnetization in this configuration.

We have also plotted in the inset of FIG.4.7 the inverse spin Hall voltage $V_{\rm ISHE}$ measured at $I_{\rm dc} = 0$ mA and $f = 6.33$ GHz on the same sample, for the two opposite orientations of the in-plane bias field. This allows to check that a spin current can be transmitted from YIG to Pt, and which polarity of the current is required to compensate the damping. In our experiment, damping compensation occurs when the product of

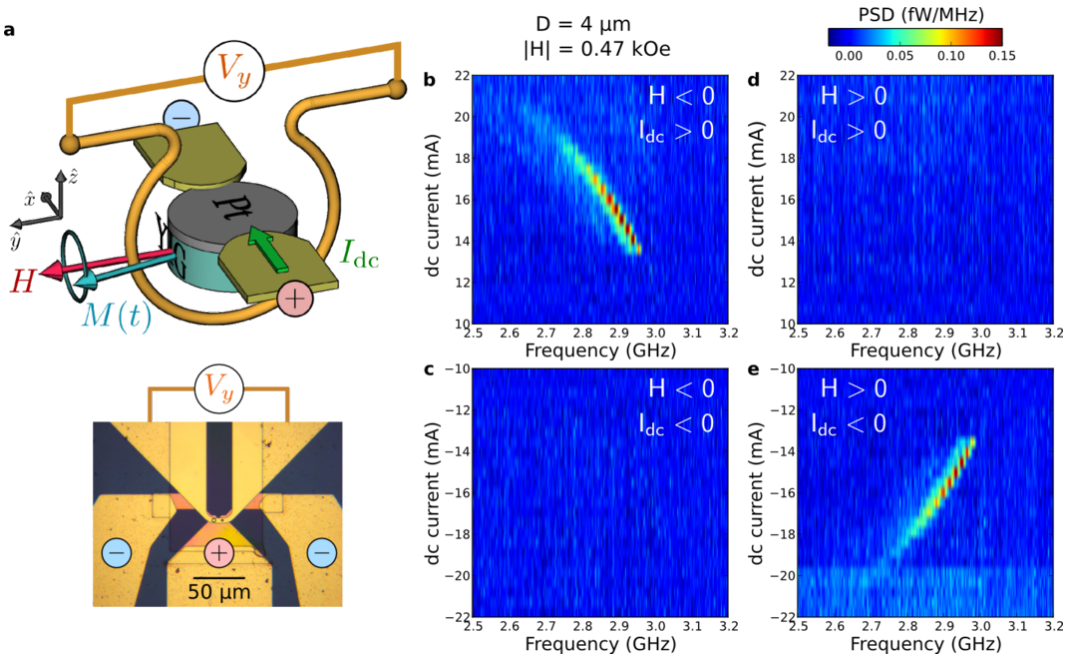

Figure 4.8: ***Electrical detection of auto-oscillations.*** *(a) Sketch of the measurement configuration and microscopy image of a device with two micro-disks connected (underneath the circles). The bias field H is oriented transversely to the dc current I_{dc} flowing in Pt. The inductive voltage V_y produced in the antenna by the precession of the YIG magnetization $M(t)$ is amplified and monitored by a spectrum analyzer. (b-e) Power spectral density maps measured on a 4 μm YIG|Pt disk at fixed $|H| = 0.47$ kOe and variable I_{dc}. The four quadrants correspond to different possible polarities of H and I_{dc}. An auto-oscillation signal is detected above a threshold current of ± 13 mA if $H \cdot I_{dc} < 0$, in agreement with the symmetry of spin-orbit torque.*

V_{ISHE} and I_{dc} is negative. This is consistent with having a positive spin Hall angle in Pt, Θ_{SH}.

The results of Fig.4.7 unambiguously demonstrate that spin-orbit torque can be used to control the relaxation of a YIG|Pt hybrid, and the current density extrapolated to reach the threshold are those expected using our experimental parameters, and Eq.(1.4) [199]. By solely biasing the sample with dc current (no microwave applied), we were also able to detect with our MRFM setup the signature of the onset of auto-oscillations beyond the threshold current [81], similarly to the experiment performed on the spin-valve nanopillar STNO of Fig.3.3. In the following, we present the direct electrical detection of these auto-oscillations, using a similar YIG|Pt micro-disk sample with a microwave antenna defined around it to obtain an inductive coupling with the YIG magnetization, as shown schematically in Fig.4.8a.

Using this sample, we monitor with a spectrum analyzer the voltage produced in the antenna by potential auto-oscillations of a 4 μm YIG disk as a function of the dc current I_{dc} injected in Pt. Color plots of the inductive signal measured as a function of the relative polarities of H and I_{dc} are presented in Fig.4.8b–e. The magnetic field is set to $|H| = 0.47$ kOe. At $H < 0$, we observe in the power spectral density (PSD) a peak which starts at around 2.95 GHz and 13 mA and then shifts towards lower frequency as I_{dc} is increased (Fig.4.8b), a clear signature that spin transfer occurs through the YIG|Pt interface. An identical behavior is observed at $H > 0$ and $I_{\mathrm{dc}} < 0$ (Fig.4.8d). In

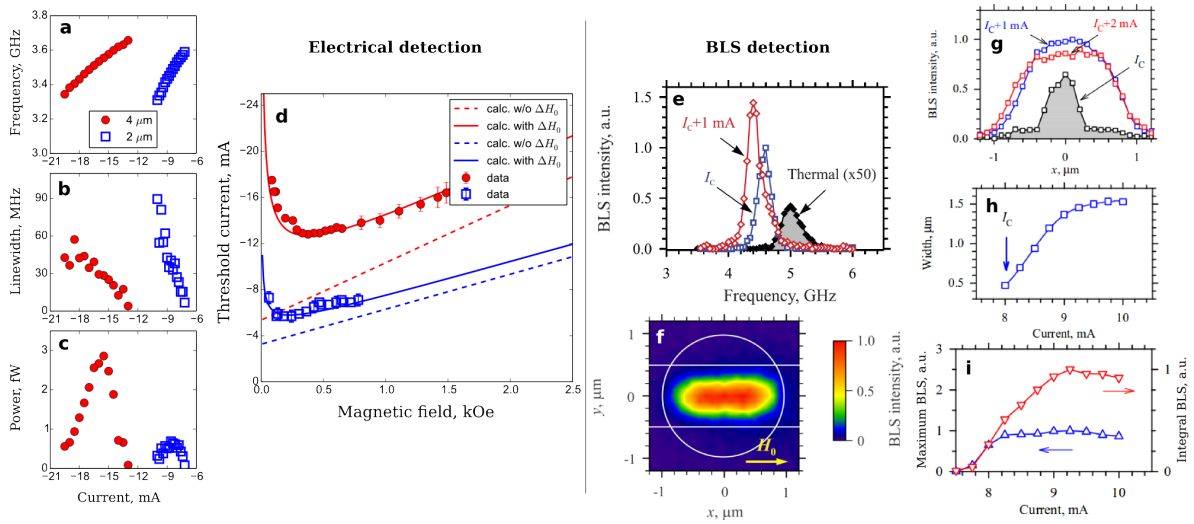

Figure 4.9: ***Evolution of electrical and μ−BLS signals above the auto-oscillation threshold.*** Left: *electrical detection of auto-oscillations in the 4 µm and 2 µm YIG|Pt disks. The experimental configuration is the same as in Fig.4.8a, with the bias field fixed to $H = 0.65$ kOe. (a) Auto-oscillation frequency f, (b) linewidth Δf and (c) integrated power vs. dc current. (d) Dependence of the threshold current on the applied field in both disks. Expectations taking into account only the homogeneous linewidth or the total linewidth are respectively shown by dashed and continuous lines.* Right: *μ−BLS detection of auto-oscillations in the 2 µm YIG|Pt disk at $H = 1$ kOe. (e) BLS spectra recorded by placing the probing laser spot in the middle of the YIG disk for different dc currents: black solid symbols – $I_{dc} = 0$, blue open squares – $I_{dc} = I_C \simeq 8$ mA, red open diamonds – $I_{dc} = I_C + 1$ mA. The intensity of the peak for $I_{dc} = I_C$ is by about two orders of magnitude larger compared to that for $I_{dc} = 0$. (f) Spatial map recorded for $I_{dc} = I_C + 1$ mA of the intensity of current-induced magnetic auto-oscillations in the YIG disk. The contours of the disk and the edges of the electrodes are shown by white lines. (g) Spatial profiles of the oscillation intensity in the direction along the gap between the electrodes recorded for different dc currents. (h) Current dependence of the full width at half maximum of the spatial profiles. (i) Current dependences of the maximum intensity of the auto-oscillations detected in the center of the gap and that of the spatially-integrated intensity.*

contrast, the PSD remains flat in the two other cases (Fig.4.8c–d). Therefore, an auto-oscillation signal is detected only if $H \cdot I_{\rm dc} < 0$, in agreement with the expected symmetry of SHE and the previous conclusions of Fig.**??**. Moreover, as opposed to numerous peaks previously observed over an almost 1 GHz wide frequency range [94], a single emission peak is detected here by spectral analysis. The linewidth of this emission peak lies in the 10–20 MHz range for $13 < |I_{\rm dc}| < 17$ mA. Depending on the bias conditions, we observe that the effective quality factor of the auto-oscillation signal, defined as the ratio of emission frequency to frequency linewidth, can reach values close to 1000. This single mode with a narrow linewidth can hence be considered as coherent [163].

We now analyze quantitatively the main features of auto-oscillations, which allows us to determine their nature. For this, we compare the auto-oscillations observed in the 4 μm and 2 μm micro-disks. Similar threshold current density in both samples of $(4.4 \pm 0.2) \cdot 10^{11}$ A.m^{-2}, in agreement with our previous study (see Fig.4.7). As the dc current is varied towards more negative values, the peaks shift towards lower frequency (Fig.4.9a), at a rate which is twice faster in the smaller disk. This frequency shift is mainly due to linear and

quadratic contributions in I_{dc} of Oersted field and Joule heating, respectively [81] (from the Pt resistance, the maximal temperature increase in both samples is estimated to be +40°C). At the same time, the signal first rapidly increases in amplitude, reaches a maximum, and then, more surprisingly, drops until it cannot be detected anymore, as seen in Fig.4.9b, which plots the integrated power *vs.* I_{dc}. The maximum of power measured in the 4 μm disk (2.9 fW) is four times larger than the one measured in the 2 μm disk (0.7 fW), which is due to the inductive origin of V_y. The latter can be estimated from geometrical considerations, and the maximal angle of precession reached by auto-oscillations is found to be about 1° in both micro-disks. Finally, the disappearance of the signal as I_{dc} gets more negative is accompanied by a continuous broadening of the linewidth, which increases from a few MHz to several tens of MHz (Fig.4.9c).

We also measure the bias field dependence of the auto-oscillations in both micro-disks. The onset frequency in both micro-disks is identical and closely follows the dispersion relation of the Kittel mode. We note that this mode is the one which couples the most efficiently to our inductive electrical detection, because it is the most uniform. Hence, we conclude that the detected auto-oscillation signal is due to the destabilisation of this mode by spin-orbit torque. The threshold current at which auto-oscillations start is plotted in Fig.4.9d. It behaves quite as expected from Eq.1.4 in the region where it linearly increases with the field (see dashed lines), at large bias. To understand its behavior at low field, one need to take into account quasi-degenerate spin-wave modes, which are responsible for the inhomogeneous contribution to the linewidth, ΔH_0, which is detected on the same samples using electrical FMR spectroscopy [30]. These quasi-degenerate SW modes strongly affect the exact value and detailed dependence *vs.* H of the threshold current, as seen from the comparison between continuous and dashed lines in Fig.4.9d. In fact, it is the total linewidth that truly quantifies the losses of a magnetic device regardless of the nature and number of microscopic mechanisms involved. Even in structures with micron-sized lateral dimensions, there still exist a few quasi-degenerate spin-wave modes. Due to magnon-magnon scattering, they are linearly coupled to the main FMR mode, which as a result has its effective damping increased, along with the threshold current. The presence of these modes is also known to play a crucial role in spin-orbit torque driven dynamics. The strongly non-equilibrium distribution of spin-waves promoted by spin-orbit torque in combination with nonlinear interactions between modes can lead to mode competition, which might even prevent auto-oscillations to start [44]. We believe that the observed behaviors of the integrated power (Fig.4.9b) and linewidth (Fig.4.9c) *vs.* I_{dc} are reminiscent of the presence of these quasi-degenerate SW modes. A meaningful interpretation of these experimental results is that as the FMR mode starts to auto-oscillate and to grow in amplitude as the dc current is increased above the threshold, its coupling to other spin-wave modes – whose amplitudes also grow due to spin-orbit torque – becomes larger, which makes the flow of energy out of the FMR mode more efficient. This reduces the inductive signal, as non-uniform SW modes are poorly coupled to our inductive detection scheme. At the same time, it enhances the auto-oscillation linewidth, which reflects this additional nonlinear relaxation channel.

To check this scenario, we have performed μ-BLS spectroscopy on samples from the same batch [42], in collaboration with the group of Sergej Demokritov (Universität Münster). When the laser spot is positioned at the center of the 2 μm YIG|Pt micro-disk, Fig.4.9e, it detects the onset of auto-oscillations at a similar current than the one measured with the inductive detection scheme. The μ-BLS technique also allows to map

the spatial profile of the magnetization dynamics, see Fig.4.9f. Interestingly, one observes that the latter quickly expands laterally to occupy all the space in between the gold electrodes contacting the YIG|Pt disk, as shown in Figs.4.9g and h. The maximum intensity of the auto-oscillations (up triangles in Fig.4.9i) saturates immediately after the onset and then stays nearly constant over the entire used range of current. In contrast, the integral intensity (down triangles in Fig.4.9i) exhibits a gradual increase up to 9.2 mA. This indicates that the amplitude of the dynamic mode excited at the onset cannot grow above a certain level and that the further increase in current results in the energy flow into other dynamical modes leading to the formation of a strongly nonlinear spatially-extended mode, which cannot be treated as a linear combination of the eigenmodes of the system [43]. These behaviors can be attributed to the efficient nonlinear mode coupling stimulated by the small dynamic damping in YIG, and nicely confirm the hypotheses made above.

Related publications

1. C. Hahn, V. V. Naletov, G. de Loubens, O. Klein, O. d'Allivy Kelly, A. Anane, R. Bernard, E. Jacquet, P. Bortolotti, V. Cros, J. L. Prieto, M. Muñoz, *Measurement of the intrinsic damping constant in individual nanodisks of $Y_3Fe_5O_{12}$ and $Y_3Fe_5O_{12}|Pt$*, Appl. Phys. Lett. **104**, 152410 (2014).

2. A. Hamadeh, O. d'Allivy Kelly, C. Hahn, H. Meley, R. Bernard, A. H. Molpeceres, V. V. Naletov, M. Viret, A. Anane, V. Cros, S. O. Demokritov, J. L. Prieto, M. Muñoz, G. de Loubens, O. Klein, *Full Control of the Spin-Wave Damping in a Magnetic Insulator Using Spin-Orbit Torque*, Phys. Rev. Lett. **113**, 197203 (2014).

3. M. Collet, X. de Milly, O. d'Allivy Kelly, V.V. Naletov, R. Bernard, P. Bortolotti, J. Ben Youssef, V.E. Demidov, S.O. Demokritov, J.L. Prieto, M. Muñoz, V. Cros, A. Anane, G. de Loubens, O. Klein, *Generation of coherent spin-wave modes in yttrium iron garnet microdiscs by spin-orbit torque*, Nature Commun.**7**, 10377 (2016).

4. V. E. Demidov, M. Evelt, V. Bessonov, S. O. Demokritov, J. L. Prieto, M. Muñoz, J. Ben Youssef, V. V. Naletov, G. de Loubens, O. Klein, M. Collet, P. Bortolotti, V. Cros, A. Anane. *Direct observation of dynamic modes excited in a magnetic insulator by pure spin current*, Sci. Rep. **6**, 32781 (2016).

5. M. Evelt, V. E. Demidov, V. Bessonov, S. O. Demokritov, J. L. Prieto, M. Munoz, J. Ben Youssef, V. V. Naletov, G. de Loubens, O. Klein, M. Collet, K. Garcia-Hernandez, P. Bortolotti, V. Cros, A. Anane. *High-efficiency control of spin-wave propagation in ultra-thin yttrium iron garnet by the spin-orbit torque*, Appl. Phys. Lett. **108**, 172406 (2016).

6. V. Demidov, S. Urazhdin, G. de Loubens, O. Klein, V. Cros, A. Anane, S. Demokritov. *Magnetization oscillations and waves driven by pure spin currents*, Physics Reports 673, 1-31 (2017).

Grégoire de Loubens

Résumé en français

Les électrons de conduction d'une couche de métal normal N sont un canal de relaxation pour l'aimantation hors équilibre d'une couche adjacente ferromagnétique F. En précessant, cette dernière émet un courant de spin à l'interface F|N : c'est le pompage de spin. Ce phénomène a été récemment démontré dans le cas où F est isolant. Grâce à l'effet Hall de spin inverse, qui convertit un courant de spin en courant de charge, nous avons détecté électriquement la composante statique du pompage de spin aux interfaces YIG|Pt et YIG|Ta, et montré que les angles de Hall dans Pt et Ta étaient de signes opposés (Fig.4.2). Nous avons aussi mesuré la magnétorésistance spin Hall qui résulte du couple de transfert de spin à l'interface YIG|N entre les électrons polarisés de N et l'aimantation du YIG et de l'effet Hall de spin (Fig.4.4). De plus, en excitant paramétriquement des ondes de spin dans YIG|Pt, nous sommes parvenus à détecter la composante dynamique du pompage de spin (Fig.4.3). En outre, nous avons étudié la transmission du courant de spin à travers un antiferromagnétique isolant (NiO), intercalé entre le YIG et le Pt (Fig.4.5), et montré que NiO était un bon conducteur pour le moment angulaire.

Nous avons également étudié les spectres d'ondes de spin de nano-disques fabriqués à partir de couches ultra-minces de YIG (20 nm) d'excellente qualité produites par ablation laser pulsé (Fig.4.6). L'amortissement mesuré par MRFM dans ces nanostructures n'est pas affecté par la nanofabrication, et la différence de largeur de raie observée entre les nano-disques de YIG et ceux de YIG|Pt permet d'extraire la conductance spin mixing de l'interface YIG|Pt. En mesurant la variation de largeur de raie d'un micro-disque de YIG|Pt en fonction du courant dc circulant dans le Pt, nous avons déterminé la densité de courant nécessaire pour compenser totalement l'amortissement du YIG (Fig.4.7). La valeur trouvée de quelques 10^{11} A/m^2 est en accord avec les attentes. Pour le confirmer, nous avons directement détecté les auto-oscillations d'un micro-disque de YIG|Pt au-dessus du courant critique. La symétrie observée en fonction des polarités du champ et du courant appliqué confirme que l'origine de la dynamique est le couple spin-orbite généré à l'interface YIG|Pt (Fig.4.8). Ces expériences indiquent également que les modes d'ondes de spin quasi-dégénérés avec le mode uniforme augmentent le courant critique et limitent l'amplitude et la cohérence spatiale de ces oscillations à cause d'effets non-linéaires. Ces résultats ont été confirmés par des études en microscopie Brillouin permettant d'imager directement le profil spatial des auto-oscillations (Fig.4.9).

Chapter 5

Current projects and perspectives

The research topics developed in the three previous chapters have some perspectives in the short- and mid-term, which I would like to develop in the framework of collaborative projects. In the following sections, I am presenting their main lines, together with some preliminary data when available.

Although I will not develop at all this project here, I would like to emphasize that the detection of magnetization dynamics at the local scale using magnetoresistive sensors is a very efficient and well integrated alternative to MRFM. A main advantage of this type of sensors is that they are directly sensitive to the magnetic *field*, which, as the size of the sample is decreased, scales much more favorably than the magnetic flux whose time derivative is sensed by traditional inductive methods. My colleagues Claude Fermon, Myriam Pannetier-Lecoeur and Aurélie Solignac are experts on this topic of field sensing, and some preliminary promising studies of detecting magnetic field in the microwave range with spin-valve elements have been carried out in the past [16].

5.1 Individual nano-objects

A natural perspective of the results on the dynamics in individual vortex-state nanodots presented in chapter 2 is to use the MRFM technique to perform the spectroscopy and to probe the nonlinear dynamics of other non-trivial spin textures in magnetic nano-objects, as described below.

5.1.1 Magnetic skyrmions

Magnetic skyrmions are topological singularities appearing in magnetic materials with strong Dzyaloshinskii-Moriya interaction (DMI), which favors non-collinear configurations of the magnetization. These topological objects are interesting candidates for information storage and processing, as they are naturally coupled to spintronics [157]. Nevertheless, their stability and dynamics still have to be investigated. Recently it has been demonstrated that such structures having typical size of a few tens of nanometers could be stabilized at room temperature in nanodisks patterned from multilayers with strong DMI [130]. Their excitation spectrum has also been calculated [100, 56, 70, 132], but so far never measured. In particular, specific modes such as the breathing modes, which can be excited with an out-of-plane microwave field [100], and gyrotropic skyrmion modes [70] have been predicted.

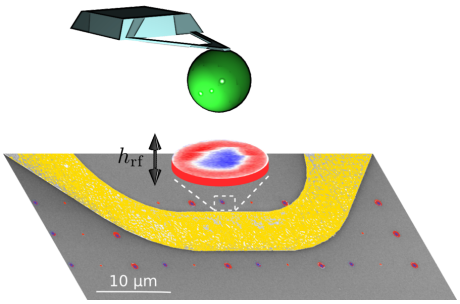

Figure 5.1: ***Planned MRFM experiment on skyrmions.*** *The sample consists of different dots of sub-micron diameters patterned from a Pt10|(Co0.8|Ir1|Pt1)$_{10}$|Pt3 multilayer, where thicknesses are given in nm. The broadband microwave antenna allows to apply in-plane and out-of-plane rf fields to excite different dynamic modes.*

The goal of this project is to perform the MRFM spectroscopy of an individual nano-disk in the spatially uniform and skyrmion states in order to identify the spin-wave modes and the relaxation mechanisms. In particular, it would be interesting to study how the spin-wave modes transform at the transition between the uniform and skyrmion states [132], in a similar way we did for the vortex cone state [175] (see section 2.1.2).

For this, I am collaborating with Vincent Cros' team (UMR CNRS/Thales), in particular in the framework of an ANR project just funded on the topic. As a preliminary work, some samples adapted to the MRFM experiment have been nanofabricated (see Fig.5.1). They consist of nano-disks made of Pt|Co|Ir multilayers with strong out-of-plane anisotropy and sizeable DMI, with a microwave antenna integrated on top to provide in-plane and out-of-plane microwave field excitations. In a first stage, we have used the MRFM setup to perform cantilever magnetometry of such nano-disks. Similarly to the data shown in Fig.2.2a, the cantilever frequency is recorded as a function of perpendicular field, which allows us to extract the hysteresis loop of the nano-disk placed underneath the MRFM probe. When the bias perpendicular field is scanned, magnetization reversal occurs in the nano-disk through several sharp magnetization steps, whose number decreases with the diameter of the nano-disk. Moreover, standard MFM imaging confirms that a single skyrmion can be stabilized in nano-disks with diameter below 500 nm. The next stage is to measure the magnetization dynamics in these samples under microwave irradiation.

5.1.2 Magnetic nanoparticles

Magnetic nanospheres are expected to exhibit interesting high-frequency dynamics due to non-uniform equilibrium states at low field, arising from the competition between exchange and dipolar interactions. Among them, topological singularities such as a vortex [102], a Bloch point [149], or even a skyrmion [92], are very attractive. The interest of these singularities is both fundamental, since they are recognized as key for understanding the behavior of a wide variety of condensed matter systems, and applicative, since they can be considered as elementary entities for information recording. On a more practical point of view for my research activities, this type of object is also an ideal magnetic probe for MRFM.

In all the MRFM studies presented in this manuscript, the probe attached to the very

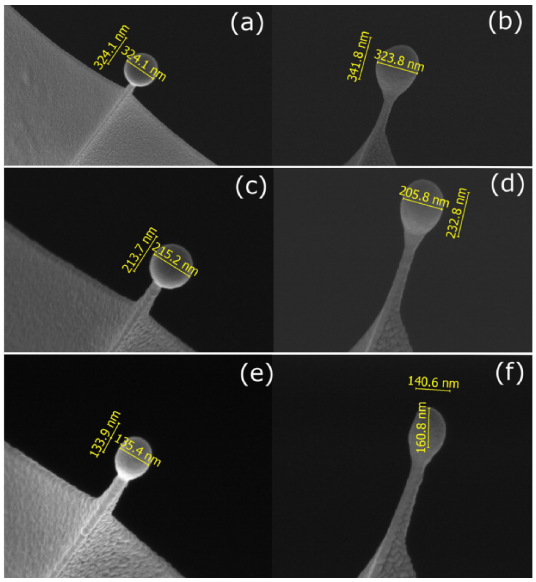

Figure 5.2: ***Cobalt nanospheres grown by focused electron beam induced deposition.*** *SEM micrographs showing the dimensions of the grown cobalt nanospheres at the tip of MRFM cantilevers. Top view and front view of cobalt nanospheres of 325 nm (a, b), 215 nm (c, d) and 135 nm (e, f) in diameter.*

soft cantilever is a soft Fe (with 3% Si) nanosphere of diameter 700 to 800 nm, which is well adapted to perform sensitive MRFM spectroscopy of samples with lateral size larger than 100 nm in the weak coupling geometry (*i.e.*, a probe-sample separation larger than 1 μm). If one would like to study sub-100 nm lateral size samples, or gain spatial resolution, one would need much smaller MRFM probes. There are, however, few methods for the synthesis of nanomagnets in the 10 nm – 300 nm range. In that context, the possibility of growing high-quality cobalt nanoparticles by focused-electron-beam-induced deposition (FEBID) [187, 10] opens an interesting new route to attaching in-situ nanosize magnets at the tip of cantilevers. This technique directly uses the electron beam of a scanning electron microscope to decompose a precursor gas, which enables to grow three dimensional nanomagnets [52], similarly to 3D-printing. Hence, no micromanipulation is required in that case to position the nanomagnet at the apex of the cantilever beam.

For a few years, I have started a collaboration with the team of José María de Teresa (Universidad de Zaragoza), and in particular with Soraya Sangiao. Using FEBID, cobalt magnetic nanospheres with diameter ranging between 100 nm and 300 nm have first been grown at the tip of our ultra-soft MRFM cantilevers, see Fig.5.2. By monitoring the mechanical resonance frequency of the cantilever as a function of the applied magnetic field [168], the hysteresis curve of these individual nanospheres have been measured. This enabled to evaluate their saturation magnetization, found to be around 4.3 10^5 A/m independently of the size of the particle [109]. More recently, the growth conditions have been optimized: nanospheres with diameter in the 300 nm – 500 nm range have a Co content above 90%, and a magnetization close to bulk cobalt. The latter decreases with the size of the nanospheres, but is still around 10^6 A/m for 200 nm diameter, which is a good compromise between spatial resolution and sensitivity for MRFM application. Moreover, electron holography measurements show the formation of a magnetic vortex state in remanence, which nicely agrees with magnetic hysteresis loops performed by can-

tilever magnetometry showing negligible remanent magnetization for these soft magnetic nanospheres [159].

Now the objective is to use such magnetic nanospheres in MRFM studies requiring smaller and more sensitive probes, *e.g.*, the study of individual skyrmions mentioned above. It would also be interesting to probe the magnetization dynamics of the nanospheres themselves by MRFM, in particular in the vortex state. A longer term project would be to use 100 nm cobalt nanospheres as MRFM probe to study magnetization dynamics in individual nanoparticles of truly nanometer size (< 20 nm) in our variable temperature (4 K – 300 K) and large magnetic field (up to 7 T) microscope. Despite some pioneering studies of microwave assisted magnetization reversal using micro-SQUID magnetometry [179], there are almost no spectroscopic studies of the magnetization dynamics and of its relaxation close to equilibrium in these systems, which are at the transition between quantum dynamics (several interacting spins) and classical thermodynamics (many-body behavior) [137, 55].

Related publications

1. H. Lavenant, V. Naletov, O. Klein, G. de Loubens, L. Casado, J. M. de Teresa, *Mechanical magnetometry of Cobalt nanospheres deposited by focused electron beam at the tip of ultrasoft cantilevers*, Nanofabrication **1**, 65-73 (2014).

2. S. Sangiao, C. Magén, D. Mofakhami, G. de Loubens and J. M. de Teresa, *Magnetic properties of optimized cobalt nanospheres grown by Focused Electron Beam Induced Deposition (FEBID) on cantilever tips*, Beilstein J. Nanotechnol. **8**, 2106-2115 (2017).

5.2 Nonlinear effects

Nonlinearities have important implications in magnetization dynamics of nanostructures, as illustrated in spin torque nano-oscillators (chapter 3), where large precession angles can be achieved, and in spin-orbit torque YIG-based oscillators (chapter 4), where nonlinear interactions between spin-wave modes play a crucial role above the threshold. In this section, I am describing two ongoing projects related to nonlinear effects in nanostructures. In the first one, we would like to take advantage of a sample integrating a microwave antenna on top of high dynamical quality YIG nano-disks to study a regime of highly nonlinear FMR never achieved so far. In the second one, we study a generic mechanism of destruction of the mutual synchronization between nonlinear oscillators.

5.2.1 Deeply nonlinear magnetization dynamics in YIG nano-disks

In extended ferromagnetic samples, it is well known that spin-wave instabilities quickly develop as the excitation power is increased, preventing to achieve very large angle of uniform precession [170] (see section 1.1). The situation is expected to be quite different in nanostructures, where spin-wave modes are highly quantized due to the geometric confinement [105, 125]. To study the highly nonlinear magnetization dynamics forced by a harmonic excitation, it is for instance possible to perform spin-torque driven FMR in metallic spin-valve nanopillars, where large foldover shifts were observed thanks to the

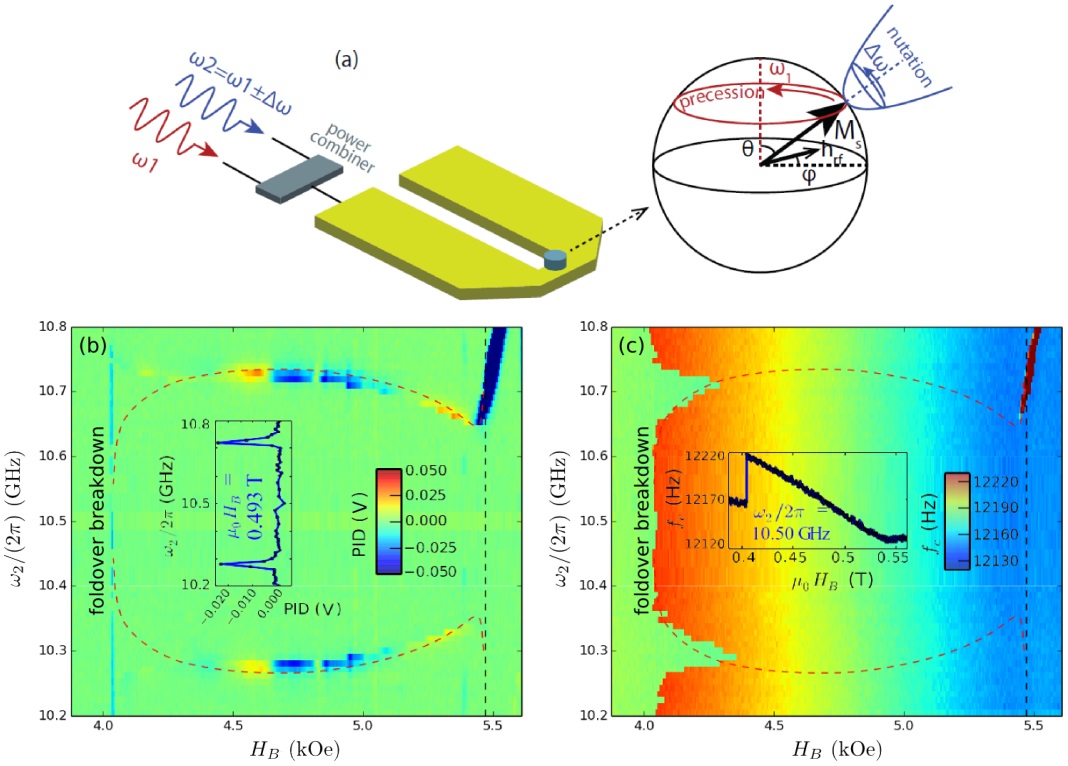

Figure 5.3: ***MRFM spectroscopy of spin-wave instabilities in a YIG nano-disk.*** *(a) The YIG nano-disk is subjected to two microwave signals: a first one, continuous wave, at 10.5 GHz and large power (+2 dBm) to excite the large amplitude foldover state (red), and a second one, modulated at the cantilever frequency, of varying frequency (10.2 GHz – 10.8 GHz) and low power (−24 dBm), to sensitively probe the spin-waves on top (blue). (b-c) Color maps of the MRFM spectroscopy signal (b) and of the cantilever frequency shift (c) recorded simultaneously as a function of bias perpendicular field and frequency of the low power microwave signal. Insets in (b) and (c) show cuts of the data at specific field and specific frequency, respectively. The dashed curves are calculated using Eq.(5.1).*

high efficiency of the excitation scheme [24]. There are also a few experimental reports on the FMR driven highly nonlinear regime in micron-size Permalloy samples, which demonstrate large foldover states [62] and nonlinear hybridization of spin-wave modes [41].

Because of its very low damping, YIG has been for a long time a material of choice to study magnetization dynamics of macroscopic samples in the highly nonlinear regime [198]. Now, we have access to YIG nanostructures of high dynamical quality, such as the nano-disks whose spin-wave spectra are presented in Fig.4.6. These bare YIG nano-disks have a damping below 5 10^{-4}. Moreover, thanks to the micro-antenna patterned above them, the amplitude of the microwave field can be increased up to a few mT in a broad frequency range (up to 20 GHz), enabling us to investigate the deeply nonlinear regime of FMR. Using the MRFM technique, it is possible to measure the out-of-plane FMR in the regime where the reduction of the longitudinal component is such that it induces an important shift of the resonance field, which leads to the foldover effect. For this, we monitor the cantilever frequency under continuous wave (cw) irradiation of the sample, which is required to explore the full extension of foldover, due to the latter being hysteretic on the swept parameter (field or frequency). Preliminary experiments on

the 700 nm nano-disk show that ultra-large amplitude precession with almost complete suppression of the longitudinal component can be achieved by pumping the sample with the uniform microwave field.

Two types of studies have been planned. Firstly, we want to follow thoroughly the evolution of the resonance curves as a function of the excitation power, in order to identify experimental signatures of the nonlinear coupling between quantized spin-wave modes. Strikingly, preliminary data show that the foldover shift is not constantly growing as the power is increased, but instead presents plateaus, pointing towards nonlinear energy dissipation to quantized spin-wave modes. Micromagnetic simulations have been launched and more experimental data on smaller diameter samples are planned to confirm this picture. Secondly, we want to probe the stability of the highly nonlinear dynamics excited by the large micowave field at the pumping frequency, in order to unveil the excitation spectrum which has been calculated in the rotating frame of the magnetization vector [13], but never measured so far. As a matter of fact, when adding a much weaker rf field of varying frequency using a power combiner (Fig.5.3a), two resonance peaks symmetrically distributed around the main frequency are observed in the foldover region of Fig.5.3b, which correspond to a nutation of the magnetization vector on top of the large angle coherent dynamics excited by the strong cw rf field. These two resonances coincide well with the theoretical prediction of the nutation frequency, which was shown to have a similar form as the Rabi formula, generalized to take into account nonlinearities [13]:

$$\frac{\omega_n^2}{\gamma^2} = \frac{\mu_0 h_{\mathrm{rf}} \cos\phi}{\sin\theta}\left(\frac{\mu_0 h_{\mathrm{rf}} \cos\phi}{\sin\theta} + \mu_0 M_s \sin^2\theta\right) , \tag{5.1}$$

where the polar angles θ and ϕ are defined in Fig.5.3a. When excited above a certain threshold, the nutation destabilizes the foldover, as evidenced by the resonant reduction of the foldover field shift around 10.3 GHz and 10.7 GHz in Fig.5.3c. Higher order nutation modes are also being currently studied, both experimentally and using micromagnetic simulations.

5.2.2 Resonant destruction of synchronization of nonlinear oscillators

Synchronization of self-sustained oscillators is a generic phenomenon, which is widely studied in nonlinear sciences due to its importance in domains spanning from engineering to medicine [147]. General theoretical frameworks, such as the famous one introduced by Kuramoto [2], have been developed and are able to successfully capture many features observed in real systems that can be modelled using interacting oscillators. Still, there is a variety of phenomena which remain to be explored in this vast field of research, where a current trend is to propose new directions in which multidisciplinarity is key, such as bio-inspired computing [61].

Among these phenomena, qualitative consequences of the oscillators' nonlinearities on their collective dynamics have been recently predicted [181, 182]. On one side, the sensitivity of nonlinear auto-oscillators to external signals is exacerbated, which can be used to increase the stability of phase-locking [182]. On the other side, the existence of an intrinsic nonlinear phase shift in the mutual couplings can lead to frustration [181] and to unusual transitions to synchronization [140].

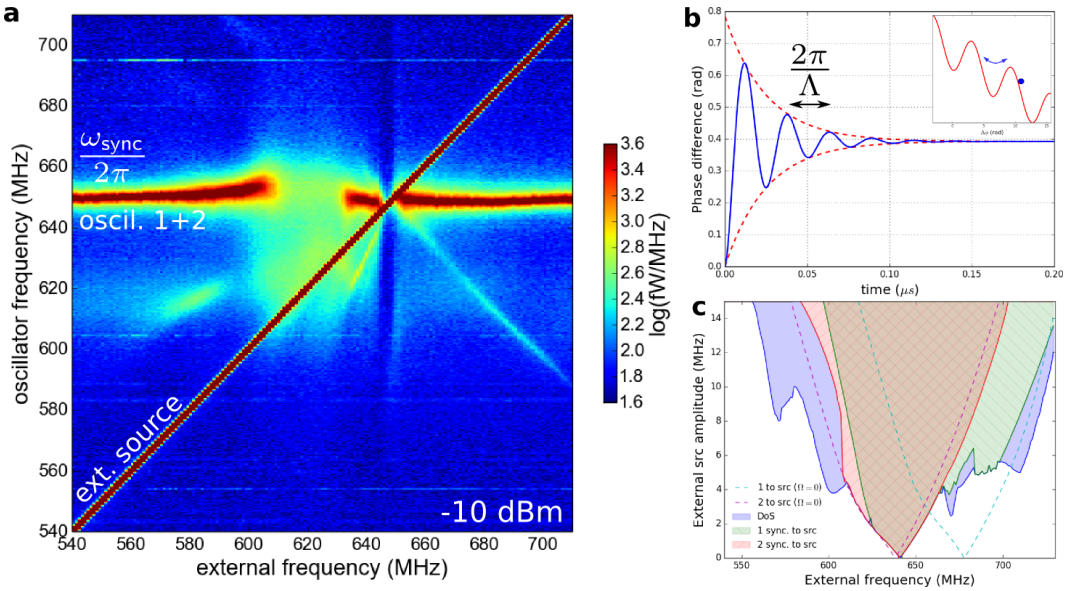

Figure 5.4: ***Resonant destruction of synchronization.*** *(a) PSD map of the mutually synchronized oscillators (in a similar state as in Fig.3.13c) measured as a function of the frequency of the external source. (b) Relaxation of the oscillators' phase difference $\Delta\phi$ after an initial perturbation from the synchronized state, revealing the intrinsic oscillation frequency Λ. The inset shows the effective potential created by the mutual interaction on $\Delta\phi$. (c) Dynamical state of the coupled oscillators' system as a function of frequency and amplitude of the external signal, determined using numerical simulations.*

There are very few studies of small size systems with only a few mutually coupled nonlinear oscillators and one external source, although they are already non trivial. It is thus very interesting to investigate the consequences of the oscillators nonlinearities in a system of two STNOs in mutual interaction plus an external source, which can display very rich dynamics. This study has been initiated by a collaborative ANR project with Julie Grollier (UMR CNRS/Thales), whose goal is to investigate the opportunities of coupled STNOs networks to design associative memories, which are inspired by the brain and allow information to be reconstructed from noisy or incomplete data. This project also benefits from the very valuable theoretical support of Vasyl Tiberkevich (Oakland University).

Our main result so far on this topic is presented in Fig.5.4, which demonstrates that the synchronized state of coupled STNOs can be destroyed by a weak external signal tuned around the intrinsic frequency of phase oscillations. The system under investigation is the two STVOs mutually synchronized by the dipolar interaction presented in Fig.3.13. We perform a similar experiment to that presented in Fig.3.14, where we scan the external source frequency in the vincinity of the oscillators' frequency, except that this time we do it at a working point where the two oscillators are mutually synchronized. The major experimental observation in Fig.5.4a is the fact that the system is the most affected by the external source at a frequency of about 620 MHz, which is quite lower than the synchronous frequency of oscillators (around 650 MHz). In fact, the synchronous signal disappears and instead, a spreading of the auto-oscillating signal in the frequency domain occurs.

The explanation of this phenomenon lies in the existence of intrinsic phase oscillations

in a system of mutually synchronized nonlinear oscillators, which are shown in Fig.5.4b. We note that such phase oscillations in a system of two mutually synchronized STVOs were already observed in numerical simulations [9]. The mutual phase-locking creates an effective potential well for the oscillators' phase difference (inset of Fig.5.4b), and since the oscillators are nonlinear, *i.e.*, have an inertia, this system is analogous to a massive particle in a potential well, which can be resonantly excited by a weak external force and kicked out from its stable point. With simplifying assumptions, and considering the oscillators as quasi-identical, the frequency of intrinsic phase oscillations can be estimated analytically: $\Lambda \simeq 2\sqrt{\Gamma_p \Omega \nu}$, where ν and Γ_p are respectively the dimensionless nonlinear parameter of the STNOs and the relaxation rate of amplitude fluctuations [163], and Ω the strength of the mutual dipolar interaction. The damping rate of these phase oscillations is governed by Γ_p.

Using numerical simulations, it is also possible to calculate the time evolution of the oscillator's phase difference when the system is affected by the external source of varying frequency and amplitude, and to build the stability diagram of the system, see Fig.5.4c. Regions of destruction of the synchronization (DoS), where none of the oscillators is synchronized to the source, but not mutually synchronized anymore either, are shown in blue on this diagram (the white region corresponds to the oscillators being synchronized to each other). Interestingly, the simulations also suggest that the system becomes chaotic in these DoS regions.

From a fundamental point of view, our findings thus reveal a specific mechanism of coupled nonlinear systems, namely, the resonant destruction of synchronization by a weak external signal. It could be used in practice as a way to selectively destroy undesirable synchronized states, which may be important for oscillator-based neuromorphic computing [136, 61, 190].

Related publications

1. G. Melkov, D. Slobodianiuk, V. Tiberkevich, G. de Loubens, O. Klein, A. Slavin, *Nonlinear Ferromagnetic Resonance in Nanostructures Having Discrete Spectrum of Spin-Wave Modes*, Magnetics Letters **4**, 4000504 (2013).

5.3 Transport of spin angular momentum in magnetic insulators

The demonstration that electrical signals could be transmitted by spin-wave interconversion in a magnetic insulator has been a breakthrough [94], which motivated us to work mainly on the possibilities to control the magnetic relaxation in YIG by the spin-orbit torque (chapter 4). Simultaneously, there have also been a lot of studies on the spin Seebeck effect in magnetic insulators [185], and heat driven dynamics has been recently demonstrated in a YIG based "spin caloritronic" oscillator [156]. It has even been proposed that spin transport at an insulator/metal interface could trigger the condensation magnons in the magnetic insulator [11]. Although this has not been observed experimentally yet, control and local measurement using diamond nitrogen-vacancy centers of the spin chemical potential in a magnetic insulator has recently been reported [47], and

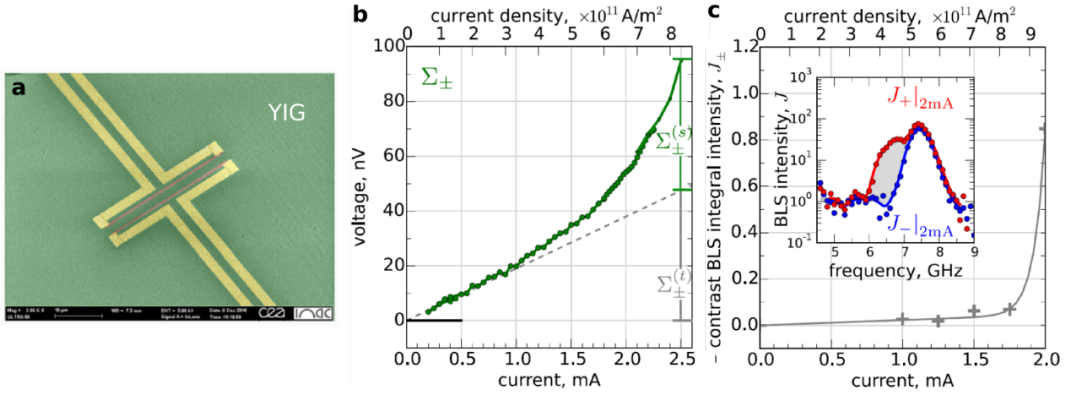

Figure 5.5: ***Non-local spin conduction in the nonlinear regime.*** *(a) SEM picture of the device, with two Pt stripes separated by* 1.2 *µm (red) patterned on top of a 18 nm thick YIG film (green) and contacted by gold electrodes (yellow). (b) Spin-orbit torque contribution of the non-local voltage detected on the Pt detector electrode as a function of the current sent through the Pt injector electrode. (c) µ-BLS integrated intensity measured at the detector under the same conditions, in a similar sample. The inset shows the spectral distributions of the magnons measured by BLS at* ±2 *mA.*

a general phenomenology describing the interplay between coherent and incoherent dynamics in ferromagnetic insulators has been introduced [54]. All this constitutes a very active field of research, on which we will continue to collaborate with my colleagues Michel Viret (SPEC), Olivier Klein and Laurent Vila (Spintec), Jamal Ben Youssef (UBO/Lab-STICC), Madjid Anane and Vincent Cros (CNRS/Thales) and Vladislav Demidov and Sergej Demokritov (Universität Münster).

Our latest results on this topic have been obtained in studying the spin conductance of YIG ultra-thin films driven by large spin-orbit torque, and are summarized in Fig.5.5. Magnons are generated and detected by direct and inverse spin Hall effects in a non-local geometry, with two Pt wires deposited on top of a 18 nm thick extended YIG film (see SEM picture in Fig.5.5a). We confirm that at low current (linear response) the spin conductance is dominated by transport of thermal exchange magnons (see linear dependence of the non-local voltage in Fig.5.5b), as it was first demonstrated in ref. [32]. Above an electrical current density in the Pt of about 5 10^{11} A/m^2, the non-local signal clearly deviates from a linear behavior. In this regime, the spin transfer torque is sufficient to compensate the dissipation of long wavelength spin-wave modes, as we demonstrated on micro-disks in section 4.2 [30]. The spin conductance is thus dominated by these magnetostatic magnons, which are low-damping non-equilibrium magnons thermalized near the spectral bottom by magnon-magnon interaction, and becomes sensitive to the strength of the applied magnetic field. This picture is supported by μ-BLS spectroscopy, as shown in Fig.5.5c.

There are many other research directions which could be explored to progress on this topic. It is known for a long time that magneto-elastic coupling in YIG gives rise to a variety of phenomena [64], but the contribution of phonons in the transport of angular momentum in magnetic insulators still has to be elucidated. In passing, I would like to emphasize that spin-phonon coupling is a very relevant issue, as a universal mechanism of spin relaxation in solids does exist [27]. It turns out that during my postdoc at NYU with Andy Kent, I did measure the relaxation rate in single molecule magnets at microwave

frequencies and collaborated with Dmitri Garanin (CUNY) to compare my experimental results with detailed calculations of the relaxation rate using the universal density matrix equation [36]. Of course, the situation of magnon-phonon coupling in YIG is much more complex, in particular due to the intricate excitation spectrum of this ferrimagnetic material, which extends up to the terahertz region [8], and due to the strong thermal gradients that can exist when injecting large current densities in adjacent Pt [156]. Moreover, for ultra-thin YIG films, the role of the thick GGG substrate, which can also support the transport of phonons, is certainly not negligible.

Another very important class of magnetic insulators are antiferromagnets, in which spin currents can also be transmitted, as shown in section 4.1.2. Antiferromagnetic dynamics naturally occurs in the terahertz range [103, 97], and the possibility of generating THz oscillations through spin transfer torque at the interface between a strong spin-orbit metal such as Pt and an insulating antiferromagnet such as NiO has been recently suggested [26, 99]. My colleagues Jean-Yves Chauleau and Michel Viret have recently developed a nonlinear optics technique based on imaging the second harmonic light generated by magnetic orders. The experiment based on femtosecond light pulses has state-of-the-art sub-micron resolution and allowed them to follow the evolution of antiferromagnetic domains under the application of some external fields [22]. This provides an essential tool for pursuing investigations on how to best control antiferromagnetic domains and eventually to trigger and use antiferromagnetic spin-waves in THz devices, in particular by interfacing them with spintronics.

Résumé en français

Les axes de recherche développés plus haut ont des perspectives à court ou moyen terme, que je souhaite développer sous forme de projets collaboratifs.

L'étude de la dynamique de l'aimantation dans des nano-objets individuels par MRFM, en particulier celle de skyrmions. Le but de ce projet est de réaliser la spectroscopie MRFM de nano-disques, fabriqués à partir de multicouches présentant une forte interaction Dzyaloshinskii-Moriya, dans les états uniformes et skyrmion, afin d'identifier les modes d'ondes de spin et les mécanismes de relaxation (Fig.5.1). D'autre part, des nanosphères de cobalt peuvent être élaborées in situ dans un microscope électronique à balayage à l'extrémité des leviers mécaniques très souples (collaboration avec Saragosse, Fig.5.2). Ces particules sont intéressantes en tant qu'objets d'étude, car elles peuvent présenter des états de configurations d'équilibre non triviales (vortex), et leurs dimensions nanométriques et propriétés magnétiques font d'elles des sondes idéales pour des études MRFM de nano-objets de taille inférieure à la centaine de nanomètres.

L'investigation d'effets non-linéaires spécifiques, soit dans les systèmes fortement confinés, soit dans des systèmes d'oscillateurs à transfert de spin mutuellement couplés.

- En utilisant la technique MRFM, il est possible de mesurer la résonance ferromagnétique dans le régime fortement non-linéaire d'un nano-disque de YIG unique, où la réduction d'aimantation longitudinale est telle qu'elle induit un décalage important du champ de résonance et conduit au repliement de la courbe de résonance. Les études des signatures expérimentales des couplages non-linéaires entre ondes de spin quantifiées dans ce régime et de la stabilité de la dynamique dans le référentiel tournant de l'aimantation sont en cours (Fig.5.3).

- Nous étudions également le mécanisme générique de destruction résonante de la synchronisation de deux STNOs par un signal externe de faible amplitude, expérimentalement et numériquement (Fig.5.4). Son origine provient des propriétés non-linéaires intrinsèques des oscillateurs, et de leur couplage mutuel. Il pourrait aboutir à une dynamique chaotique, et permettre de contrôler sélectivement la synchronisation de clusters dans des architectures neuromorphiques à base d'oscillateurs couplés.

Le transport de moment angulaire dans des isolants magnétiques. Actuellement, nous nous intéressons au transport de moment angulaire dans des films ultra-minces de YIG, où les interactions entre les nombreux modes de magnons pouvant être excités par un courant de spin, dont les énergies s'étendent du GHz (modes magnétostatiques) au THz (modes d'échange), jouent un rôle crucial (Fig.5.5). D'autre part, il est possible de transmettre des courants de spin à travers des antiferromagnétiques isolants, ce qui ouvre des perspectives intéressantes pour interfacer ces matériaux avec l'électronique de spin, de la même façon qu'il est possible de le faire pour le YIG.

Bibliography

[1] F. Abreu Araujo, A. D. Belanovsky, P. N. Skirdkov, K. A. Zvezdin, A. K. Zvezdin, N. Locatelli, R. Lebrun, J. Grollier, V. Cros, G. de Loubens, and O. Klein, *Optimizing magnetodipolar interactions for synchronizing vortex based spin-torque nano-oscillators*, Phys. Rev. B, 92 (2015), p. 045419.

[2] J. A. Acebrón, L. L. Bonilla, C. J. Pérez Vicente, F. Ritort, and R. Spigler, *The kuramoto model: A simple paradigm for synchronization phenomena*, Rev. Mod. Phys., 77 (2005), pp. 137–185.

[3] P. W. Anderson and H. Suhl, *Instability in the motion of ferromagnets at high microwave power levels*, Phys. Rev., 100 (1955), p. 1788.

[4] R. Arias and D. L. Mills, *Extrinsic contributions to the ferromagnetic resonance response of ultrathin films*, Phys. Rev. B, 60 (1999), pp. 7395–7409.

[5] L. V. Asryan and R. A. Suris, *Inhomogeneous line broadening and the threshold current density of a semiconductor quantum dot laser*, Semiconductor Science and Technology, 11 (1996), pp. 554–567.

[6] A. A. Awad, K. Y. Guslienko, J. F. Sierra, G. N. Kakazei, V. Metlushko, and F. G. Aliev, *Precise probing spin wave mode frequencies in the vortex state of circular magnetic dots*, Appl. Phys. Lett., 96 (2010), p. 012503.

[7] M. Bailleul, R. Hollinger, and C. Fermon, *Microwave spectrum of square Permalloy dots: Quasisaturated state*, Phys. Rev. B, 73 (2006), p. 104424.

[8] J. Barker and G. E. W. Bauer, *Thermal spin dynamics of yttrium iron garnet*, Phys. Rev. Lett., 117 (2016), p. 217201.

[9] A. D. Belanovsky, N. Locatelli, P. N. Skirdkov, F. A. Araujo, J. Grollier, K. A. Zvezdin, V. Cros, and A. K. Zvezdin, *Phase locking dynamics of dipolarly coupled vortex-based spin transfer oscillators*, Phys. Rev. B, 85 (2012), p. 100409.

[10] L. M. Belova, O. Hellwig, E. Dobisz, and E. Dan Dahlberg, *Rapid preparation of electron beam induced deposition co magnetic force microscopy tips with 10 nm spatial resolution*, Rev. Sci. Instrum., 83 (2012), p. 093711.

[11] S. A. Bender, R. A. Duine, A. Brataas, and Y. Tserkovnyak, *Dynamic phase diagram of dc-pumped magnon condensates*, Phys. Rev. B, 90 (2014), p. 094409.

[12] L. Berger, *Emission of spin waves by a magnetic multilayer traversed by a current*, Phys. Rev. B, 54 (1996), pp. 9353–9358.

[13] G. Bertotti, I. D. Mayergoyz, and C. Serpico, *Spin-wave instabilities in large-scale nonlinear magnetization dynamics*, Phys. Rev. Lett., 87 (2001), p. 217203.

[14] G. Bertotti, C. Serpico, and I. D. Mayergoyz, *Nonlinear magnetization dynamics under circularly polarized field*, Phys. Rev. Lett., 86 (2001), pp. 724–727.

[15] G. Bertotti, C. Serpico, I. D. Mayergoyz, A. Magni, M. d'Aquino, and R. Bonin, *Magnetization switching and microwave oscillations in nanomagnets driven by spin-polarized currents*, Phys. Rev. Lett., 94 (2005), p. 127206.

[16] N. Biziere and C. Fermon, *High-frequency giant magnetoresistance measurement to study the dynamics of a micron-scale spin-valve sensor*, Phys. Rev. B, 78 (2008), p. 064408.

[17] F. Boust and N. Vukadinovic, *Micromagnetic simulations of vortex-state excitations in soft magnetic nanostructures*, Phys. Rev. B, 70 (2004), p. 172408.

[18] M. Buess, R. Höllinger, T. Haug, K. Perzlmaier, U. Krey, D. Pescia, M. R. Scheinfein, D. Weiss, and C. H. Back, *Fourier transform imaging of spin vortex eigenmodes*, Phys. Rev. Lett., 93 (2004), p. 077207.

[19] J. A. J. Burgess, A. E. Fraser, F. F. Sani, D. Vick, B. D. Hauer, J. P. Davis, and M. R. Freeman, *Quantitative magneto-mechanical detection and control of the barkhausen effect*, Science, 339 (2013), p. 1051.

[20] V. Castel, J. Ben Youssef, F. Boust, R. Weil, B. Pigeau, G. de Loubens, V. V. Naletov, O. Klein, and N. Vukadinovic, *Perpendicular ferromagnetic resonance in soft cylindrical elements: Vortex and saturated states*, Phys. Rev. B, 85 (2012), p. 184419.

[21] V. Castel, N. Vlietstra, J. Ben Youssef, and B. J. van Wees, *Platinum thickness dependence of the inverse spin-hall voltage from spin pumping in a hybrid yttrium iron garnet/platinum system*, Appl. Phys. Lett., 101 (2012), p. 132414.

[22] J.-Y. Chauleau, E. Haltz, C. Carrétéro, S. Fusil, and M. Viret, *Multi-stimuli manipulation of antiferromagnetic domains assessed by second-harmonic imaging*, Nature Materials, 16 (2017), pp. 803–807.

[23] W. Chen, J.-M. L. Beaujour, G. de Loubens, A. D. Kent, and J. Z. Sun, *Spin-torque driven ferromagnetic resonance of co/ni synthetic layers in spin valves*, Applied Physics Letters, 92 (2008), p. 012507.

[24] W. Chen, G. de Loubens, J.-M. L. Beaujour, J. Z. Sun, and A. D. Kent, *Spin-torque driven ferromagnetic resonance in a nonlinear regime*, Appl. Phys. Lett., 95 (2009), p. 172513.

[25] Y.-T. Chen, S. Takahashi, H. Nakayama, M. Althammer, S. T. B. Goennenwein, E. Saitoh, and G. E. W. Bauer, *Theory of spin Hall magnetoresistance*, Phys. Rev. B, 87 (2013), p. 144411.

[26] R. Cheng, D. Xiao, and A. Brataas, *Terahertz antiferromagnetic spin hall nano-oscillator*, Phys. Rev. Lett., 116 (2016), p. 207603.

[27] E. M. Chudnovsky, D. A. Garanin, and R. Schilling, *Universal mechanism of spin relaxation in solids*, Phys. Rev. B, 72 (2005), p. 094426.

[28] A. V. Chumak, A. A. Serga, M. B. Jungfleisch, R. Neb, D. A. Bozhko, V. S. Tiberkevich, and B. Hillebrands, *Direct detection of magnon spin transport by the inverse spin hall effect*, Appl. Phys. Lett., 100 (2012), p. 082405.

[29] A. V. Chumak, V. I. Vasyuchka, A. A. Serga, and B. Hillebrands, *Magnon spintronics*, Nature Physics, 11 (2015), pp. 453–461.

[30] M. Collet, X. de Milly, O. d'Allivy Kelly, V. Naletov, R. Bernard, P. Bortolotti, J. B. Youssef, V. Demidov, S. Demokritov, J. Prieto, M. Muñoz, V. Cros, A. Anane, G. de Loubens, and O. Klein, *Generation of coherent spin-wave modes in yttrium iron garnet microdiscs by spin-orbit torque*, Nature Communications, 7 (2016), p. 10377.

[31] R. L. Compton and P. A. Crowell, *Dynamics of a pinned magnetic vortex*, Phys. Rev. Lett., 97 (2006), p. 137202.

[32] L. J. Cornelissen, J. Liu, R. A. Duine, J. Ben Youssef, and B. J. van Wees, *Long-distance transport of magnon spin information in a magnetic insulator at room temperature*, Nature Physics, 11 (2015), pp. 1022–1026.

[33] R. P. Cowburn, D. K. Koltsov, A. O. Adeyeye, M. E. Welland, and D. M. Tricker, *Single-domain circular nanomagnets*, Phys. Rev. Lett., 83 (1999), pp. 1042–1045.

[34] M. Curcic, B. V. Waeyenberge, A. Vansteenkiste, M. Weigand, V. Sackmann, H. Stoll, M. Fähnle, T. Tyliszczak, G. Woltersdorf, C. H. Back, and G. Schütz, *Polarization selective magnetic vortex dynamics and core reversal in rotating magnetic fields*, Phys. Rev. Lett., 101 (2008), p. 197204.

[35] O. d'Allivy Kelly, A. Anane, R. Bernard, J. B. Youssef, C. Hahn, A. H. Molpeceres, C. Carrétéro, E. Jacquet, C. Deranlot, P. Bortolotti, R. Lebourgeois, J.-C. Mage, G. de Loubens, O. Klein, V. Cros, and A. Fert, *Inverse spin hall effect in nanometer-thick yttrium iron garnet/pt system*, Appl. Phys. Lett., 103 (2013), p. 082408.

[36] G. de Loubens, D. A. Garanin, C. C. Beedle, D. N. Hendrickson, and A. D. Kent, *Magnetization relaxation in the single-molecule magnet ni4 under continuous microwave irradiation*, EPL (Europhysics Letters), 83 (2008), p. 37006 (6pp).

[37] G. de Loubens, V. V. Naletov, and O. Klein, *Reduction of the spin-wave damping induced by nonlinear effects*, Phys. Rev. B, 71 (2005), p. 180411(R).

[38] G. de Loubens, V. V. Naletov, O. Klein, J. B. Youssef, F. Boust, and N. Vukadinovic, *Magnetic Resonance Studies of the Fundamental Spin-Wave Modes in Individual Submicron Cu/NiFe/Cu Perpendicularly Magnetized Disks*, Physical Review Letters, 98 (2007), p. 127601.

[39] G. de Loubens, A. Riegler, B. Pigeau, F. Lochner, F. Boust, K. Y. Guslienko, H. Hurdequint, L. W. Molenkamp, G. Schmidt, A. N. Slavin, V. S. Tiberkevich, N. Vukadinovic, and O. Klein, *Bistability of vortex core dynamics in a single perpendicularly magnetized nanodisk*, Phys. Rev. Lett., 102 (2009), p. 177602.

[40] C. L. Degen, M. Poggio, H. J. Mamin, C. T. Rettner, and D. Rugar, *Nanoscale magnetic resonance imaging*, Proc. Natl. Acad. Sci., 106 (2009), p. 1313.

[41] V. E. Demidov, M. Buchmeier, K. Rott, P. Krzysteczko, J. Münchenberger, G. Reiss, and S. O. Demokritov, *Nonlinear hybridization of the fundamental eigenmodes of microscopic ferromagnetic ellipses*, Phys. Rev. Lett., 104 (2010), p. 217203.

[42] V. E. Demidov, M. Evelt, V. Bessonov, S. O. Demokritov, J. L. Prieto, M. Muñoz, J. B. Youssef, V. V. Naletov, G. de Loubens, O. Klein, M. Collet, P. Bortolotti, V. Cros, and A. Anane, *Direct observation of dynamic modes excited in a magnetic insulator by pure spin current*, Scientific Reports, 6 (2016), p. 32781.

[43] V. E. Demidov, U.-H. Hansen, and S. O. Demokritov, *Spin-wave eigenmodes of a saturated magnetic square at different precession angles*, Phys. Rev. Lett., 98 (2007), p. 157203.

[44] V. E. Demidov, S. Urazhdin, E. R. J. Edwards, M. D. Stiles, R. D. McMichael, and S. O. Demokritov, *Control of magnetic fluctuations by spin current*, Phys. Rev. Lett., 107 (2011), p. 107204.

[45] S. O. Demokritov, V. E. Demidov, O. Dzyapko, G. A. Melkov, A. A. Serga, B. Hillebrands, and A. N. Slavin, *Bose–Einstein condensation of quasi-equilibrium magnons at room temperature under pumping*, Nature, 443 (2006), pp. 430–433.

[46] A. Drews, B. Krüger, G. Selke, T. Kamionka, A. Vogel, M. Martens, U. Merkt, D. Möller, and G. Meier, *Nonlinear magnetic vortex gyration*, Phys. Rev. B, 85 (2012), p. 144417.

[47] C. Du, T. van der Sar, T. X. Zhou, P. Upadhyaya, F. Casola, H. Zhang, M. C. Onbasli, C. A. Ross, R. L. Walsworth, Y. Tserkovnyak, and A. Yacoby, *Control and local measurement of the spin chemical potential in a magnetic insulator*, Science, 357 (2017), pp. 195–198.

[48] A. Dussaux, E. Grimaldi, B. Rache Salles, A. S. Jenkins, A. V. Khvalkovskiy, P. Bortolotti, J. Grollier, H. Kubota, A. Fukushima, K. Yakushiji, S. Yuasa, V. Cros, and A. Fert, *Large amplitude spin torque vortex oscillations at zero external field using a perpendicular spin polarizer*, Appl. Phys. Lett., 105 (2014), p. 022404.

[49] A. Dussaux, A. V. Khvalkovskiy, P. Bortolotti, J. Grollier, V. Cros, and A. Fert, *Field dependence of spin-transfer-induced vortex dynamics in the nonlinear regime*, Phys. Rev. B, 86 (2012), p. 014402.

[50] A. Dussaux, A. V. Khvalkovskiy, J. Grollier, V. Cros, A. Fukushima, M. Konoto, H. Kubota, K. Yakushiji, S. Yuasa, K. Ando, and A. Fert, *Phase locking of vortex based spin transfer oscillators to a microwave current*, Appl. Phys. Lett., 98 (2011), p. 132506.

[51] M. I. Dyakonov and V. I. Perel, *Possibility of orienting electron spins with current*, JETP Lett., 13 (1971), pp. 467–469.

[52] A. Fernández-Pacheco, L. Serrano-Ramón, J. M. Michalik, M. R. Ibarra, J. M. D. Teresa, L. O'Brien, D. Petit, J. Lee, and R. P. Cowburn, *Three dimensional magnetic nanowires grown by focused electron-beam induced deposition*, Scientific Reports, 3 (2013), p. 1492.

[53] A. Fert, N. Reyren, and V. Cros, *Magnetic skyrmions: advances in physics and potential applications*, Nature Reviews Materials, 2 (2017), p. 17031.

[54] B. Flebus, P. Upadhyaya, R. A. Duine, and Y. Tserkovnyak, *Local thermomagnonic torques in two-fluid spin dynamics*, Phys. Rev. B, 94 (2016), p. 214428.

[55] D. A. Garanin, *Relaxation of superparamagnetic spins: Classical vs large-spin description*, Phys. Rev. B, 78 (2008), p. 144413.

[56] Z. V. Gareeva and K. Y. Guslienko, *Magnetic skyrmion dynamics in thin cylindrical dots*, Phys. Status Solidi RRL, (2016).

[57] B. Georges, J. Grollier, M. Darques, V. Cros, C. Deranlot, B. Marcilhac, G. Faini, and A. Fert, *Coupling efficiency for phase locking of a spin transfer nano-oscillator to a microwave current*, Phys. Rev. Lett., 101 (2008), p. 017201.

[58] L. Giovannini, F. Montoncello, F. Nizzoli, G. Gubbiotti, G. Carlotti, T. Okuno, T. Shinjo, and M. Grimsditch, *Spin excitations of nanometric cylindrical dots in vortex and saturated magnetic states*, Phys. Rev. B, 70 (2004), p. 172404.

[59] E. Grimaldi, A. Dussaux, P. Bortolotti, J. Grollier, G. Pillet, A. Fukushima, H. Kubota, K. Yakushiji, S. Yuasa, and V. Cros, *Response to noise of a vortex based spin transfer nano-oscillator*, Phys. Rev. B, 89 (2014), p. 104404.

[60] J. Grollier, V. Cros, and A. Fert, *Synchronization of spin-transfer oscillators driven by stimulated microwave currents*, Phys. Rev. B, 73 (2006), p. 060409.

[61] J. Grollier, D. Querlioz, and M. D. Stiles, *Spintronic nanodevices for bioinspired computing*, Proceedings of the IEEE, 104 (2016), pp. 2024–2039.

[62] Y. S. Gui, A. Wirthmann, and C.-M. Hu, *Foldover ferromagnetic resonance and damping in permalloy microstrips*, Phys. Rev. B, 80 (2009), p. 184422.

[63] F. Guo, L. M. Belova, and R. D. McMichael, *Spectroscopy and imaging of edge modes in permalloy nanodisks*, Phys. Rev. Lett., 110 (2013), p. 017601.

[64] A. G. Gurevich and G. A. Melkov, *Magnetization Oscillations and Waves*, CRC Press, 1996.

[65] K. Guslienko, B. Ivanov, V. Novosad, Y. Otani, H. Shima, and K. Fukamichi, *Eigenfrequencies of vortex state excitations in magnetic submicron-size disks*, J. Appl. Phys., 91 (2002), p. 8037.

[66] K. Y. Guslienko, *Low-frequency vortex dynamic susceptibility and relaxation in mesoscopic ferromagnetic dots*, Appl. Phys. Lett., 89 (2006), p. 022510.

[67] K. Y. Guslienko, *Magnetic vortex state stability, reversal and dynamics in restricted geometries*, J. Nanosci. Nanotechnol., 8 (2008), p. 2745.

[68] K. Y. Guslienko, G. R. Aranda, and J. M. Gonzalez, *Topological gauge field in nanomagnets: Spin-wave excitations over a slowly moving magnetization background*, Phys. Rev. B, 81 (2010), p. 014414.

[69] K. Y. Guslienko, S. O. Demokritov, B. Hillebrands, and A. N. Slavin, *Effective dipolar boundary conditions for dynamic magnetization in thin magnetic stripes*, Phys. Rev. B, 66 (2002), p. 132402.

[70] K. Y. Guslienko and Z. V. Gareeva, *Gyrotropic skyrmion modes in ultrathin magnetic circular dots*, IEEE Magn. Lett., 8 (2017), pp. 1–5.

[71] K. Y. Guslienko, X. F. Han, D. J. Keavney, R. Divan, and S. D. Bader, *Magnetic vortex core dynamics in cylindrical ferromagnetic dots*, Phys. Rev. Lett., 96 (2006), p. 067205.

[72] K. Y. Guslienko, G. N. Kakazei, J. Ding, X. M. Liu, and A. O. Adeyeye, *Giant moving vortex mass in thick magnetic nanodots*, Scientific Reports, 5 (2015), p. 13881.

[73] K. Y. Guslienko, K.-S. Lee, and S.-K. Kim, *Dynamic origin of vortex core switching in soft magnetic nanodots*, Phys. Rev. Lett., 100 (2008), p. 027203.

[74] K. Y. Guslienko, A. N. Slavin, V. Tiberkevich, and S.-K. Kim, *Dynamic origin of azimuthal modes splitting in vortex-state magnetic dots*, Phys. Rev. Lett., 101 (2008), p. 247203.

[75] M. Haertinger, C. H. Back, J. Lotze, M. Weiler, S. Geprägs, H. Huebl, S. T. B. Goennenwein, and G. Woltersdorf, *Spin pumping in yig/pt bilayers as a function of layer thickness*, Phys. Rev. B, 92 (2015), p. 054437.

[76] C. Hahn, G. de Loubens, O. Klein, M. Viret, V. V. Naletov, and J. Ben Youssef, *Comparative measurements of inverse spin hall effects and magnetoresistance in yig/pt and yig/ta*, Phys. Rev. B, 87 (2013), p. 174417.

[77] C. Hahn, G. de Loubens, V. V. Naletov, J. B. Youssef, O. Klein, and M. Viret, *Conduction of spin currents through insulating antiferromagnetic oxides*, EPL (Europhysics Letters), 108 (2014), p. 57005.

[78] C. Hahn, G. de Loubens, M. Viret, O. Klein, V. Naletov, V. and J. Ben Youssef, *Erratum: Detection of microwave spin pumping using the inverse spin hall effect [phys. rev. lett. 111, 217204 (2013)]*, Phys. Rev. Lett., 112 (2014), p. 179901.

[79] C. Hahn, G. de Loubens, M. Viret, O. Klein, V. V. Naletov, and J. Ben Youssef, *Detection of microwave spin pumping using the inverse spin hall effect*, Phys. Rev. Lett., 111 (2013), p. 217204.

[80] C. Hahn, V. V. Naletov, G. de Loubens, O. Klein, O. d'Allivy Kelly, A. Anane, R. Bernard, E. Jacquet, P. Bortolotti, V. Cros, J. L. Prieto, and M. Muñoz, *Measurement of the intrinsic damping constant in individual nanodisks of y3fe5o12 and y3fe5o12—pt*, Appl. Phys. Lett., 104 (2014), p. 152410.

[81] A. Hamadeh, O. d'Allivy Kelly, C. Hahn, H. Meley, R. Bernard, A. H. Molpeceres, V. V. Naletov, M. Viret, A. Anane, V. Cros, S. O. Demokritov, J. L. Prieto, M. Muñoz, G. de Loubens, and O. Klein, *Full control of the spin-wave damping in a magnetic insulator using spin-orbit torque*, Phys. Rev. Lett., 113 (2014), p. 197203.

[82] A. Hamadeh, G. de Loubens, V. V. Naletov, J. Grollier, C. Ulysse, V. Cros, and O. Klein, *Autonomous and forced dynamics in a spin-transfer nano-oscillator: Quantitative magnetic-resonance force microscopy*, Phys. Rev. B, 85 (2012), p. 140408.

[83] A. Hamadeh, N. Locatelli, V. Naletov, V. R. Lebrun, G. de Loubens, J. Grollier, O. Klein, and V. Cros, *Origin of spectral purity and tuning sensitivity in a spin transfer vortex nano-oscillator*, Phys. Rev. Lett., 112 (2014), p. 257201.

[84] A. Hamadeh, N. Locatelli, V. V. Naletov, R. Lebrun, G. de Loubens, J. Grollier, O. Klein, and V. Cros, *Perfect and robust phase-locking of a spin transfer vortex nano-oscillator to an external microwave source*, Appl. Phys. Lett., 104 (2014), p. 022408.

[85] C. Hauser, T. Richter, N. Homonnay, C. Eisenschmidt, M. Qaid, H. Deniz, D. Hesse, M. Sawicki, S. G. Ebbinghaus, and G. Schmidt, *Yttrium iron garnet thin films with very low damping obtained by recrystallization of amorphous material*, Sci. Rep., 6 (2016), p. 20827.

[86] B. Heinrich, C. Burrowes, E. Montoya, B. Kardasz, E. Girt, Y.-Y. Song, Y. Sun, and M. Wu, *Spin pumping at the magnetic insulator (YIG)/normal metal (Au) interfaces*, Phys. Rev. Lett., 107 (2011), p. 066604.

[87] R. Hertel, S. Gliga, M. Fähnle, and C. M. Schneider, *Ultrafast nanomagnetic toggle switching of vortex cores*, Phys. Rev. Lett., 98 (2007), p. 117201.

[88] J. E. Hirsch, *Spin Hall effect*, Phys. Rev. Lett., 83 (1999), pp. 1834–1837.

[89] F. Hoffmann, G. Woltersdorf, K. Perzlmaier, A. N. Slavin, V. S. Tiberkevich, A. Bischof, D. Weiss, and C. H. Back, *Mode degeneracy due to vortex core removal in magnetic disks*, Phys. Rev. B, 76 (2007), p. 014416.

[90] E. Iacocca, P. Dürrenfeld, O. Heinonen, J. Åkerman, and R. K. Dumas, *Mode-coupling mechanisms in nanocontact spin-torque oscillators*, Phys. Rev. B, 91 (2015), p. 104405.

[91] B. A. Ivanov and G. M. Wysin, *Magnon modes for a circular two-dimensional easy-plane ferromagnet in the cone state*, Phys. Rev. B, 65 (2002), p. 134434.

[92] P. Johnson, A. K. Gangopadhyay, R. Kalyanaraman, and Z. Nussinov, *Demagnetization-borne microscale skyrmions*, Phys. Rev. B, 86 (2012), p. 064427.

[93] M. B. Jungfleisch, A. V. Chumak, A. Kehlberger, V. Lauer, D. H. Kim, M. C. Onbasli, C. A. Ross, M. Kläui, and B. Hillebrands, *Thickness and power dependence of the spin-pumping effect in* $y_3fe_5o_{12}$*/pt heterostructures measured by the inverse spin hall effect*, Phys. Rev. B, 91 (2015), p. 134407.

[94] Y. Kajiwara, K. Harii, S. Takahashi, J. Ohe, K. Uchida, M. Mizuguchi, H. Umezawa, H. Kawai, K. Ando, K. Takanashi, S. Maekawa, and E. Saitoh, *Transmission of electrical signals by spin-wave interconversion in a magnetic insulator*, Nature, 464 (2010), pp. 262–266.

[95] S. Kaka, M. R. Pufall, W. H. Rippard, T. J. Silva, S. E. Russek, and J. A. Katine, *Mutual phase-locking of microwave spin torque nano-oscillators*, Nature, 437 (2005), pp. 389–392.

[96] G. N. Kakazei, P. E. Wigen, K. Y. Guslienko, V. Novosad, A. N. Slavin, V. O. Golub, N. A. Lesnik, and Y. Otani, *Spin-wave spectra of perpendicularly magnetized circular submicron dot arrays*, Appl. Phys. Lett., 85 (2004), pp. 443–445.

[97] T. Kampfrath, A. Sell, G. Klatt, A. Pashkin, S. Mährlein, T. Dekorsy, M. Wolf, M. Fiebig, A. Leitenstorfer, and R. Huber, *Coherent terahertz control of antiferromagnetic spin waves*, Nature Photonics, 5 (2011), pp. 31–34.

[98] A. V. Khvalkovskiy, A. N. Slavin, J. Grollier, K. A. Zvezdin, and K. Y. Guslienko, *Critical velocity for the vortex core reversal in perpendicular bias magnetic field*, Appl. Phys. Lett., 96 (2010), p. 022504.

[99] R. Khymyn, I. Lisenkov, V. Tiberkevich, B. Ivanov, and A. Slavin, *Antiferromagnetic thz-frequency josephson-like oscillator driven by spin current*, Scientific Reports, 7 (2017), p. 43705.

[100] J.-V. Kim, F. Garcia-Sanchez, J. a. Sampaio, C. Moreau-Luchaire, V. Cros, and A. Fert, *Breathing modes of confined skyrmions in ultrathin magnetic dots*, Phys. Rev. B, 90 (2014), p. 064410.

[101] J.-V. Kim, V. Tiberkevich, and A. N. Slavin, *Generation linewidth of an auto-oscillator with a nonlinear frequency shift: Spin-torque nano-oscillator*, Phys. Rev. Lett., 100 (2008), p. 017207.

[102] S.-K. Kim, M.-W. Yoo, J. Lee, H.-Y. Lee, J.-H. Lee, Y. Gaididei, V. P. Kravchuk, and D. D. Sheka, *Resonantly exited precession motion of three-dimensional vortex core in magnetic nanospheres*, Scientific Reports, 5 (2015), p. 11370.

[103] C. Kittel, *Theory of Antiferromagnetic Resonance*, Phys. Rev., 82 (1951), pp. 565–565.

[104] O. Klein, G. de Loubens, V. V. Naletov, F. Boust, T. Guillet, H. Hurdequint, A. Leksikov, A. N. Slavin, V. S. Tiberkevich, and N. Vukadinovic, *Ferromagnetic resonance force spectroscopy of individual submicron-size samples*, Phys. Rev. B, 78 (2008), p. 144410.

[105] Y. Kobljanskyj, G. Melkov, K. Guslienko, V. Novosad, S. D. Bader, M. Kostylev, and A. Slavin, *Nano-structured magnetic metamaterial with enhanced nonlinear properties*, Scientific Reports, 2 (2012), p. 478.

[106] A. Kosevich, B. Ivanov, and A. Kovalev, *Magnetic solitons*, Physics Reports, 194 (1990), pp. 117 – 238.

[107] V. V. Kruglyak, S. O. Demokritov, and D. Grundler, *Magnonics*, J. Phys. D: Appl. Phys., 43 (2010), p. 264001.

[108] H. Kurebayashi, O. Dzyapko, V. E. Demidov, D. Fang, A. J. Ferguson, and S. O. Demokritov, *Controlled enhancement of spin-current emission by three-magnon splitting*, Nature Materials, 10 (2011), pp. 660–664.

[109] H. Lavenant, V. Naletov, O. Klein, G. de Loubens, L. Casado, and J. M. De Teresa, *Mechanical magnetometry of cobalt nanospheres deposited by focused electron beam at the tip of ultra-soft cantilevers*, Nanofabrication, 1 (2014), pp. 65–73.

[110] R. Lebrun, J. Grollier, F. Abreu Araujo, P. Bortolotti, V. Cros, A. Hamadeh, X. de Milly, Y. Li, G. de Loubens, O. Klein, S. Tsunegi, H. Kubota, K. Yakushiji, A. Fukushima, and S. Yuasa, *Driven energy transfer between coupled modes in spin-torque oscillators*, Phys. Rev. B, 95 (2017), p. 134444.

[111] R. Lebrun, A. Jenkins, A. Dussaux, N. Locatelli, S. Tsunegi, E. Grimaldi, H. Kubota, P. Bortolotti, K. Yakushiji, J. Grollier, A. Fukushima, S. Yuasa, and V. Cros, *Understanding of phase noise squeezing under fractional synchronization of a nonlinear spin transfer vortex oscillator*, Phys. Rev. Lett., 115 (2015), p. 017201.

[112] R. Lebrun, N. Locatelli, S. Tsunegi, J. Grollier, V. Cros, F. Abreu Araujo, H. Kubota, K. Yakushiji, A. Fukushima, and S. Yuasa, *Nonlinear behavior and mode coupling in spin-transfer nano-oscillators*, Phys. Rev. Applied, 2 (2014), p. 061001.

[113] R. Lebrun, S. Tsunegi, P. Bortolotti, H. Kubota, A. S. Jenkins, M. Romera, K. Yakushiji, A. Fukushima, J. Grollier, S. Yuasa, and V. Cros, *Mutual synchronization of spin torque nano-oscillators through a long-range and tunable electrical coupling scheme*, Nature Communications, 8 (2017), p. 15825.

[114] I. Lee, Y. Obukhov, G. Xiang, A. Hauser, F. Yang, P. Banerjee, D. Pelekhov, and P. Hammel, *Nanoscale scanning probe ferromagnetic resonance imaging using localized modes*, Nature, 466 (2010), pp. 845–848.

[115] K.-S. Lee, S.-K. Kim, Y.-S. Yu, Y.-S. Choi, K. Y. Guslienko, H. Jung, and P. Fischer, *Universal criterion and phase diagram for switching a magnetic vortex core in soft magnetic nanodots*, Phys. Rev. Lett., 101 (2008), p. 267206.

[116] Y. Li, X. de Milly, F. Abreu Araujo, O. Klein, V. Cros, J. Grollier, and G. de Loubens, *Probing phase coupling between two spin-torque nano-oscillators with an external source*, Phys. Rev. Lett., 118 (2017), p. 247202.

[117] N. Locatelli, V. Cros, and J. Grollier, *Spin-torque building blocks*, Nature Materials, 13 (2014), pp. 11–20.

[118] N. Locatelli, A. Hamadeh, F. A. Araujo, A. D. Belanovsky, P. N. Skirdkov, R. Lebrun, V. V. Naletov, K. A. Zvezdin, M. Muñoz, J. Grollier, O. Klein, V. Cros, and G. de Loubens, *Efficient synchronization of dipolarly coupled vortex-based spin transfer nano-oscillators*, Scientific Reports, 5 (2015), p. 17039.

[119] N. Locatelli, R. Lebrun, V. Naletov, A. Hamadeh, G. De Loubens, O. Klein, J. Grollier, and V. Cros, *Improved spectral stability in spin-transfer nano-oscillators: Single vortex versus coupled vortices dynamics*, IEEE Trans. Magn., 51 (2015), p. 4300206.

[120] N. Locatelli, V. V. Naletov, J. Grollier, G. de Loubens, V. Cros, C. Deranlot, C. Ulysse, G. Faini, O. Klein, and A. Fert, *Dynamics of two coupled vortices in a spin valve nanopillar excited by spin transfer torque*, Appl. Phys. Lett., 98 (2011), p. 062501.

[121] H. Makino and Y. Hidaka, *Determination of magnetic anisotropy constants for bubble garnet epitaxial films using field orientation dependence in ferromagnetic resonances*, Mat. Res. Bull., 16 (1981), pp. 957–966.

[122] F. B. Mancoff, N. D. Rizzo, B. N. Engel, and S. Tehrani, *Phase-locking in double-point-contact spin-transfer devices*, Nature, 437 (2005), p. 393.

[123] S. A. Manuilov, S. I. Khartsev, and A. M. Grishin, *Pulsed laser deposited y3fe5o12 films: Nature of magnetic anisotropy i*, J. Appl. Phys., 106 (2009), p. 123917.

[124] R. McMichael and P. Krivosik, *Classical model of extrinsic ferromagnetic resonance linewidth in ultrathin films*, IEEE Trans. Magn., 40 (2004), pp. 2–11.

[125] G. Melkov, D. Slobodianiuk, V. Tiberkevich, G. de Loubens, O. Klein, and A. Slavin, *Nonlinear ferromagnetic resonance in nanostructures having discrete spectrum of spin-wave modes*, IEEE Magn. Lett., 4 (2013), pp. 4000504–4000504.

[126] K. L. Metlov, *Vortex precession frequency and its amplitude-dependent shift in cylindrical nanomagnets*, J. Appl. Phys., 114 (2013), p. 223908.

[127] C. Miramond, C. Fermon, F. Rousseaux, D. Decanini, and F. Carcenac, *Permalloy cylindrical submicron size dot arrays*, J. Magn. Magn. Mater., 165 (1997), pp. 500–503.

[128] Q. Mistral, M. van Kampen, G. Hrkac, J.-V. Kim, T. Devolder, P. Crozat, C. Chappert, L. Lagae, and T. Schrefl, *Current-driven vortex oscillations in metallic nanocontacts*, Phys. Rev. Lett., 100 (2008), p. 257201.

[129] S. M. Mohseni, S. R. Sani, J. Persson, T. N. A. Nguyen, S. Chung, Y. Pogoryelov, P. K. Muduli, E. Iacocca, A. Eklund, R. K. Dumas, S. Bonetti, A. Deac, M. A. Hoefer, and J. Akerman, *Spin torque-generated magnetic droplet solitons*, Science, 339 (2013), pp. 1295–1298.

[130] C. Moreau-Luchaire, C. Moutafis, N. Reyren, J. Sampaio, C. Vaz, N. Van Horne, K. Bouzehouane, K. Garcia, C. Deranlot, P. Warnicke, et al., *Additive interfacial chiral interaction in multilayers for stabilization of small individual skyrmions at room temperature*, Nature Nanotechnology, 11 (2016), pp. 444–448.

[131] M. Morota, Y. Niimi, K. Ohnishi, D. H. Wei, T. Tanaka, H. Kontani, T. Kimura, and Y. Otani, *Indication of intrinsic spin hall effect in 4d and 5d transition metals*, Phys. Rev. B, 83 (2011), p. 174405.

[132] M. Mruczkiewicz, M. Krawczyk, and K. Y. Guslienko, *Spin excitation spectrum in a magnetic nanodot with continuous transitions between the vortex, bloch-type skyrmion, and néel-type skyrmion states*, Phys. Rev. B, 95 (2017), p. 094414.

[133] H. Nakayama, M. Althammer, Y.-T. Chen, K. Uchida, Y. Kajiwara, D. Kikuchi, T. Ohtani, S. Geprägs, M. Opel, S. Takahashi, R. Gross, G. E. W. Bauer, S. T. B. Goennenwein, and E. Saitoh, *Spin hall magnetoresistance induced by a nonequilibrium proximity effect*, Phys. Rev. Lett., 110 (2013), p. 206601.

[134] V. V. Naletov, G. de Loubens, G. Albuquerque, S. Borlenghi, V. Cros, G. Faini, J. Grollier, H. Hurdequint, N. Locatelli, B. Pigeau, A. N. Slavin, V. S. Tiberkevich, C. Ulysse, T. Valet, and O. Klein, *Identification and selection rules of the spin-wave eigenmodes in a normally magnetized nanopillar*, Phys. Rev. B, 84 (2011), p. 224423.

[135] I. Neudecker, K. Perzlmaier, F. Hoffmann, G. Woltersdorf, M. Buess, D. Weiss, and C. H. Back, *Modal spectrum of permalloy disks excited by in-plane magnetic fields*, Phys. Rev. B, 73 (2006), p. 134426.

[136] D. E. Nikonov, G. Csaba, W. Porod, T. Shibata, D. Voils, D. Hammerstrom, I. A. Young, and G. I. Bourianoff, *Coupled-oscillator associative memory array operation for pattern recognition*, IEEE J. Explor. Solid-State Computat. Devices Circuits, 1 (2015), pp. 85–93.

[137] N. Noginova, F. Chen, T. Weaver, E. P. Giannelis, A. B. Bourlinos, and V. A. Atsarkin, *Magnetic resonance in nanoparticles: between ferro- and paramagnetism*, J. Phys.: Condens. Matter, 19 (2007), p. 246208.

[138] V. Novosad, F. Y. Fradin, P. E. Roy, K. S. Buchanan, K. Y. Guslienko, and S. D. Bader, *Magnetic vortex resonance in patterned ferromagnetic dots*, Phys. Rev. B, 72 (2005), p. 024455.

[139] V. Novosad, M. Grimsditch, K. Y. Guslienko, P. Vavassori, Y. Otani, and S. D. Bader, *Spin excitations of magnetic vortices in ferromagnetic nanodots*, Phys. Rev. B, 66 (2002), p. 052407.

[140] O. E. Omel'chenko and M. Wolfrum, *Nonuniversal transitions to synchrony in the sakaguchi-kuramoto model*, Phys. Rev. Lett., 109 (2012), p. 164101.

[141] M. C. Onbasli, A. Kehlberger, D. H. Kim, G. Jakob, M. Kläui, A. V. Chumak, B. Hillebrands, and C. A. Ross, *Pulsed laser deposition of epitaxial yttrium iron garnet films with low gilbert damping and bulk-like magnetization*, APL Mater., 2 (2014), p. 106102.

[142] J. P. Park and P. A. Crowell, *Interactions of spin waves with a magnetic vortex*, Phys. Rev. Lett., 95 (2005), p. 167201.

[143] J. P. Park, P. Eames, D. M. Engebretson, J. Berezovsky, and P. A. Crowell, *Imaging of spin dynamics in closure domain and vortex structures*, Phys. Rev. B, 67 (2003), p. 020403.

[144] B. Pigeau, G. de Loubens, O. Klein, A. Riegler, F. Lochner, G. Schmidt, and L. W. Molenkamp, *Optimal control of vortex-core polarity by resonant microwave pulses*, Nature Physics, 7 (2011), pp. 26–31.

[145] B. Pigeau, G. de Loubens, O. Klein, A. Riegler, F. Lochner, G. Schmidt, L. W. Molenkamp, V. S. Tiberkevich, and A. N. Slavin, *A frequency-controlled magnetic vortex memory*, Appl. Phys. Lett., 96 (2010), p. 132506.

[146] B. Pigeau, C. Hahn, G. de Loubens, V. V. Naletov, O. Klein, K. Mitsuzuka, D. Lacour, M. Hehn, S. Andrieu, and F. Montaigne, *Measurement of the dynamical dipolar coupling in a pair of magnetic nanodisks using a ferromagnetic resonance force microscope*, Phys. Rev. Lett., 109 (2012), p. 247602.

[147] A. Pikovsky, M. Rosenblum, and J. Kurths, *Synchronization: A Universal Concept in Nonlinear Sciences*, Cambridge University Press, Cambridge, England, 2001.

[148] V. S. Pribiag, I. N. Krivorotov, G. D. Fuchs, P. M. Braganca, O. Ozatay, J. C. Sankey, D. C. Ralph, and R. A. Buhrman, *Magnetic vortex oscillator driven by d.c. spin-polarized current*, Nature Phys., 3 (2007), pp. 498–503.

[149] O. V. Pylypovskyi, D. D. Sheka, and Y. Gaididei, *Bloch point structure in a magnetic nanosphere*, Phys. Rev. B, 85 (2012), p. 224401.

[150] M. Quinsat, J. F. Sierra, I. Firastrau, V. Tiberkevich, A. Slavin, D. Gusakova, L. D. Buda-Prejbeanu, M. Zarudniev, J.-P. Michel, U. Ebels, B. Dieny, M.-C. Cyrille, J. A. Katine, D. Mauri, and A. Zeltser, *Injection locking of tunnel junction oscillators to a microwave current*, Appl. Phys. Lett., 98 (2011), p. 182503.

[151] M. Quinsat, V. Tiberkevich, D. Gusakova, A. Slavin, J. F. Sierra, U. Ebels, L. D. Buda-Prejbeanu, B. Dieny, M.-C. Cyrille, A. Zelster, and J. A. Katine, *Linewidth of higher harmonics in a nonisochronous auto-oscillator: Application to spin-torque nano-oscillators*, Phys. Rev. B, 86 (2012), p. 104418.

[152] W. H. Rippard, M. R. Pufall, S. Kaka, T. J. Silva, S. E. Russek, and J. A. Katine, *Injection locking and Phase Control of Spin Transfer Nano-oscillators*, Phys. Rev. Lett., 95 (2005), p. 067203.

[153] D. Rugar, R. Budakian, H. J. Mamin, and B. W. Chui, *Single spin detection by magnetic resonance force microscopy*, Nature, 430 (2004), pp. 329–332.

[154] A. Ruotolo, V. Cros, B. Georges, A. Dussaux, J. Grollier, C. Deranlot, R. Guillemet, K. Bouzehouane, S. Fusil, and A. Fert, *Phase-locking of magnetic vortices mediated by antivortices*, Nature Nanotech., 4 (2009), pp. 528–532.

[155] V. S. Rychkov, S. Borlenghi, H. Jaffres, A. Fert, and X. Waintal, *Spin torque and waviness in magnetic multilayers: A bridge between valet-fert theory and quantum approaches*, Phys. Rev. Lett., 103 (2009), p. 066602.

[156] C. Safranski, I. Barsukov, H. K. Lee, T. Schneider, A. Jara, A. Smith, H. Chang, K. Lenz, J. Lindner, Y. Tserkovnyak, M. Wu, and I. Krivorotov, *Spin caloritronic nano-oscillator*, Nature Communications, 8 (2017), p. 117.

[157] J. Sampaio, V. Cros, S. Rohart, A. Thiaville, and A. Fert, *Nucleation, stability and current-induced motion of isolated magnetic skyrmions in nanostructures*, Nature Nanotechnology, 8 (2013), pp. 839–844.

[158] C. W. Sandweg, Y. Kajiwara, K. Ando, E. Saitoh, and B. Hillebrands, *Enhancement of the spin pumping efficiency by spin wave mode selection*, Appl. Phys. Lett., 97 (2010), p. 252504.

[159] S. Sangiao, C. Magén, D. Mofakhami, G. de Loubens, and J. M. De Teresa, *Magnetic properties of optimized cobalt nanospheres grown by focused electron beam induced deposition (febid) on cantilever tips*, Beilstein J. Nanotechnol., 8 (2017), pp. 2106–2115.

[160] T. Shinjo, T. Okuno, R. Hassdorf, K. Shigeto, and T. Ono, *Magnetic Vortex Core Observation in Circular Dots of Permalloy*, Science, 289 (2000), pp. 930–932.

[161] J. A. Sidles, *Noninductive detection of single-proton magnetic resonance*, Appl. Phys. Lett., 58 (1991), p. 2854.

[162] J. A. Sidles, J. L. Garbini, K. J. Bruland, D. Rugar, O. Züger, S. Hoen, and C. S. Yannoni, *Magnetic resonance force microscopy*, Rev. Mod. Phys., 67 (1995), p. 249.

[163] A. Slavin and V. Tiberkevich, *Nonlinear auto-oscillator theory of microwave generation by spin-polarized current*, IEEE Trans. Magn., 45 (2009), pp. 1875–1918.

[164] A. N. Slavin and V. S. Tiberkevich, *Nonlinear self-phase-locking effect in an array of current-driven magnetic nanocontacts*, Phys. Rev. B, 72 (2005), p. 092407.

[165] J. Slonczewski, *Current-driven excitation of magnetic multilayers*, J. Magn. Magn. Mater., 159 (1996), pp. L1–L7.

[166] M. Sparks, *Ferromagnetic relaxation theory*, McGraw-Hill, New York, 1964.

[167] E. G. Spencer, R. C. LeCraw, and A. M. Clogston, *Low-temperature linewidth maximum in yttrium iron garnet*, Phys. Rev. Lett., 3 (1959), pp. 32–33.

[168] B. C. Stipe, H. J. Mamin, T. D. Stowe, T. W. Kenny, and D. Rugar, *Magnetic dissipation and fluctuations in individual nanomagnets measured by ultrasensitive cantilever magnetometry*, Phys. Rev. Lett., 86 (2001), p. 2874.

[169] S. Sugimoto, Y. Fukuma, S. Kasai, T. Kimura, A. Barman, and Y. Otani, *Dynamics of coupled vortices in a pair of ferromagnetic disks*, Phys. Rev. Lett., 106 (2011), p. 197203.

[170] H. Suhl, *The theory of ferromagnetic resonance at high signal powers*, J. Phys. Chem. Solids, 1 (1957), p. 209.

[171] O. V. Sukhostavets, J. González, and K. Y. Guslienko, *Multipole magnetostatic interactions and collective vortex excitations in dot pairs, chains, and two-dimensional arrays*, Phys. Rev. B, 87 (2013), p. 094402.

[172] O. V. Sukhostavets, B. Pigeau, S. Sangiao, G. de Loubens, V. V. Naletov, O. Klein, K. Mitsuzuka, S. Andrieu, F. Montaigne, and K. Y. Guslienko, *Probing the anharmonicity of the potential well for a magnetic vortex core in a nanodot*, Phys. Rev. Lett., 111 (2013), p. 247601.

[173] Y. Sun, Y.-Y. Song, H. Chang, M. Kabatek, M. Jantz, W. Schneider, M. Wu, H. Schultheiss, and A. Hoffmann, *Growth and ferromagnetic resonance properties of nanometer-thick yttrium iron garnet films*, Appl. Phys. Lett., 101 (2012), p. 152405.

[174] T. Tanaka, H. Kontani, M. Naito, T. Naito, D. S. Hirashima, K. Yamada, and J. Inoue, *Intrinsic spin hall effect and orbital hall effect in* 4*d and* 5*d transition metals*, Phys. Rev. B, 77 (2008), p. 165117.

[175] B. Taurel, T. Valet, V. V. Naletov, N. Vukadinovic, G. de Loubens, and O. Klein, *Complete mapping of the spin-wave spectrum in a vortex-state nanodisk*, Phys. Rev. B, 93 (2016), p. 184427.

[176] A. Thiaville, J. M. García, R. Dittrich, J. Miltat, and T. Schrefl, *Micromagnetic study of bloch-point-mediated vortex core reversal*, Phys. Rev. B, 67 (2003), p. 094410.

[177] A. Thiaville, N. Vukadinovic, and O. Acher, *Sum rule for the magnetic permeability of arbitrary textures*, Phys. Rev. B, 86 (2012), p. 214404.

[178] A. A. Thiele, *Steady-state motion of magnetic domains*, Phys. Rev. Lett., 30 (1973), pp. 230–233.

[179] C. Thirion, W. Wernsdorfer, and D. Mailly, *Switching of magnetization by nonlinear resonance studied in single nanoparticles*, Nature Materials, 2 (2003), p. 524.

[180] V. Tiberkevich and A. Slavin, *Nonlinear phenomenological model of magnetic dissipation for large precession angles: Generalization of the Gilbert model*, Phys. Rev. B, 75 (2007), p. 014440.

[181] V. Tiberkevich, A. Slavin, E. Bankowski, and G. Gerhart, *Phase-locking and frustration in an array of nonlinear spin-torque nano-oscillators*, Appl. Phys. Lett., 95 (2009), p. 262505.

[182] V. S. Tiberkevich, R. S. Khymyn, H. X. Tang, and A. N. Slavin, *Sensitivity to external signals and synchronization properties of a non-isochronous auto-oscillator with delayed feedback*, Sci. Rep., 4 (2014), p. 3873.

[183] Y. Tserkovnyak, A. Brataas, G. E. W. Bauer, and B. I. Halperin, *Nonlocal magnetization dynamics in ferromagnetic heterostructures*, Rev. Mod. Phys., 77 (2005), p. 1375.

[184] S. Tsunegi, H. Kubota, K. Yakushiji, M. Konoto, S. Tamaru, A. Fukushima, H. Arai, H. Imamura, E. Grimaldi, R. Lebrun, J. Grollier, V. Cros, and S. Yuasa, *High emission power and q factor in spin torque vortex oscillator consisting of feb free layer*, Appl. Phys. Express, 7 (2014), p. 063009.

[185] K. Uchida, J. Xiao, H. Adachi, J. Ohe, S. Takahashi, J. Ieda, T. Ota, Y. Kajiwara, H. Umezawa, H. Kawai, G. E. W. Bauer, S. Maekawa, and E. Saitoh, *Spin seebeck insulator*, Nature Materials, 9 (2010), pp. 894–897.

[186] S. Urazhdin, P. Tabor, V. Tiberkevich, and A. Slavin, *Fractional synchronization of spin-torque nano-oscillators*, Phys. Rev. Lett., 105 (2010), p. 104101.

[187] I. Utke, P. Hoffmann, R. Berger, and L. Scandella, *High-resolution magnetic co supertips grown by a focused electron beam*, Appl. Phys. Lett., 80 (2002), pp. 4792–4794.

[188] A. Vansteenkiste, K. W. Chou, M. Weigand, M. Curcic, V. Sackmann, H. Stoll, T. Tyliszczak, G. Woltersdorf, C. H. Back, G. Schütz, and B. V. Waeyenberge, *X-ray imaging of the dynamic magnetic vortex core deformation*, Nature Physics, 5 (2009), pp. 332–334.

[189] L. H. Vilela-Leão, C. Salvador, A. Azevedo, and S. M. Rezende, *Unidirectional anisotropy in the spin pumping voltage in yttrium iron garnet/platinum bilayers*, Appl. Phys. Lett., 99 (2011), p. 102505.

[190] D. Vodenicarevic, N. Locatelli, F. A. Araujo, J. Grollier, and D. Querlioz, *A nanotechnology-ready computing scheme based on a weakly coupled oscillator network*, Sci. Rep., 7 (2017), p. 44772.

[191] K. Vogt, O. Sukhostavets, H. Schultheiss, B. Obry, P. Pirro, A. A. Serga, T. Sebastian, J. Gonzalez, K. Y. Guslienko, and B. Hillebrands, *Optical detection of vortex spin-wave eigenmodes in microstructured ferromagnetic disks*, Phys. Rev. B, 84 (2011), p. 174401.

[192] B. V. Waeyenberge, A. Puzic, H. Stoll, K. W. Chou, T. Tyliszczak, R. Hertel, M. Fähnle, H. Bräckl, K. Rott, G. Reiss, I. Neudecker, D. Weiss, C. H. Back, and G. Schütz, *Magnetic vortex core reversal by excitation with short bursts of an alternating field*, Nature, 444 (2006), pp. 461 – 464.

[193] H. Wang, C. Du, P. C. Hammel, and F. Yang, *Antiferromagnonic spin transport from* $y_3fe_5o_{12}$ *into nio*, Phys. Rev. Lett., 113 (2014), p. 097202.

[194] H. L. Wang, C. H. Du, Y. Pu, R. Adur, P. C. Hammel, and F. Y. Yang, *Large spin pumping from epitaxial* $y_3fe_5o_{12}$ *thin films to pt and w layers*, Phys. Rev. B, 88 (2013), p. 100406.

[195] D. Wei, M. Obstbaum, M. Ribow, C. H. Back, and G. Woltersdorf, *Spin hall voltages from a.c. and d.c. spin currents*, Nature Communications, 5 (2014), p. 3768.

[196] M. Weigand, B. V. Waeyenberge, A. Vansteenkiste, M. Curcic, V. Sackmann, H. Stoll, T. Tyliszczak, K. Kaznatcheev, D. Bertwistle, G. Woltersdorf, C. H. Back, and G. Schütz, *Vortex core switching by coherent excitation with single in-plane magnetic field pulses*, Phys. Rev. Lett., 102 (2009), p. 077201.

[197] M. Weiler, J. M. Shaw, H. T. Nembach, and T. J. Silva, *Phase-sensitive detection of spin pumping via the ac inverse spin hall effect*, Phys. Rev. Lett., 113 (2014), p. 157204.

[198] P. E. Wigen, ed., *Nonlinear Phenomena and Chaos in Magnetic Materials*, World ScientificWorld Scientific, Singapore, 1994.

[199] J. Xiao and G. E. W. Bauer, *Spin-wave excitation in magnetic insulators by spin-transfer torque*, Phys. Rev. Lett., 108 (2012), p. 217204.

[200] K. Yamada, S. Kasai, Y. Nakatani, K. Kobayashi, H. Kohno, A. Thiaville, and T. Ono, *Electrical switching of the vortex core in a magnetic disk*, Nature Materials, 6 (2007), pp. 270–273.

[201] M.-W. Yoo, K.-S. Lee, D.-E. Jeong, and S.-K. Kim, *Origin, criterion, and mechanism of vortex-core reversals in soft magnetic nanodisks under perpendicular bias fields*, Phys. Rev. B, 82 (2010), p. 174437.

[202] C. E. Zaspel, E. S. Wright, A. Y. Galkin, and B. A. Ivanov, *Frequencies of radially symmetric excitations in vortex state disks*, Phys. Rev. B, 80 (2009), p. 094415.

[203] Z. Zhang, P. C. Hammel, and P. E. Wigen, *Observation of ferromagnetic resonance in a microscopic sample using magnetic resonance force microscopy*, Appl. Phys. Lett., 68 (1996), p. 2005.

[204] R. Zivieri and F. Nizzoli, *Theory of spin modes in vortex-state ferromagnetic cylindrical dots*, Phys. Rev. B, 71 (2005), p. 014411.